ABSTRACT

Lappeenranta University of Technology
Department of Energy and Environmental Technology

Eveliina Takasuo

Modeling of pressurizer using APROS and TRACE thermal hydraulic codes

Master's Thesis

2005

111 pages, 59 figures, 6 tables and 1 appendix

Examiners: Professor Riitta Kyrki-Rajamäki
Senior Research Scientist Ismo Karppinen

Keywords: pressurizer, thermal hydraulic model, APROS, TRACE, PACTEL, separate effect test

The objective of the Master's thesis is detailed thermal hydraulic modeling of the PWR pressurizer using both APROS simulation software package and TRACE code. The constructed models have been assessed against data from insurge, outsurge and spray experiments conducted at test facilities suitable for separate effect pressurizer tests in order to find an optimal modeling approach for simulating pressurizer transients. A main goal of the research was validating the pressurizer model of APROS against the background provided by experiments from three different test facilities, namely PACTEL, MIT pressurizer and Neptunus facility. In addition, a model of the Loviisa NPP pressurizer has been generated and the pressurizer behavior during a turbine trip transient was simulated for the purpose of investigating the scaling effect on the performance of the APROS pressurizer calculation. The separate tests have been simulated using different nodalization schemes and modeling options, and extensive comparisons between the results given by APROS and TRACE have been made. The TRACE simulations are also a part of the international CAMP code validation program of the United States Nuclear Regulatory Commission. Based on the simulation results, an evaluation of the capabilities of the heat transfer models to predict pressure behavior in the two codes has been provided. A significant drawback in the APROS pressurizer calculation was discovered and an improvement to the calculation was achieved by incorporating a new wall condensation correlation into the code.

TIIVISTELMÄ

Lappeenrannan teknillinen yliopisto
Energia- ja ympäristötekniikan osasto

Eveliina Takasuo

Paineistimen mallinnus APROS- ja TRACE -termohydrauliikkaohjelmistoilla

Diplomityö

2005

111 sivua, 59 kuvaa, 6 taulukkoa ja 1 liite

Tarkastajat: Professori Riitta Kyrki-Rajamäki
Erikoistutkija, DI Ismo Karppinen

Hakusanat: paineistin, termohydraulinen malli, APROS, TRACE, PACTEL, erilliskoe
Keywords: pressurizer, thermal hydraulic model, APROS, TRACE, PACTEL, separate effect test

Diplomityön tavoitteena on paineistimen yksityiskohtainen mallintaminen APROS- ja TRACE -termohydrauliikkaohjelmistoja käyttäen. Rakennetut paineistinmallit testattiin vertaamalla laskentatuloksia paineistimen täyttymistä, tyhjentymistä ja ruiskutusta käsittelevistä erilliskokeista saatuun mittausdataan. Tutkimuksen päätavoitteena on APROSin paineistinmallin validoiminen käyttäen vertailuaineistona PACTEL ATWS–koesarjan sopivia paineistinkokeita sekä MIT Pressurizer- ja Neptunus- erilliskokeita. Lisäksi rakennettiin malli Loviisan ydinvoimalaitoksen paineistimesta, jota käytettiin turbiinitrippitransientin simulointiin tarkoituksena selvittää mahdolliset voimalaitoksen ja koelaitteistojen mittakaavaerosta johtuvat vaikutukset APROSin paineistinlaskentaan. Kokeiden simuloinnissa testattiin erilaisia noodituksia ja mallinnusvaihtoehtoja, kuten entalpian ensimmäisen ja toisen kertaluvun diskretisointia, ja APROSin sekä TRACEn antamia tuloksia vertailtiin kattavasti toisiinsa. APROSin paineistinmallin lämmönsiirtokorrelaatioissa havaittiin merkittävä puute ja laskentatuloksiin saatiin huomattava parannus ottamalla käyttöön uusi seinämälauhtumismalli. Työssä tehdyt TRACE-simulaatiot ovat osa United States Nuclear Regulatory Commissionin kansainvälistä CAMP-koodinkehitys- ja validointiohjelmaa.

ACKNOWLEDGEMENTS

This work has been conducted at VTT Technical Research Centre of Finland at VTT Processes in the group of Nuclear Power Plant Technology and it was partially funded by the Finnish participation to the international CAMP program. I wish to express my gratitude to M.Sc. Ismo Karppinen, my supervisor and examiner at VTT and Professor Riitta Kyrki-Rajamäki, my examiner at Lappeenranta University of Technology. I also wish to thank research scientists Markku Hänninen and Jukka Ylijoki for their valuable instructions and cooperation in using APROS and senior research scientist Heikki Holmström for helping in the material acquisitions in the literature survey of the thesis and for introducing me to the CAMP program.

Espoo, November 17th, 2005

Eveliina Takasuo

TABLE OF CONTENTS

APPENDIX 1. PACTEL ATWS-10 – 13 STEAM SUPERHEAT

NOMENCLATURE

A	dimensionless parameter	
A	area	[m^2]
C_C	correction factor for droplet internal circulation	
c_p	heat capacity (constant pressure)	[J/kgK]
D_d	droplet Sauter mean diameter	[m]
D_H	hydraulic diameter	[m]
G	mass flux	[kg/m^{2}s]
g	gravitational acceleration	[m/s^2]
Gr	Grashof number	
h	specific enthalpy	[J/kg]
h	heat transfer coefficient	[W/m^{2}K]
h_{fg}	latent heat of vaporization	[J/kg]
h'_{lg}	modified latent heat	[J/kg]
K	interfacial heat transfer coefficient (APROS)	[kg/m^{3}s]
k	thermal conductivity	[W/m K]
L	length	[m]
Nu	Nusselt number	
p	pressure	[Pa]
Pe	Peclet number	
Pr	Prandtl number	
Re	Reynolds number	
St	Stanton number	
T	temperature	[°C]
T*	dimensionless droplet mixing cup temperature	
T_{sv}	saturation temperature corresponding steam partial pressure	
t_d	thermal boundary layer lifetime	
u	velocity	[m/s]
V	velocity	[m/s]
$V^*_{\max}$	dimensionless droplet maximum circulation velocity	
X_{TT}	Martinelli parameter	
x	quality	
x_e	equilibrium steam mass quality	

Greek

α	void fraction	
δ	droplet diameter	[m]
ε	emissivity	
κ	phasic viscosity ratio	
λ	Taylor characteristic wavelength	
μ	dynamic viscosity	[kg/ms]
ρ	density	[kg/m^3]
σ_r	Stefan-Boltzmann constant	[W/(m^{2}K^4)]

Subscripts

a	air or non-condensable gas
cell	related to mesh cell
ch	related to Chen correlation
cond	condensation
cr	critical
dr	related to Dougall-Rohsenow correlation
fBB	related to Bromley correlation
forc	forced convection
g	gas
i	interfacial
ig	interface-to-gas
il	interface-to-liquid
l	liquid
ne	flow without entrainment
NC	natural convection
r	relative, radiation
s	stratified flow
sat	saturated state
sh	related to Shah correlation
t	turbulent
TP	two phase
w	wall
wl	wall-to-liquid

ABBREVIATIONS

APROS	Advanced Process Simulation Environment
ATWS	Anticipated Transient Without Scram
BWR	Boiling Water Reactor
CAMP	Thermal Hydraulic Code Applications and Maintenance Program
HPIS	High-Pressure Injection System
INEEL	Idaho National Engineering & Environmental Laboratory
LOCA	Loss of Coolant Accident
LOFW	Loss of Feed Water accident
MIT	Massachusetts Institute of Technology
NPP	Nuclear Power Plant
PACTEL	Parallel Channel Test Loop
PWR	Pressurized Water Reactor
RELAP	Reactor Excursion and Leak Analysis Program
SBLOCA	Small Break Loss of Coolant accident
TRAC	Transient Reactor Analysis Code
TRACE	TRAC/RELAP Advanced Computational Engine
USNRC	Unites States Nuclear Regulatory Commission
VTT	Technical Research Centre of Finland
VVER	Voda Vodjanyi Energetitseskij Reaktor

1 INTRODUCTION

The capability of thermal hydraulic simulation software to predict pressurizer transients in nuclear reactors has generally not been good. Most often, improvements to the pressurizer calculation have been attempted by increasing the number of nodes in the model and using a smaller timestep. However, a potential exists to improve the pressurizer modeling significantly by incorporating more accurate heat transfer models into the code as was recently done in the RELAP-3D code (Weaver, 2004) by modifying the interfacial condensation model, and in the RELAP5/MOD3.3 code by using thermal front tracking (Prelewicz et al., 2005).

In this work assessment of the pressurizer model of APROS is performed. APROS is a multi-purpose process simulation environment which has been developed in Finland by VTT Processes (previously known as VTT Energy), VTT Industrial Systems and Fortum Power and Heat Ltd. APROS is suitable for design analysis, feasibility studies, accident analyses, testing of operation instructions and optimization and training purposes (Vihavainen et al., 1999). In Finland it has been widely used in simulating nuclear and conventional power plants. The main part of the experimental data chosen for code validation consists of six tests of the second series of the ATWS test sequence which was performed at the PACTEL test facility in Lappeenranta, Finland, in 1998. The PACTEL integral test facility is a volume-scaled (1:305) model of the Soviet-design VVER-440 PWR and it has been used for reactor thermal hydraulic modeling at the Lappeenranta University of Technology in co-operation with VTT (Tuunanen et al, 1998). The aim of the ATWS-10 to ATWS-13 experiments was to investigate steam compressibility under nearly isentropic compression. In the ATWS-20 and ATWS-21 tests the effect of pressurizer spray was studied (Riikonen, 1998).

Most of the separate effect tests for pressurizers which are used for code validation were conducted in the beginning of the 1980’s after the Three Mile Island accident had made the researcher community realize the importance of being able to predict the behavior of all the components in the nuclear power plant loop. Prior to the TMI-2 accident there had been not much interest in small break LOCAs and recovery procedures after such accidents since large break LOCAs were thought to be more severe. Nowadays it is clear that it is crucial to predict the pressure behavior during operational transients and recovery procedures in order to be able to take the necessary actions to restore the system to a safe state. For example, condensation in the pressurizer at the end of recovery procedures can make it difficult to reach the set point of the normal residual heat removal system (Aksan et al., 1993). The pressurizer separate effect tests of which data sets are available for large thermal hydraulic code validation are collected together in the Separate Effects Test Validation Matrix of the OECD Task Group for Thermal Hydraulic System Behavior (Aksan et al., 1993). From the tests presented in the Validation Matrix, the Neptunus Y05 test and the MIT pressurizer tests were selected for simulating in addition to the PACTEL ATWS tests. For the purpose of investigating the scaling effect on the pressurizer models one power plant scale pressurizer transient is also simulated. The transient is a turbine load decrease at Loviisa nuclear power plant which was used as a validation case for the operator training simulator at the power plant.

The second part of the Thesis consists of simulating the PACTEL, MIT pressurizer and the Neptunus experiment using TRACE code. The PACTEL ATWS simulations will be a part of the contribution of Finland to the international Code Applications and Maintenance Program (CAMP) of The US Nuclear Regulatory Commission. The CAMP program was started in 1992 as a continuation to the ICAP program whose goal was the assessment of the RELAP5, TRAC-PF and TRAC-BF codes. The Finnish participants of the current five-year CAMP program are VTT Processes, Teollisuuden Voima Ltd., the Finnish Radiation and Nuclear Safety Authority and Fortum Nuclear Services Ltd. TRACE is the flagship of the thermal hydraulic tools developed at the USNRC and it is designed to consolidate the capabilities of the three codes, TRAC-P, TRAC-B and RELAP into a modernized code with the capability to analyze system transients and small and large break LOCAs in both PWR and BWR nuclear power plants (USNRC, 2005). It is expected that analyzing the PACTEL experiments, which are more recent and well documented in comparison to the older pressurizer tests, using TRACE could provide a valuable addition to the separate effect validation cases of the code. Also, extensive comparisons between the results obtained by APROS and TRACE are made.

2 PRESSURIZER OPERATION DURING TRANSIENTS

In a PWR reactor a pressurizer is used to control the pressure of the primary circuit. A pressurizer consists of a steel tank which contains water in the lower section and steam in the upper section. The pressurizer is connected to the primary system by a surge line. There is a pressure-actuated spray nozzle at the top of the container and immersion-type electric heaters in the bottom. In case the coolant temperature increases, i.e. as a response to a decrease in the turbine power output, the coolant volume increases correspondingly and the pressurizer water level rises. The pressure increase activates the spray valve and water from a cold leg is sprayed to the pressurizer to limit the pressure by condensing some of the steam. When the coolant temperature in the primary system is decreased, i.e. as a result of a decrease in the electrical load on the plant, the volume of the coolant decreases and the pressurizer level drops which activates the heaters. Due to pressure drop some of the water in the pressurizer flashes to steam which reduces the pressure change in addition to the effect of heaters (Lamarsh et Baratta, 2001). The importance of the pressurizer in controlling the system is apparent considering that water is practically incompressible and a minor change in the fluid temperature can result in a significant change in the pressure. A schematic diagram of a typical pressurizer is presented in Fig. 1 (a). Figure 1 (b) summarizes the heat and mass transfer mechanisms present in the pressurizer for the control volumes of steam, hot water and cold water. Next, the different types of pressurizer transients and heat transfer phenomena which dominate the behavior of the pressurizer are introduced.

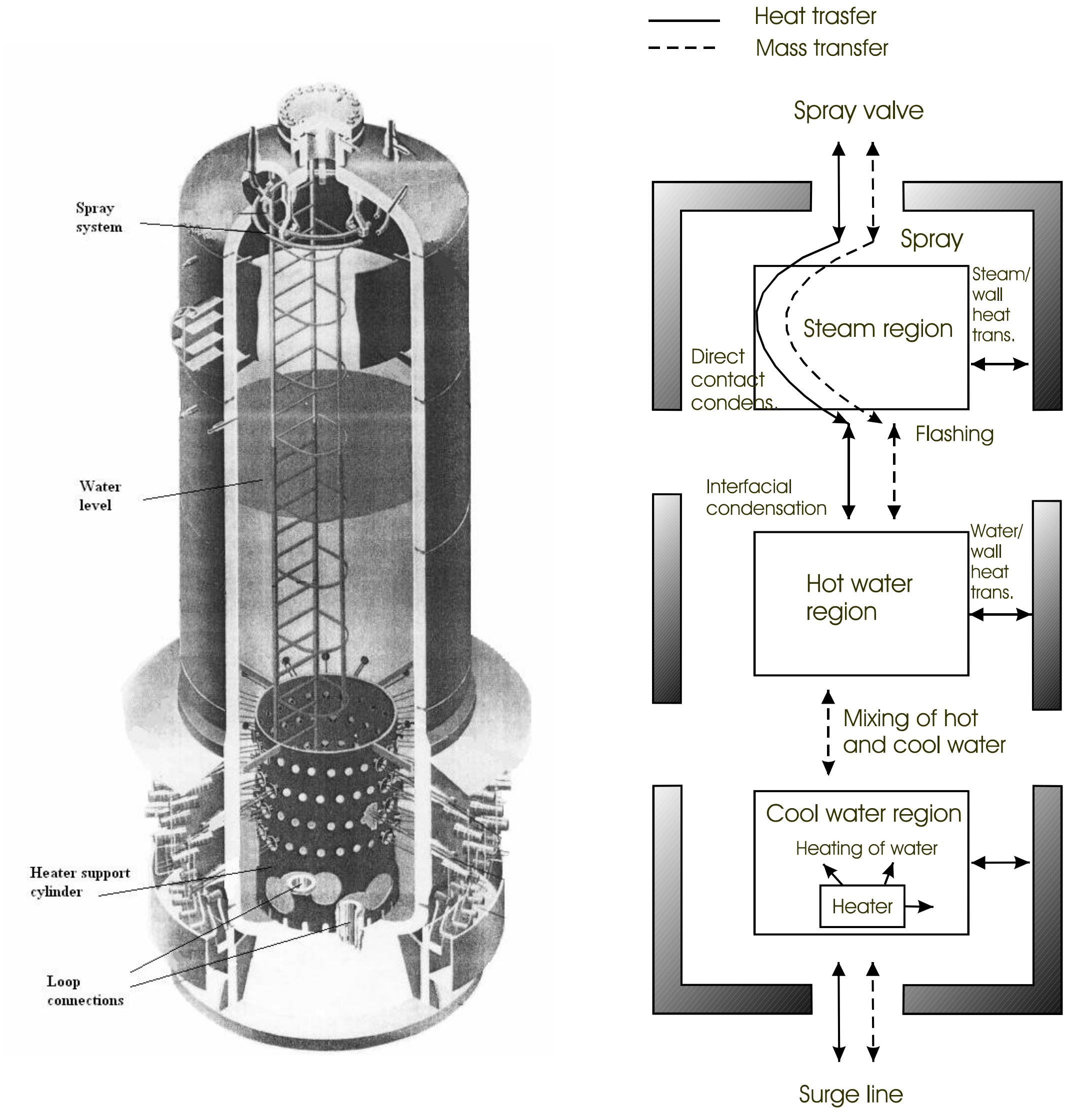

(a) (b)

Figure 1. (a) A PWR pressurizer. (b) Heat and mass transfer processes in the pressurizer.

2.1 Insurge

An example of a rapid pressurization of the primary system and injection of sub-cooled water into the pressurizer is a LOFW-ATWS during which the heat removal from the primary circuit is lost. The expansion of coolant volume raises the water level in the pressurizer as sub-cooled water is injected into the pressurizer. Under normal operation, the pressurizer is partially filled and water level is high enough that the buoyancy force of the saturated water prevents the injection jet from breaking through the water surface, and a clear stratification of hot and cool water occurs. Since the heat conductivity of water is small the cool water will remain at the bottom and the bulk of saturated water at the top. In this case, the increase of the water level results in the so-called piston effect in which the steam undergoes a nearly isentropic compression and becomes superheated. Also, the surge line hydraulics plays an important role in this case. In case the water level is low enough for the injection jet to disrupt the water surface the result is a fountain effect of sub-cooled water into the steam volume where depressurization occurs due to direct contact condensation of steam on the jet droplets.

The heat transfer phenomena present in an insurge transient are condensation and natural convection at the pressurizer walls, mixing or stratification of hot and cool water in the bottom section of the tank and condensation at the phase interface. Experimental studies have shown that the condensation at the wall and at the interface between the phases forms a thin layer of hot water on the interface which separates the rest of the water volume from steam and reduces interfacial condensation. Usually the effects of wall convection and interfacial heat transfer on the system behavior are negligible compared to the wall condensation and mixing and stratification in the water section (Kim, 1984).

2.2 Outsurge

The phenomena observed in a pressurizer outsurge are steam expansion, flashing and wall boiling. When the pressurizer level decreases because of outsurge of water to the primary circuit the steam volume is expanded and the steam pressure decreases. Following the depressurization, the saturation temperature decreases and the water becomes superheated which may lead to a rapid and violent evaporation process called flashing. Flashing of some of the water to steam effectively helps to maintain the pressure and slow the depressurization in the tank. Boiling at the wall occurs because the wall temperature is higher than the saturation temperature inside the tank. Also, forced convection is present at the lower section of the pressurizer wall during sub-cooled outsurge as the hot water region reaches the section of the wall which was previously cooled by the sub-cooled water. It has been shown that this plays a role in suppressing the flashing (Kim, 1984). The heat transfer by boiling and forced convection is insignificant compared to flashing.

2.3 Spray

When the spray valve is opened to control an undesired pressure rise two main phenomena occurring in the pressurizer are direct contact condensation between spray droplets and heating of the spray droplets due to direct heat transfer from the pressurizer wall. It has been experimentally observed that the temperature of the spray water increases and reaches the saturation temperature very quickly after entering the pressurizer (Kim, 1984). The spray parameters which play the most important role in the effectiveness of the cooling are droplet size and the angle of the spray. The condensation depends on the surface area, and the smaller the droplets the larger the condensation area. In addition, droplet velocity, pressurizer pressure, the amounts of steam and water in the tank and the distance from the spray nozzle to the water level have an effect on the phenomenon. In some nuclear power plants, such as Loviisa VVER-440 reactors, a cylindrical shield (spray cylinder) is installed into the pressurizer to prevent the spray from hitting the pressurizer wall directly and to protect the wall from thermal shock.

2.4 Heaters

The purpose of the heaters is to limit an undesired pressure drop by warming up the water section of the pressurizer. The pressure increases along the temperature increase as the fluid volume increases. The heat transfer mechanisms present are conduction, convection and possibly boiling. Heat is transferred by convection from the heater surface to the surrounding water. If the temperature close to the surface is higher than the saturation temperature film boiling occurs.

3 EXPERIMENTS

The experiments sequences selected for simulations cover both the insurge and outsurge transients using different initial parameters and spray cooling. The main focus is on the ATWS-10 - 13 and ATWS-20 - 21 tests which were conducted at the PACTEL test facility in Lappeenranta, Finland, in 1998 (Riikonen, 1998). Based on a literature survey, the results of the aforementioned PACTEL ATWS tests are the latest experimental data available of this type of tests in which the pressurizer component is examined separately.

The MIT pressurizer test and Neptunus Y05 test are found in the OECD Separate Effect Test Matrix for thermal hydraulic code validation (Aksan et al., 1993). The MIT pressurizer tests were performed at the Department of Nuclear Engineering at MIT, USA during 1983 and 1984. The transients include insurge into a partially full pressurizer tank, outsurge, insurge to a hot tank, outsurge after insurge and empty tank insurge (Kim et Griffith, 1987). The Neptunus pressurizer was operational between 1965 and 1970 in the

Laboratory for Thermal Power Engineering at the Delft University of Technology, the Netherlands. The test Y05 simulated four successive insurge-outsurge transients combined with spray (Peterson, 1984).

3.1 PACTEL Pressurizer component

The pressurizer component of the PACTEL test facility is a steel container with the total height of 8.8 m and the inner diameter of 13.97 cm. The pressurizer is connected by the surge line to the Loop 1 of the facility, and a spray line is installed on the top of the tank. The volume scaling ratio of the pressurizer, as well as the other components of the facility, is 1:305 and the elevation scale is 1:1 compared to the reference reactor of the facility which is the six-loop VVER-440 type PWR currently in operation in Loviisa. The total heater power is 13kW which is distributed by three electrical heaters whose nominal powers are 2kW, 4kW and 7kW (Tuunanen et al., 1998). A general view of the test facility is presented in Fig. 2. The schematic of the PACTEL pressurizer is shown in Fig. 3 and the spray nozzle in Fig. 4.

The instrumentation of the test facility consists of temperature, pressure, differential pressure and flow transducers. In the pressurizer, there are seven fluid temperature measurements located in the centerline of the pressurizer, four structure temperature measurements, three of which are at the heaters and one in the upper part of the pressurizer, and six differential pressure transducers. A pressure transducer is installed on the top of the pressurizer. The temperature measurements of the facility use K-type mineral insulated thermocouples with the diameter varying from 0.5 mm to 3 mm, depending on the measurement location. (Tuunanen et al., 1998)

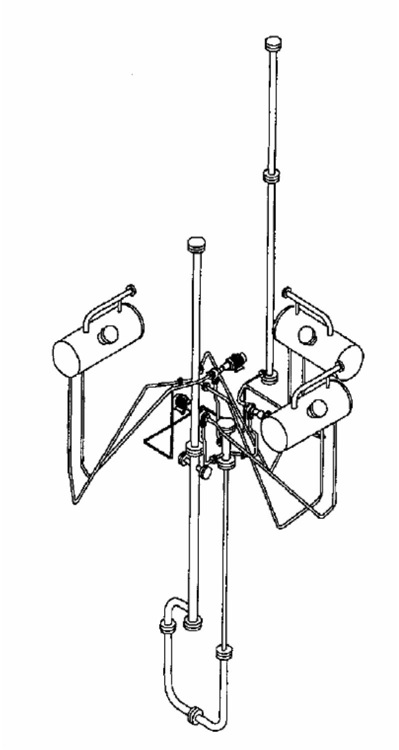

Figure 2. PACTEL test facility (Tuunanen et al, 1998).

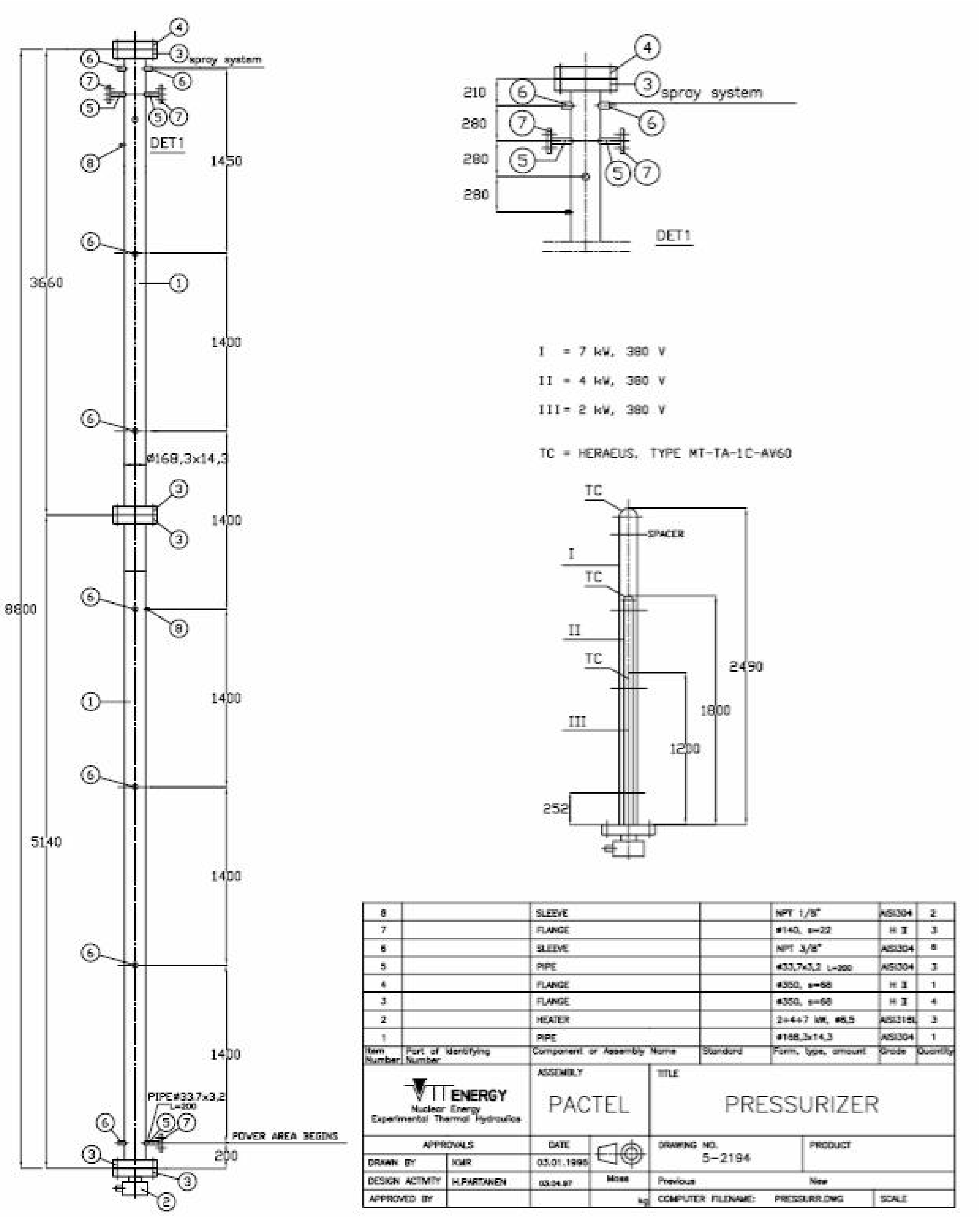

8		SLEEVE		NPT 1/8"	AISI304	2
7		FLANGE		Ø140, s=22	H II	3
6		SLEEVE		NPT 3/8"	AISI304	8
5		PIPE		Ø33,7x3,2 L=200	AISI304	3
4		FLANGE		Ø350, s=68	H II	1
3		FLANGE		Ø350, s=68	H II	4
2		HEATER		2+4+7 kW, Ø8,5	AISI316L	3
1		PIPE		Ø168,3x14,3	AISI304	1
Item Number	Part of Identifying Number	Component or Assembly Name	Standard	Form, type, amount	Grade	Quantity

VTT ENERGY
Nuclear Energy
Experimental Thermal Hydraulics

ASSEMBLY
PACTEL

TITLE
PRESSURIZER

APPROVALS
DATE
DRAWN BY KMR 03.01.1998
DESIGN ACTIVITY H.PARTANEN 03.04.97
APPROVED BY
Mass
kg
DRAWING NO. 5-2194
PRODUCT
Previous
New
COMPUTER FILENAME: PRESSURR.DWG
SCALE

Figure 3. Schematic of the pressurizer of the PACTEL test facility (Tuunanen et al., 1998).

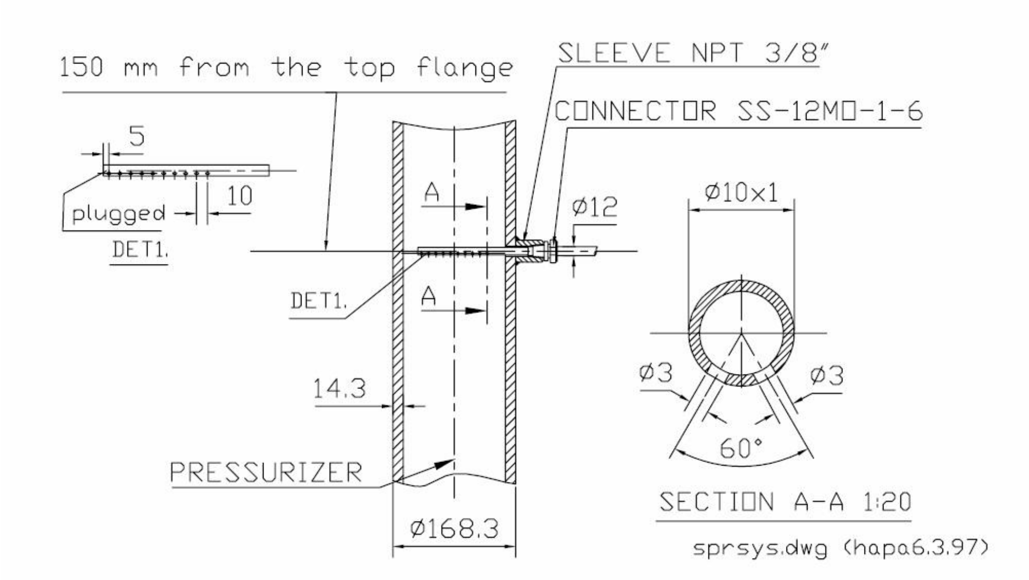

Figure 4. PACTEL pressurizer spray nozzle (Tuunanen et al, 1998).

3.1.1 PACTEL ATWS-10 – 13

The objective of the experiments from ATWS-10 to ATWS-13 was to study steam compression under fast nearly isentropic compression. The procedure of the experiments was as follows. A 100 s steady-state period was run with the heater power being 4 kW. At 100s the heater was switched off and injection of nearly saturated water into the pressurizer using the high pressure piston pump began. A suitable core power was maintained to prevent the cooling of the facility. When the pressure was reaching 7.8 MPa the injection was stopped and draining began. A draining valve of 2 mm in diameter was opened in the cold leg. The primary circuit and the other components of the facility were used only to inject and drain water to and from the pressurizer. A low core power was maintained to prevent cooling of the facility. The initial state at the beginning of the experiments is given in Table 1. The operator actions during the experiments are presented in Table 2. (Riikonen, 1998).

Table 1. Initial parameters for the ATWS 10 – 13 tests.

Parameter	**ATWS-10**	**ATWS-11**	**ATWS-12**	**ATWS-13**
Pressure	5.9 MPa	5.9 MPa	6.0 MPa	6.0 MPa
Water level	3.3 m	3.5 m	3.5 m	5.0 m
Mass flow rate	0.367 kg/s	0.217 kg/s	0.100 kg/s	0.100 kg/s
Core power	380 kW	245 kW	150 kW	150 kW

Table 2. Operator actions during the experiments.

Event	**ATWS-10**	**ATWS-11**	**ATWS-12**	**ATWS-13**
Test begins	0 s	0 s	0 s	0 s
Heaters off	100 s	100 s	100 s	100 s
Power increase	116 s	111 s	109 s	109 s
Insurge on	120 s	119 s	117 s	119 s
Insurge stopped	221 s	297 s	570 s	444 s
Draining begins	221 s	297 s	580 s	444 s
Core power off	221 s	305 s	602 s	456 s
Draining ends	407 s	502 s	813 s	593 s
End of test	500 s	600 s	1000 s	700 s

The analysis of the relationship between steam pressure and volume during a polytropic process showed that the steam reality coefficient ranged from 0.70 to 0.82. The highest values were obtained for the fastest transient (ATWS-10) and the smallest for the slowest process (ATWS-13). The steam temperature followed the saturation temperature until at the end of the expansion the steam began to superheat slightly. During compression the condensed mass was 56%-64% of the initial mass. At the end of the experiment the steam mass was reduced to 82%-89% of the initial value. (Riikonen, 1998)

3.1.2 PACTEL ATWS-20 - 21

The effect of the pressurizer spray was studied in the experiments. After a steady-state period water (20°C-25°C) was sprayed to the pressurizer through the spray line. The pressurizer heaters were controlled by automation. The spray was stopped when the pressure was reaching 6.0 MPa. In the ATWS-20 experiment all the heaters were on at 660s and the pressure began to increase. To prevent further pressure increase the heaters were switched off between 890 s and 906 s (Riikonen, 1998). The initial state and the operator actions during the test are given in table 3 and 4, respectively.

Table 3. Initial parameters for the ATWS – 20-21 tests.

Parameter	ATWS-20	ATWS-21
Pressure	7.5 MPa	7.5 MPa
Water level	5.6 m	5.6 m
Mass flow rate	0.00667 kg/s	0.0167 kg/s

Table 4. Operator actions during the experiments.

Event	ATWS-20	ATWS-21
Test begins	0 s	0 s
Spray on	100 s	200 s
7 kW heater off	890 s	-
4 kW heater off	903 s	-
2 kW heater off	906 s	-
Spray off	1500 s	1220 s
End of test	1500 s	1220 s

Similarly to the previous tests, the steam temperature followed saturation temperature. In addition to the spray condensation, there was condensation of steam on the pressurizer walls and on the water surface. The condensed mass was 35%-55% of the initial mass.

3.2 MIT Pressurizer

The MIT pressurizer experiment series was performed to increase fundamental understanding on important phenomena occurring in the pressurizer. A general analytical model of the pressurizer was prepared, based on which the pressure-time behavior of the pressurizer could be predicted (Kim, 1984).

The main components of the test facility are two cylindrical stainless steel pressure vessels, namely “primary tank” and “storage tank” with associated piping, instrumentation and a non-condensable gas injection rig. The height of the primary tank is 1.143 m and inside diameter is 0.203 m. The thickness of the stainless steel wall is 9.5 mm. The tank has a sight glass for measuring the collapsed water level, six circular windows of 6.35 cm in diameter, a pressure gauge, a pressure transducer, a vent, a sparger and six electrical heaters. The schematic of the test apparatus is presented in Fig. 5 (Kim et Griffith, 1987).

The measurement system consists of thirteen thermocouples installed at the center of the tank and eight thermocouples on the outside wall at different heights from the bottom of the tank, an ASME standard orifice and a pressure transducer for measuring surge flow rate, and a pressure transducer for the pressurizer pressure. The thermocouples are of the type 304-T-MO-1.5mm manufactured by Omega Co (Kim, 1984). The accuracy of the type T thermocouples for the temperature range of 0 – 350℃ is ±0.75% according to the American Limits of Error Standard ASTM E230-ANSI MC96.1. The accuracy of the two Validyne DP pressure transducers is ±0.25% according to the manufacturer (Validyne Engineering).

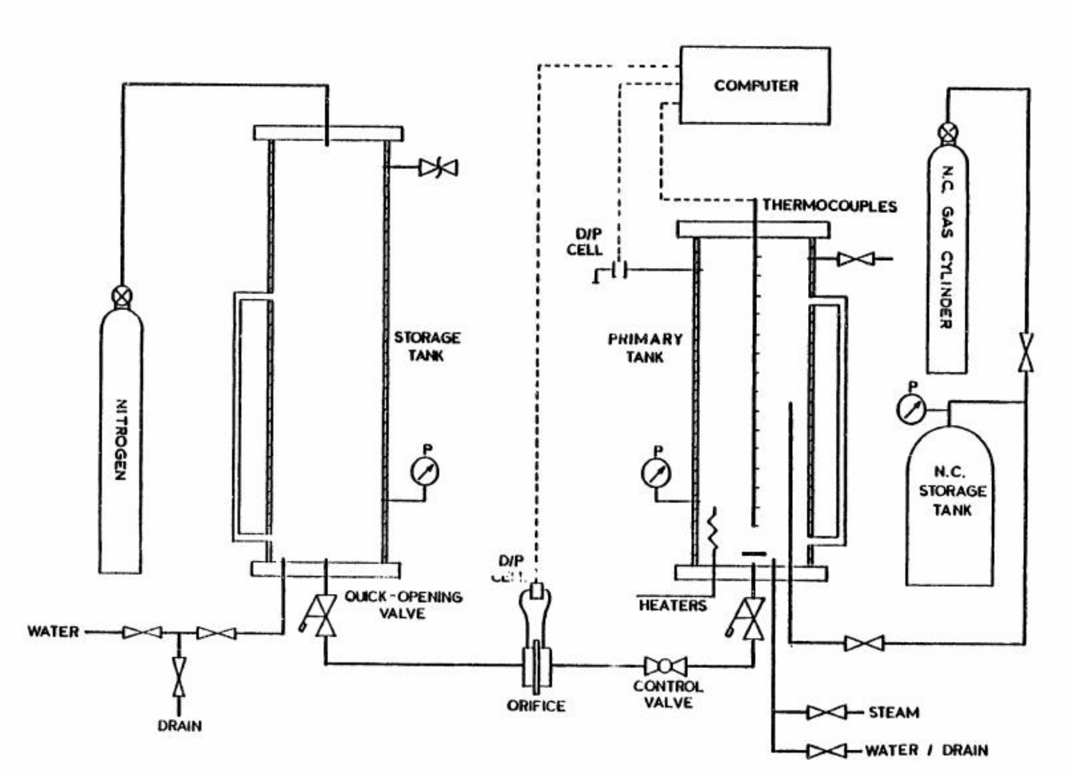

Figure 5. Schematic diagram of the MIT pressurizer test apparatus. (Kim, 1984)

The behavior of the pressurizer was investigated by the following tests: partially full insurge, outsurge, insurge to a hot tank, outsurge after insurge and empty tank insurge. Prior to the main experiments, preliminary experiments were performed in order to calibrate the instruments, to set up the software and compute the heat loss from the apparatus to the environment. In addition, some insurge tests were executed to investigate the radial temperature distribution and mixing of hot and cold water. The initial state and some of the final state values, which are presented in Appendices A to E in Kim's Thesis (1984), are given in Table 5 for each of the experiments.

Table 5. MIT pressurizer test parameters.

Parameter	**Part full insurge**	**Outsurge**	**Hot tank insurge**	**Outsurge after ins.**	**Empty tank insurge**
Initial pressure	0.696 MPa	0.867 MPa	0.784 MPa	0.698 MPa	0.869 Mpa
Initial water level	0.35 m	0.75 m	0.28 m	0.52 m	0.24 m
Pressure before insurge	-	-	0.596 MPa	-	0.776 MPa
Pressure after insurge	-	-	-	-	0.896 MPa
Final water level	0.86 m	0.24 m	0.89 m	0.20 m	0.71 m
Final pressure	-	0.817 MPa	0.852 MPa	-	0.376 MPa

3.2.1 Insurge to a partially full tank

The objective of the partially full insurge and outsurge experiments was to simulate a case where the system is initially at equilibrium. The tank was filled with saturated water to about 1/3 of the tank height and cold water was injected from the bottom of the pressurizer until the water level reached about 2/3 of the tank height. The experiment results showed that the incoming cold water and the hot water in the pressurizer are stratified and that the gas phase is never more than slightly superheated. The temperature profile measured outside of the wall implies that a significant amount of heat is removed from the vapor phase to the wall, and also heat is conducted from the bottom part of the wall to the cooler liquid present in the bottom. The most important heat transfer mechanism during the transient is wall condensation. (Kim, 1984)

3.2.2 Outsurge

In the simple outsurge experiment saturated water was discharged from the bottom of the tank. It was observed that flashing on both the wall and the heaters helps to maintain pressure inside the tank effectively resulting in a very small pressure drop compared to the increase in the steam volume. When the wall is submerged or wet the drop of the temperature inside the wall follows closely the decrease of saturation temperature. After the wall is dried out the wall temperature drops remarkably slower. The axial temperature profile during the test shows that before the outsurge, the temperature of the upper part of the water is slightly higher than that of the lower part. As the outsurge proceeds the temperature profile becomes flat and finally the temperature of the lower part becomes slightly higher, presumably due to a higher hydrostatic pressure in the lower part of the tank. (Kim, 1984)

3.2.3 Insurge to a hot tank

In this experiment, a case where the pressurizer wall temperature is different than the saturation temperature was investigated. A hot wall was made by venting steam so that the pressure and saturation temperature decreased while the wall temperature remained nearly constant. It was observed that the natural convection between the dry wall and steam is negligible so that the process is practically isentropic as long as the wall temperature is higher than the saturation temperature. (Kim, 1984)

3.2.4 Outsurge after insurge

This experiment simulated a case where the water temperature is not uniform. The insurge stage of the test is identical to the simple insurge transient but the outsurge pressure behavior shows a significant difference. In the beginning of the outsurge the bulk of water is not initially saturated but cold water exists in the bottom of the tank. Before flashing can occur the pressure must decrease below saturation pressure for the existing temperature which in this case takes longer than in the simple outsurge transient where all the water is saturated and immediately available for flashing. When the pressure reaches the saturation pressure corresponding to the initial temperature, the heat transfer to the cold wall reduces the flashing, resulting in a more rapid pressure drop than in the simple outsurge case. (Kim, 1984)

3.2.5 Empty tank insurge

Usually, the water level in the pressurizer is high enough to prevent the insurge jet from the bottom of the tank from disrupting the steam-water interface. However, if the momentum of the insurge water is enough to penetrate the water surface, the heat transfer at the interface is drastically improved which may lead to a large enough drop in the pressure to activate the safety injection system. This could be the initiating event leading to a pressurized thermal shock. The purpose of this experiment was to investigate how significant this pressure drop is. It was observed that the pressure response of the empty tank insurge is quite sensitive to the initial hot water depth. In this case the scaling effect is significant, firstly, because in this type of a low pressure system the volume internal energy capacity is much lower than that of high pressure steam, which results in a remarkably more drastic pressure drop than in a full-scale high pressure system (Kim, 1984). Secondly, the wall heat capacity is smaller and the relative heat losses are greater than in a full-scale system.

3.3 Neptunus pressurizer

The schematic of the Neptunus pressurizer test facility is shown in Fig. 6. The carbon steel vessel is of 2.51 m in height and 0.8 m in inside diameter. The surge line connection can be seen in the bottom of the vessel and spray nozzle on the top. The surge line nozzle is 8.4 cm in diameter and the spray line nozzle 2.7 cm. One pressure and four fluid temperature measurements are reported of the facility but the exact positions and type of the transducers have not been documented. Initially, in the Y05 test the pressurizer was partially filled with water (1.12 m) at 327ºC. An insurge of 275ºC water flowed into the tank, followed shortly by the activation of spray. Four similar successive insurges and outsurges combined with spray injection during insurge were performed at 50 s intervals. (Peterson, 1984). The details of the test can be seen in Chapter 6, Section 6.4 in which the simulation results are presented.

Peterson (1984) analyzed the Y05 test using TRAC-PF1/MOD1 code as a part of the TRAC independent assessment project of the time at Sandia National Laboratories, United States. Peterson studied three different nodalization options: a 13-cell and a 4-cell uniform-node model in which the PRIZER component represented the container, a 13-cell pressurizer which consisted of two PRIZER components and a PIPE component and a model of three PIPE components. All the models computed the maximum pressure and the fluid temperature to be too high for each insurge but a good agreement with the measured minimum pressure was found. The results from each of the models showed no significant differences.

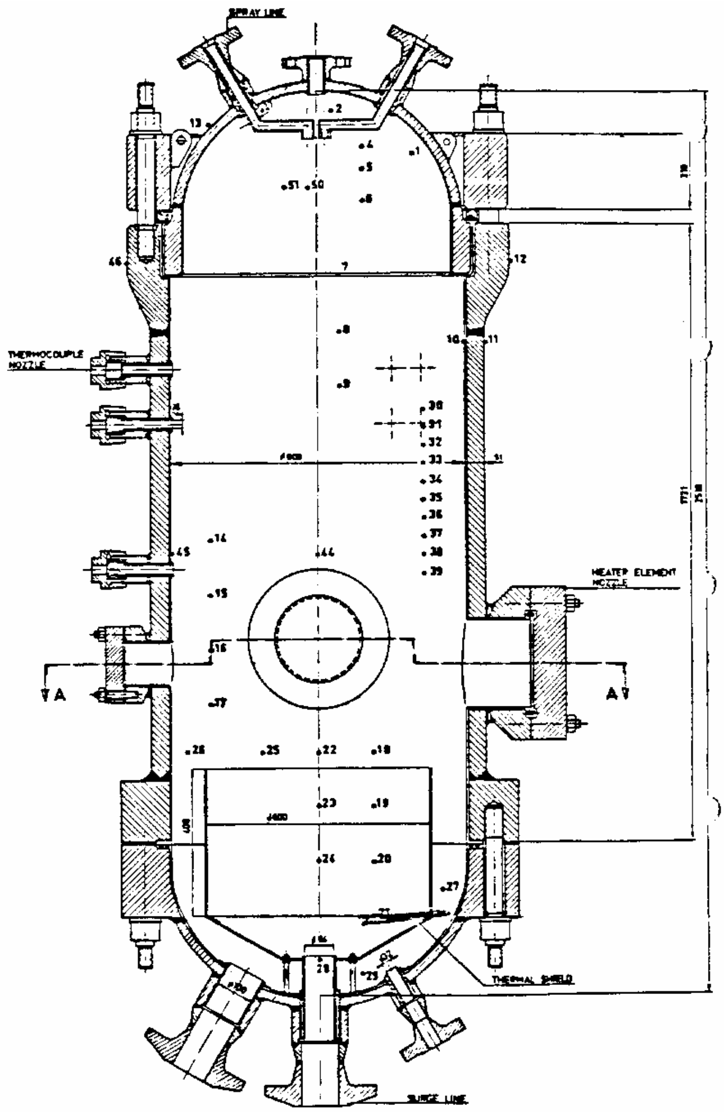

Figure 6. The Neptunus pressurizer test facility (Peterson, 1984).

3.4 Loviisa pressurizer

In addition to the tests described in the previous section, one power plant-scale transient is selected for simulation in order to examine the effect of scaling on the pressure response. Some measurement data recorded at the Loviisa nuclear power plant in Loviisa, Finland, was acquired from Fortum Power and Heat utility which operates the two VVER-440 reactor units in Loviisa. The modeled transient is a decrease in the turbine loading where the turbine power was decreased from the full power of 109 % to the level corresponding the internal load. The test was initiated by setting the turbine power control to manual and opening three of the four turbine by-pass valves. When the reactor power had decreased to 80 %, of the normal operation value, approximately 80 seconds after the initiation of the transient, the reactor power was set to manual control and maintained constant for about 40 seconds which after it was decreased to 60 % for the rest of the transient. The last of the turbine by-pass valves was demanded to open at about 400 s. The transient was originally used as a validation case for the Loviisa training simulator in 1998. Characteristics of the transient are a fast primary pressure rise which rapidly turns into a drastic pressure drop as the primary system cools down and a more stable pressure increase following the gradual closing of the by-pass valves. In this study, a separate model of the pressurizer of the plant is generated and the other components of the primary system are reduced to boundary conditions which either provide injection water to the pressurizer or remove water from the pressurizer. Thus, the analysis is very concise and covers only the part of the transient which is of the current interest, the pressurizer.

The Loviisa pressurizer total volume is 37.8 m^2 and it is connected to the hot legs of loops number 3 and 4 by two 209 mm diameter surge lines. Two pipelines feed water from the cold legs to the spray valves. The maximum capacity of the spray valves is 50 kg/s. There is also an additional spray line connected to the HPIS with a capacity of 15 kg/s. The electrical heaters are divided into 7 groups and their total power is 1620 kW. In a case of fast pressurization the power operated relief valve and two safety valves protect the system from a too high pressure. (Yrjölä, 1992)

4 MODELING OF PRESSURIZER USING APROS

The tests described in the previous chapter are simulated using the APROS six-equation model which solves the mass, momentum and energy equations for both liquid and gas phases. The GRADES application (Graphical user interface of APROS) is used for modeling and controlling the simulations. There are three different levels in the component definition hierarchy of APROS, namely process level, process component level and calculation level. The process component level is the main operation level of the user. The user manipulates this level via GRADES, for example, by adding and removing component symbols on the GRADES workspace. The basic calculation level is the level where the calculation engine operates in terms of elementary components such as branches and nodes.

The experiments of most interest are the PACTEL ATWS test sequences. The PACTEL ATWS experiments are used to test the capabilities of the heat transfer models and to find an optimal nodalization for the insurge, outsurge and spray calculations. The PACTEL pressurizer model is the basis for thermal stratification, simulation set-up and numerical discretization considerations. The MIT and the Neptunus tests are modeled using only one base case nodalization and they are compared to the PACTEL ATWS calculation cases in order to assess the results more reliably and find out whether any significant facility- or test-specific differences, for example related to scaling, exist in the simulations of the different tests. The Loviisa turbine trip transient is also modeled using the base model.

4.1 Nodalization schemes

The nodalization of the pressurizer is quite simple, usually the pressurizer model consists of a vertical column of uniform nodes. In the GRADES component library a default pressurizer component is available, which is a convenient way to model the pressurizer.

The special options of the component include generating the heat structures representing pressurizer wall and the heater, and the spray cylinder. If the spray cylinder option is enabled two parallel stacks of nodes are created, where the inner cylindrical nodes represent the volume within the spray cylinder, and the remaining annular channel is the space between the spray cylinder and the wall. If desired, the system also creates the device controller for controlling the heating power of the heater. Different kinds of process components can be connected to the connection points of the pressurizer. The connection points are defined by the user by giving the elevation of the points (APROS Documentation).

Another possibility is to build the model using separate node components and heat structures which represent the wall. Using separate nodes the analyst can build the nodalization however necessary, i.e. using nodes of different size, and use as many channels as needed. For example, the PACTEL test facility model currently in use at VTT uses two node channels to make sure that the mixing of warm water, heated by the heaters, into the cooler water volume is simulated correctly. The third possibility is to create a vertical pipe component, or more conveniently, a pipe with heat structure, to represent the pressurizer and the pressurizer wall. The advantage of these two modeling alternatives is that they allow more flexibility in the nodalization. On the other hand, the pre-generated pressurizer component is less laborious and useful especially as a part of large thermal hydraulic system models such as primary and secondary circulation systems of nuclear power plants.

The base case model for the PACTEL pressurizer in this study is a 30-node pressurizer component. Currently, there is a restriction in the APROS code which limits the amount of pressurizer nodes to thirty. A surge line modeled using a heat pipe component (a simple pipe component without the heat structure is also acceptable) is attached to the bottom connection point of the component. Below the surge line there is a branch and an external point which are excluded from the simulation to function as boundary conditions. The external point is used to define the temperature and pressure of the primary system or a reservoir from which water is injected into the pressurizer. A fixed mass flow rate is given to the branch component according to the test parameter. In the PACTEL test facility the mass flow is maintained by the high pressure injection pump.

For outsurge transients, a valve is attached to the surge line close to the pressurizer tank. The water is discharged through the valve to the environment which is modeled by a 2-equation model point “air”. The label “air” refers to the material being defined as air. Since the point is excluded from the simulation, it is irrelevant whether water-steam mixture or air is used. The valve diameter is 2 mm which corresponds to the size of the discharge orifice located in a cold leg of the PACTEL facility. In the simulations, the valve is set to be a boundary condition in which the average outflow rate obtained from the experimental data is given. This is because it is easier to use the measured flow directly to ensure that the conditions are same as in the tests, rather than model the actual geometry and the flow resistance of the orifice. The spray line is modeled by a valve and a pipe connected to a boundary condition. The hydraulic diameter of the pipe is set to 3 mm since the spray is discharged through the 20 small orifices seen in Fig. 4. The GRADES layout of the PACTEL pressurizer model is shown in Fig. 7. The other test facility models and the Loviisa pressurizer model are built using the same method as the PACTEL model described above.

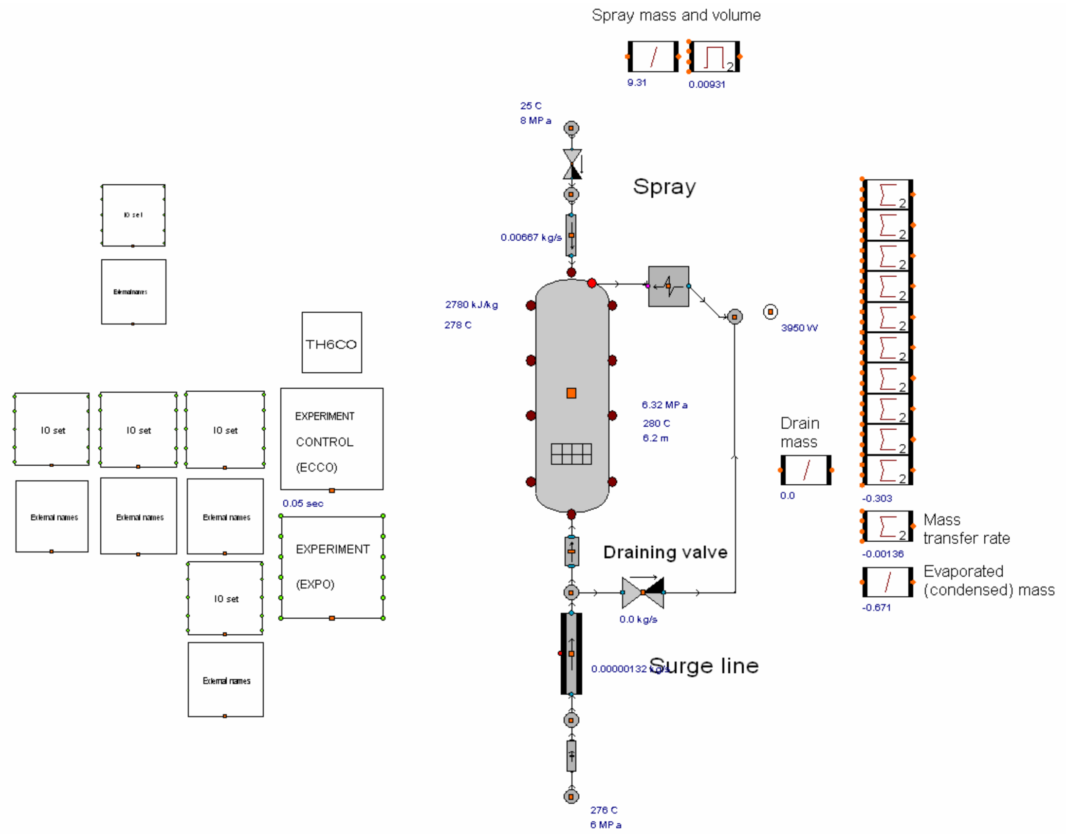

Figure 7. GRADES layout of the pressurizer net, including boundary condition components and IO set modules for output files. Note that, for better visualization, the width-length scale of the pressurizer and the piping is not realistic.

In addition to the 30-node base model, the ATWS-10 test is simulated using a model of 3, 10 and 100 nodes in order to find out the number of nodes enough to achieve a reasonable accuracy and to see if 30 nodes are enough for the pressurizer simulations. The 100-node case must be modeled using a pipe with heat structure component. The nodalization scheme for the PACTEL pressurizer base model and the other models are shown in Figs. 8, 9, 10 and 11.

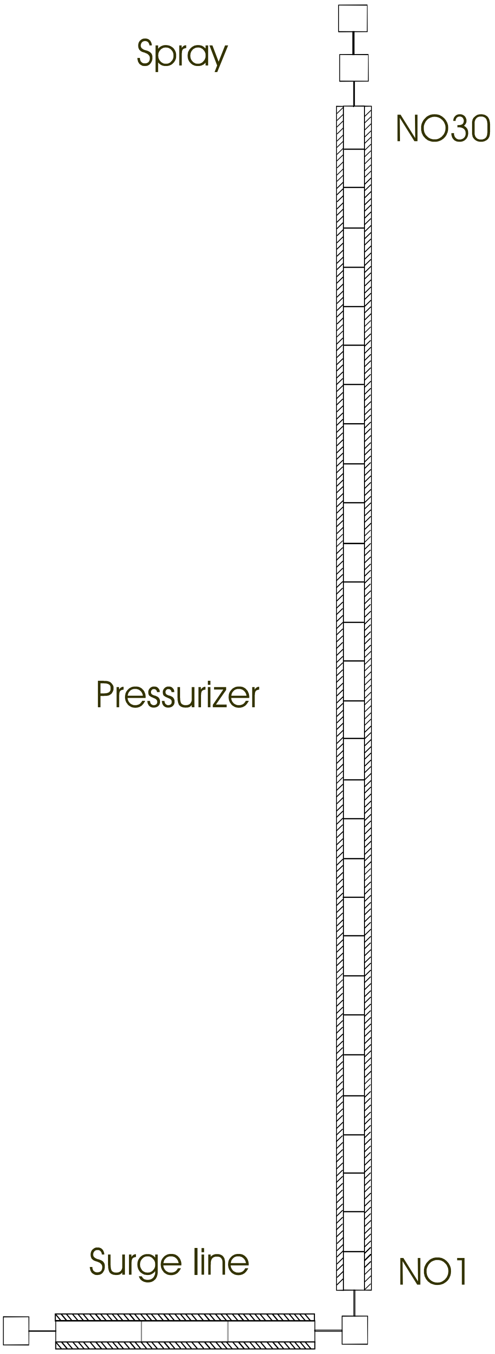

Figure 8. Base model nodalization.

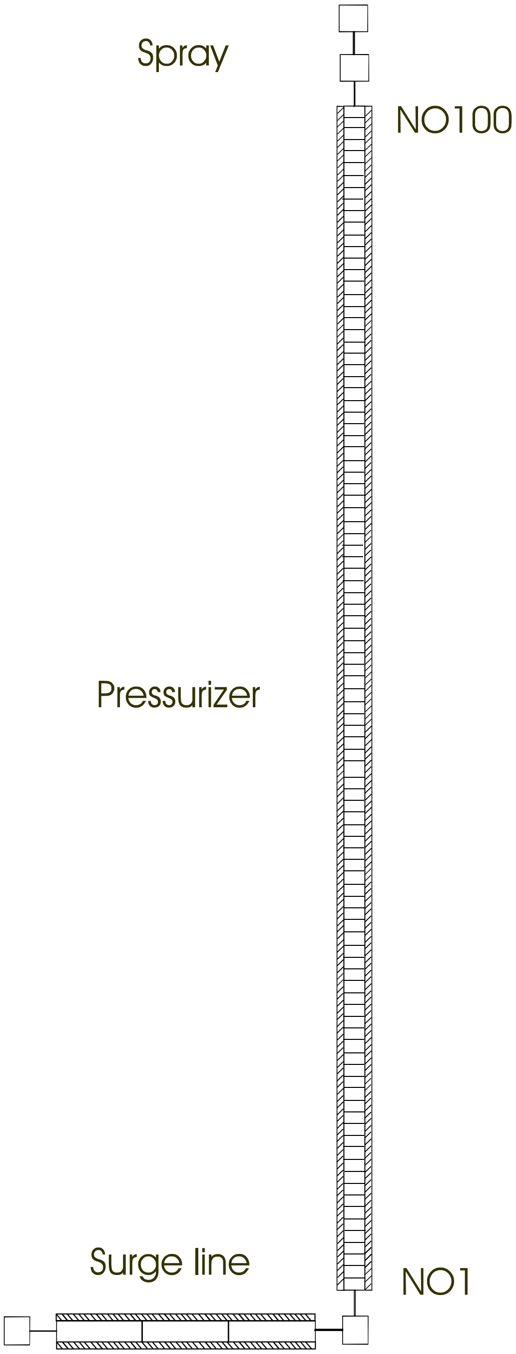

Figure 9. 100-node model nodalization.

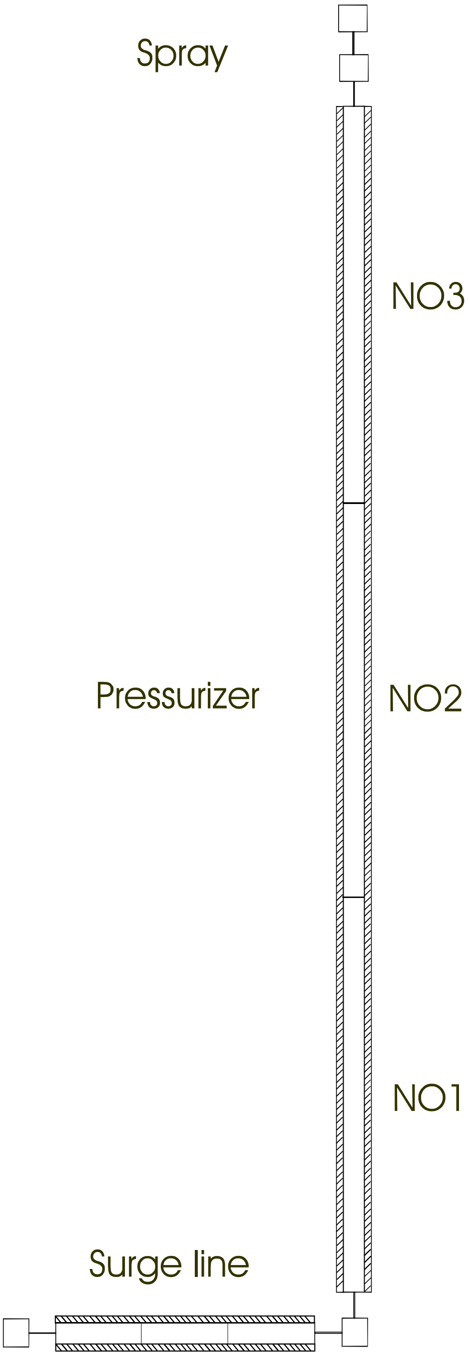

Figure 10. 3-node model nodalization.

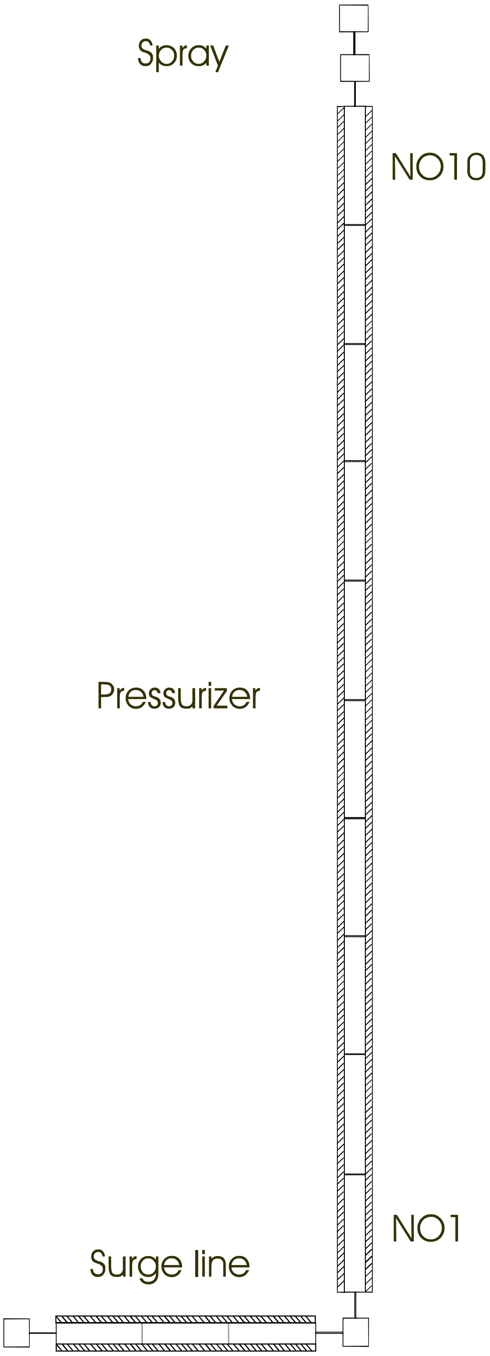

Figure 11. 10-node model nodalization.

4.2 Heat structures

APROS uses heat transfer modules to calculate heat flow between heat structure nodes and thermal hydraulic nodes. The heat transfer coefficient can be either calculated or given. A cylindrical heat structure representing the pressurizer wall is generated automatically if the thickness of the wall is given to the pressurizer component. If the pressurizer is modeled using a pipe without heat structure or separate node components a heat structure must be added separately. In all the pressurizer models in this study the pressurizer wall is divided into five radial heat transfer nodes. To simulate the heat losses to the environment a measured heat transfer coefficient is given for the heat transfer between the wall and the point “air”. For pressurizers the axial number of nodes is always the same as the number of thermal hydraulic nodes in the component. The thermal properties of the wall are defined by choosing the wall material from the material database.

In the case of the 100-node model the heat transfer component representing the heat losses from the pressurizer to the environment is connected to the “heat point” of the pipe component. Simulating the heat transfer from the outer wall of a component containing more than 30 axial heat nodes is a little problematic since the maximum number of calculation level heat transfer nodes which can be connected to a heat point module is 30. This is also true for the amount of heat transfer modules connected to single heat transfer component. In this model there are 102 outer nodes in the axial node rows (including a heat transfer node on the top and at the bottom of the pipe). This problem was solved by manually creating three additional heat point modules on the APROS calculation level and connecting the heat transfer nodes, which were not yet connected to any heat point, to them. Now each of the four heat points was connected to a heat transfer component. Thus also three “additional” heat transfer components were needed to create a connection between all the outer surface nodes and the point “air”.

4.3 Heat transfer models

In this section, the principle of heat transfer calculations and different heat transfer correlations in APROS of relevance to the pressurizer simulations are presented. In the six-equation model the wall heat transfer correlation is selected based on the wall, fluid and saturation temperatures, void fraction, critical heat flux and minimum film boiling temperature. Depending on the values of these parameters one of three heat transfer zones is selected. If the void fraction is over 0.99999 it is assumed that dry out occurs and the wall is in contact with the gas phase only (zone 3). Otherwise wet wall (zone 1) is selected if the wall temperature is less than the saturation temperature. If the wall temperature is higher than the saturation temperature the calculated heat flux is compared to the critical heat flux. In case the critical heat flux is exceeded, the heat transfer zone is set to 2 (transition zone) or 3. If the wall temperature is less than the minimum film boiling temperature the heat transfer zone is 2, otherwise zone 3 is selected. After a dry out and boiling crisis the heat transfer zone is changed back to 1 only until the wall temperature decreases below the saturation temperature (Hänninen et Ylijoki, 2004).

The heat transfer at the interface of gas and liquid is calculated separately for both phases. The heat transfer coefficient between gas and interface is calculated using the Lee-Ryley correlation for both superheated and sub-cooled steam. The heat transfer between liquid and interface is computed for evaporation and different modes of condensation. The evaporation heat transfer coefficient model is based on comprehensive critical flow tests at the SUPER MOBY DICK and Marviken test facilities (Bestion, 1990). The condensation correlation is selected based on the flow regime (flow without entrainment, droplet flow and stratified flow). For flow without entrainment, either Shah or modified Chen correlation can be chosen. The correlation for condensation in the droplet flow is a classical forced convection heat transfer model, and the correlation for stratified flow regimes is derived from the COSI experiment data. (Bestion, 1990)

4.3.1 Condensation

4.3.1.1. Shah correlation

In the pressurizer film condensation occurs when the wall temperature is lower than the steam temperature in the steam region of the pressurizer. Film condensation at the pressurizer walls is the dominating heat transfer mechanism for example during insurge transients. There are two options in APROS for calculating film condensation heat transfer, namely the Shah and the Chen correlation. The Shah correlation is the default correlation to be used for wall condensation. The Shah correlation calculates the interfacial heat transfer coefficient according to Eq. (1).

$$K_{il} = \frac{0.092\,\mathrm{Re}_{l,t}^{0.8}}{D_H^2 c_{pl}} \left[(1-x_e)^{0.8} + 3.8 x_e^{0.76} (1-x_e)^{0.04} \left(\frac{p_{cr}}{p} \right)^{0.38} \right] \tag{1}$$

The liquid Reynolds number Re_l is

$$\mathrm{Re}_{l,t} = \frac{G D_H}{\mu_l} \tag{2}$$

The original Shah correlation (Shah, 1979) has been multiplied by the ratio of the heat transfer area and the volume of a tube and divided by the heat capacity because in the APROS heat flux calculation the coefficient is multiplied by an enthalpy difference instead of a temperature difference. In the six-equation model the interfacial heat transfer between the saturated steam and the liquid, and the heat transfer between the wall and the liquid are calculated separately (Hänninen et Ylijoki, 2004). Since the Shah correlation was developed for a total condensation coefficient between the saturation temperature and the cold wall surface, it must be used in the form

$$K_{il,ne} = \frac{K_{il,sh}}{1 - \frac{K_{il,sh}}{K_{wl}}} \tag{3}$$

The Shah correlation was developed by analyzing test data from vertical, horizontal and inclined pipes with diameters between 7.4 - 40 mm, and mass flux and pressure ranging from 8.3 - 1600 kg/m²s and 0.07 - 9.8 MPa, respectively.

4.3.1.2 Chen correlation

The local condensation correlation for co-current annular film flow inside vertical tubes developed by Chen et al. (1987) is

$$Nu = \left[\left(0.31 \mathrm{Re}_l^{-1.32} + \frac{\mathrm{Re}_l^{2.4} \mathrm{Pr}_l^{3.9}}{2.37 \cdot 10^{14}} \right)^{1/3} + \frac{\mathrm{Pr}^{1.3} A}{771.6} (\mathrm{Re}_{l,t} - \mathrm{Re}_l)^{1.4} \mathrm{Re}_l^{0.4} k_l \right]^{1/2} \tag{4}$$

The coefficient A is defined as

$$A = \frac{0.252 \mu_l^{1.177} \mu_g^{0.156}}{D_H^2 g^{0.666} \rho_l^{0.553} \rho_g^{0.78}} \tag{5}$$

The heat transfer coefficient is calculated with the following equation

$$K_{il,ch} = \frac{4 Nu \cdot k_l}{D_H c_{pl} \left[\frac{\mu_l^2}{\rho_l^2 g} \right]^{0.33}} \tag{6}$$

The term $\mathrm{Re}_{l,t}$ in Eq. (4) is the film Reynolds number of the condensate film if total condensation of the vapor occurs. It is defined by Eq. (2). The superficial Reynolds number Re_l is

$$\mathrm{Re}_l = \frac{(1-\alpha)\rho_l \left|u_l\right| D_H}{\mu_l} \tag{7}$$

The first term on the right-hand side of Eq. (4) is the gravity-dominated part and the second term takes into account the interfacial shear stress. The equation is applicable for horizontal tubes if the gravity-dominated part is neglected. Annular film flow occurs if the vapor velocities are very high, and the shear forces are so high compared to gravitational forces that the tube orientation is unimportant (Chen et al., 1987). In the latest official APROS release 5.05.06 the following simplified modification of Eq. (4) is used and the gravity term is omitted from the code:

$$Nu = 0.036\,\mathrm{Pr}_l^{0.65} A^{0.5} (\mathrm{Re}_{l,t} - \mathrm{Re}_l)^{0.7}\, \mathrm{Re}_l^{0.2} \tag{8}$$

The Chen correlation was incorporated into APROS as an alternative for the Shah correlation for solving heat transfer in certain types of horizontal condenser tubes because the code assessment indicated it would perform better for flows of that type. This explains why the simplified horizontal flow correlation is used, instead of Eq. (4) applicable for all pipe orientations and a wide range of flow regimes.

Similarly to the Shah correlation, Chen correlation has been developed as a total heat transfer coefficient between the saturated fluid and the wall and it is used in the following form (Hänninen et Ylijoki, 2004):

$$K_{il,ne} = \frac{K_{il,ch}}{1 - \frac{K_{il,ch}}{K_{wl}}} \tag{9}$$

4.3.1.3 Droplet flow

In the droplet flow regime (flow with entrainment) the interfacial heat transfer coefficient is

$$K_{il,e} = \frac{6(1-\alpha)k_l}{\delta^2 c_{p,l}} \tag{10}$$

4.3.1.4 Stratified flow

The heat transfer coefficient for stratified flow according to Hänninen et Ylijoki (2004) is

$$K_{il,s} = \frac{k_l(4 + 0.07\,\mathrm{Re}_t^{0.8}\,\mathrm{Pr}_l^{0.4})}{\delta^2 c_{p,l}} \tag{11}$$

The increased turbulent mixing of due to interfacial shear is taken into account by using the turbulent Reynolds number

$$\begin{gathered} \mathrm{Re}_t = \frac{(1-\alpha)\rho_l u_t D_H}{\mu_l} \\ u_t = |u_l| + \sqrt{\frac{\rho_g}{\rho_l}}\,|u_g - u_l| \end{gathered} \tag{12}$$

The local effect of the liquid jet creates additional turbulence which enhances the heat transfer in the vicinity of the injection. This is taken into account by an extra term (injection cooling) in the liquid-to-interface heat transfer coefficient. The term is computed based on the injection jet velocity and temperature. The correlation for the stratified flow is based on the COSI experiment simulating the emergency core cooling system injections in cold legs and it is also used in the CATHARE code (Bestion, 1990).

4.3.2 Evaporation

Superheated liquid evaporates fast and reaches the saturation state within a very short time. The interfacial heat transfer correlation for superheated liquid ensures the saturation of liquid in all situations. The evaporation heat transfer coefficient is

$$K_{il} = \frac{1.2 \cdot 10^{-8} e^{4.5\alpha} \rho_l^2 u_l^2}{\mu_l \Pr_l}, \text{ if } h_l > h_{l,sat} \tag{13}$$

4.4 Thermal stratification model

Thermal stratification occurs in the upper part of the water section in the pressurizer when condensation at the steam-water interface forms a layer of warm water on the water surface. The heat is transferred by conduction only to the lower cooler water and there is no significant mixing of the hot and cool water. A sharp enthalpy drop is present across the interface. In standard models of APROS first order upwind discretization is utilized. The enthalpy and other quantities are averaged over the mesh nodes which results in unphysically smoothened temperature distributions when the fluid proceeds across several nodes. The problem is solved by using an alternative second order upwind discretization in which the first order upwind enthalpy is replaced with the enthalpy distribution defined by the enthalpies of three consecutive nodes (Vihavainen et al., 1999). To demonstrate this, the general enthalpy (temperature) profile and the movement of thermally stratified layer across a node boundary in 1D thermal hydraulic codes is given in Fig. 12. In APROS runs the second order upwind discretization is enabled in simulations in which the thermal stratification is examined.

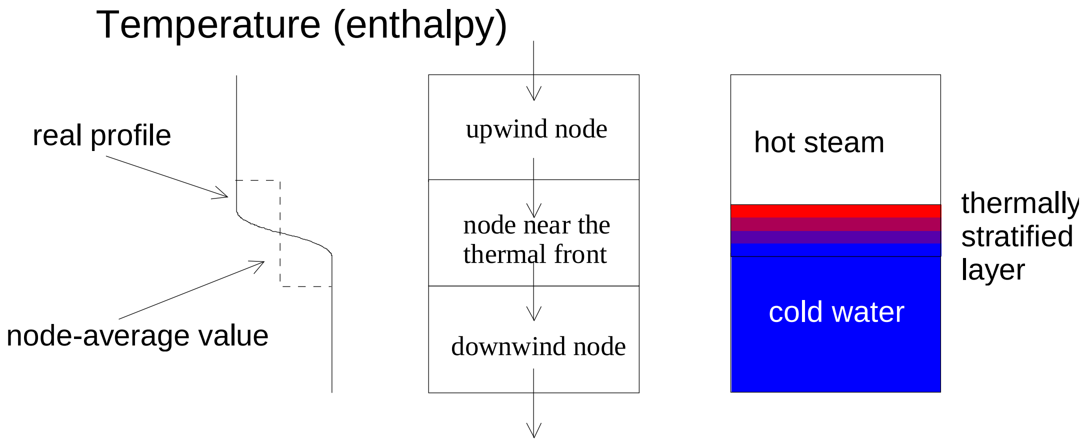

Figure 12. Principal view of thermally stratified layer across a node boundary (Vihavainen et al., 1999).

4.5 Test summary and simulation set-up

The APROS simulation runs conducted in this study are listed in Table 6 which shows which condensation correlations and nodalization schemes are used for each of the tests. The ATWS-10 and ATWS-20 tests are run using both condensation correlations available to evaluate their capability to solve the condensation in the pressurizer, after which the nodalization schemes of 3, 10, 30 and 100 nodes are tested using the ATWS-10 transient. The MIT pressurizer tests and the Neptunus tests as well as the Loviisa turbine transient are only calculated using the base model.

Table 6. APROS heat transfer correlation test cases.

TEST/MODEL	30-node base model	3-node model	10-node model	100-node model
ATWS-10	Shah/Chen	Shah/Chen	Shah/Chen	Shah/Chen
ATWS-11	Chen	-	-	Chen
ATWS-12	Chen	-	-	Chen
ATWS-13	Chen	-	-	Chen
ATWS-20	Shah/Chen	-	-	Chen
ATWS-21	Chen	-	-	Chen
MIT Insurge	Chen	-	-	-
MIT Outsurge	Chen	-	-	-
MIT Insurge to a hot tank	Chen	-	-	-
MIT Outsurge after insurge	Chen	-	-	-
MIT Empty tank insurge	Chen	-	-	-
Neptunus Y05	Chen	-	-	-
Loviisa transient	Shah/Chen	-	-	-

The thermal stratification in the upper part of the water section of the pressurizer and the enthalpy discretization method are investigated using the ATWS-10 test and following configurations

1) 30-node base model using the 1st order upwind discretization.
2) 30-node base model using the 2nd order upwind discretization.
3) 100-node model using the 1st order upwind discretization.
4) 100-node model using the 2nd order upwind discretization.

The maximum simulation timestep is 0.05 s and the maximum allowed relative mass error 0.0001. The minimum number of iterations in one timestep is 15 and maximum 30.

5 MODELING OF PRESSURIZER USING TRACE

The experiments discussed in Chapter 3 are calculated using the TRACE code pre-release V4.160 which was released on April 20, 2005, and comparisons between the results obtained by APROS and TRACE are made. Also in the TRACE simulations, special attention is paid to a detailed analysis of the PACTEL ATWS tests. The PACTEL ATWS simulations are included in VTT's contribution to the USNRC code assessment program CAMP. The TRACE simulations are performed using the base case nodalization. Unless mentioned otherwise, the simulation control options are the same as those used in APROS for the purpose of making the simulations comparable.

5.1 Nodalization schemes

In TRACE the "PRIZER" component represents pressurizer. Normally, the PRIZER models only the pressurizer reservoir, with the connecting surge line modeled by a PIPE or TEE component. The PRIZER component can be connected by its both junctions to other 1D hydraulic components. The PRIZER component provides special functions for steady-state calculations. These are simulation of a BREAK component to set the system pressure and to permit the fluid to swell or contact as a response to temperature changes, without requiring the user to model these boundary conditions separately, and calculation of the effects of gravity head and thermal non-equilibrium in the fluid to prevent small secondary transients at the beginning of a transient calculation. The PRIZER component provides a representation of heaters and sprays by manipulating the energy deposited in or extracted from the liquid in the tank. Similarly to APROS, the component creates a vertical stack of cells and calculates a collapsed liquid level (Spore et al, 2000). Note that, in the APROS vocabulary thermal hydraulic cells are referred as nodes but in TRACE "node" is used only for heat transfer nodes. Here, in connection to TRACE thermal hydraulic nodes are referred as cells but if APROS is discussed nodes can mean both thermal hydraulic and heat transfer nodes, depending on the context.

In the PRIZER component the operation of heaters and spray is controlled by a user-set control pressure and the heaters or spray is activated if the calculated pressure exceeds or is below the control pressure. In the case of spray the model is not fully mechanistic because a) the reduction in pressure relies on condensation of steam on the liquid pool surface as opposed to the spray itself, b) removing energy from the liquid results in artificially sub-cooling the entire water pool, c) there is net energy extraction from the PRIZER which does not actually occur and d) there are no mass flows associated with the spray in the PRIZER. For these reasons, the pressurizer spray is modeled by a separate boundary condition on top of the PRIZER component.

The tests described in the previous chapter have been repeated using the 30-cell base case model of the pressurizer. The surge line is modeled by three cells and the beginning of the line (representing the connection to the loop) there is a boundary condition component FILL. This boundary condition is used for both defining the insurge mass flow rate and outsurge rate. The mass flow table option of the FILL is used to determine the changes in the flow rate with respect to time throughout the simulation. (In APROS a similar table for the input of flow rates can be generated by using the Table function boundary condition in which the simulation time is given as the input and the liquid flow rate of the appropriate component as the output parameter. The Table function is used in the Neptunus model, Loviisa model and three of the MIT cases. In the other APROS models the boundary condition modifications are carried out by modifying the appropriate parameters for each module throughout the process. The commands for the modifications are read from individual .que -files for each test.) The graphical user interface SNAP is used for model construction and simulation control. A SNAP layout of the 30-cell model is shown in Fig. 13. The nodalization of the PRIZER, the surge line and the spray line are also visible in the figure.

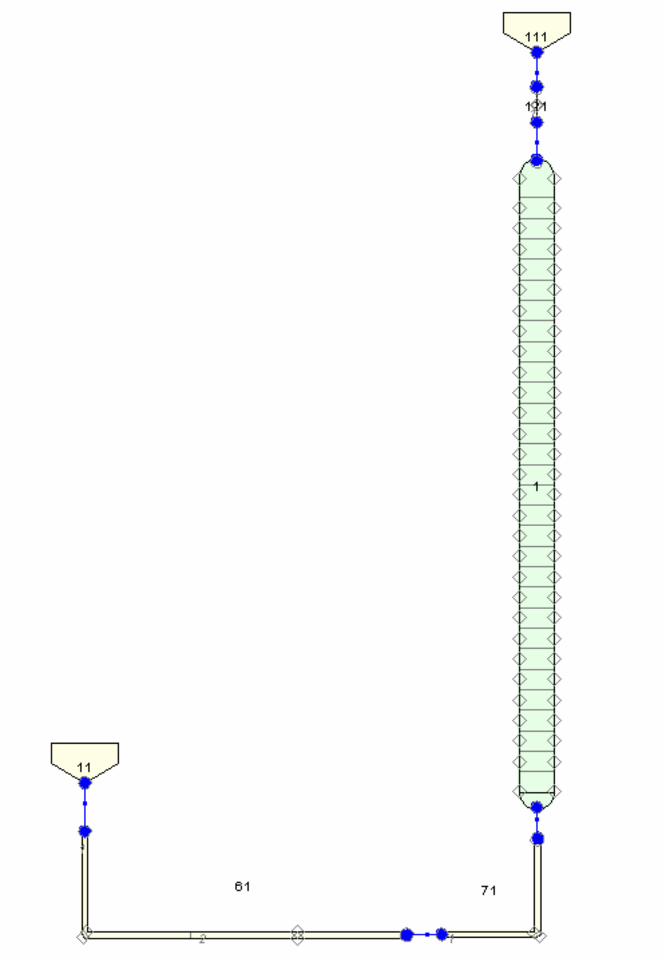

Figure 13. SNAP schematic of the PACTEL pressurizer including the FILL for surge line injection (11), the surge line and the FILL for spray (111). The width-length ratio of the PRIZER is 2:1.

5.2 Heat structures

The wall is divided into five radial heat transfer nodes and 30 axial nodes. The wall is simulated using a cylindrical heat structure component attached to the PRIZER. The axial conduction option is enabled as well as the liquid level tracking. A boundary condition for a constant heat transfer coefficient is defined at the outer surface of the heat structure which is in contact with the surroundings. A constant temperature of 25ºC is given to the surroundings and the heat transfer coefficient between the wall and the environment is obtained from the measurements at the test facilities. Next, a power component is created and connected to the heat structure to represent the pressurizer heater. The power component is controlled by a table in which the desired power as a function of time is defined. The length of the heated part of the pressurizer is defined in the Power Shape Table of the power component.

It is worth mentioning that the heat structure components of TRACE can utilize a fine mesh algorithm in the wall-to-fluid heat transfer solution which changes the coarse mesh conduction nodes to much smaller nodes capable of representing the sharp temperature gradient near the quench front in reflood conditions. Node rows may be added or removed from timestep to timestep, depending on the user-defined maximum temperature difference between node rows and the maximum number of node rows. In APROS the fine mesh renodalization is restricted to the core component.

5.3 Heat transfer models

TRACE calculates the heat transfer coefficients for interface-to-liquid, interface-to-gas, liquid-to-gas, wall-to-liquid and wall-to-gas heat transfer which are required by the closures of mass, momentum and energy equations to solve the heat transfer rates per unit volume. The interfacial heat transfer correlations are selected according to the flow regime. The flow regimes are bubbly slug flow, churn flow, annular-mist flow, transition to stratified flow, stratified flow, plug flow, reflood, bubbly flow, inverted annular flow and dispersed flow. For the wall heat transfer, TRACE considers eight regimes: forced convection to a single-phase liquid, nucleate boiling, transition boiling, film boiling, convection to a single-phase vapor, convection to a two-phase mixture, condensation and natural convection to a single-phase liquid (Spore et al., 2000).

5.3.1 Flow regime map

The simple flow regime map of TRACE is shown in Fig. 14. It is used for both vertical and horizontal flows.

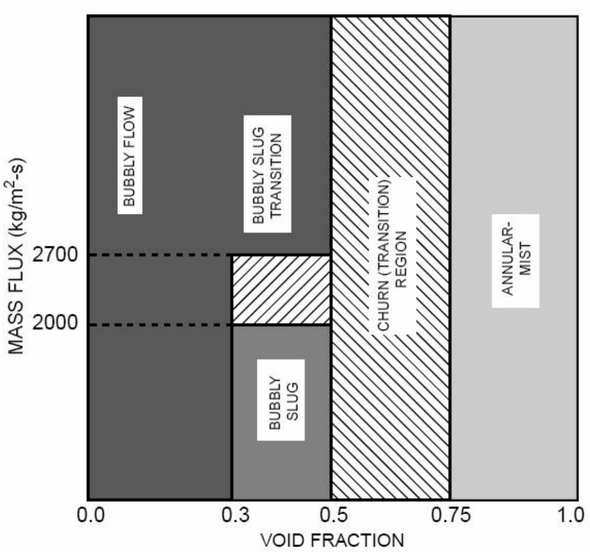

Figure 14. Basic flow regime map of TRACE for vertical and horizontal flows (Spore et al., 2000).

For modeling stratification for horizontal and vertical flows, a stratified flow regime is superimposed on the flow regime map. The horizontal stratification model is used only in the 3D VESSEL component. In case of liquid downflow, 1D components are also allowed to stratify regardless of their orientation. This type of stratification is of relevance to the current study. The transition criterion from bubbly slug to stratified flow is formulated as

$$V_{l,cr}(1-\alpha) \leq 0.2 \tag{14}$$

The transition criterion from annular-mist to stratified flow is

$$\alpha V_{g,cr} \le \left[\frac{0.2}{V_l (1-\alpha)} \right]^{0.435} \tag{15}$$

5.3.2 Condensation

5.3.2.1 Wall condensation

The requirement for condensation to occur are that the void fraction is greater than 0.05, the mass quality is greater than 0.71 and the wall temperature is lower than the combined gas and saturation temperature. The condensation correlation for laminar flow is based on the theoretical analysis of Nusselt. The coefficient according to Nusselt is

$$h_{gcond} = 0.9428 \left[\frac{\rho_l^2 g k_l^3 h_{fg}}{\mu_1 L (T_{sv} - T_w)} \right]^{0.25} \tag{16}$$

To account the ripples that develop on the liquid film as the Reynolds number increases, a modified version of the correlation is used:

$$h_2 = 0.003 \left[\frac{\rho_l^2 g k_l^3 L (T_{sv} - T_w)}{h_{fg} \mu_l^3} \right]^{0.5} \tag{17}$$

Equation (17) is an empirical correlation for film Reynolds numbers greater than 350. The turbulent natural convection heat transfer coefficient on a vertical plate is given by Eq. (18)

$$h_{gturb} = 0.023 \frac{k_g}{D_h} \mathrm{Re}_g^{0.8} \mathrm{Pr}_g^{0.3} \tag{18}$$

The liquid heat transfer coefficient is

$$h_{forc} = 0.023 \frac{k_1}{D_h} \left[\frac{\rho_l V (1.0 - \alpha) D_h}{\mu_l} \right]^{0.8} (\mathrm{Pr}_1)^{0.4} F \tag{19}$$

where F is the Chen factor defined by the following equations

$$F = 1.0 \text{ for } X_{TT}^{-1} \leq 0.10$$

$$F = 2.35 (X_{TT}^{-1} + 0.213)^{0.736} \text{ for } X_{TT}^{-1} > 0.01 \tag{20}$$

$$X_{TT}^{-1} = \left(\frac{x}{1-x} \right)^{0.9} \left(\frac{\rho_l}{\rho_g} \right)^{0.5} \left(\frac{\mu_g}{\mu_l} \right)^{0.1} \qquad \text{(Martinelli factor)}^{-1}$$

In addition,

$$h_{wl} = \max(h_{NC1}, h_{NC2}, h_{gforc}) \tag{21}$$

where

$$h_{NC1} = 0.59 \frac{k_l}{D_h} Gr_l^{0.25} \mathrm{Pr}_l^{0.25} \tag{22}$$

For vertical plates and cylinders when $1.0 \cdot 10^4 < Gr \cdot \mathrm{Pr} < 1.0 \cdot 10^9$ and

$$h_{NC2} = 0.10 \frac{k_l}{D_h} Gr_l^{0.3333} \mathrm{Pr}_l^{0.3333} \tag{23}$$

when $1.0 \cdot 10^9 < Gr \cdot \mathrm{Pr} < 1.0 \cdot 10^{13}$.

The assessment of the correlations has shown that Eq. (16) underestimates the film condensation approximately 20%, and a coefficient of 1.13 is recommended in place of

0.9428. The error increases if the correlation is used for Reynolds numbers exceeding 350. The empirical equation Eq. (17) has been found to predict the heat transfer coefficient for turbulent flow quite well. (Spore et al., 2000)

5.3.2.2 Annular-mist flow

The heat transfer correlations for annular-mist flow regime are chosen when the void fraction is between 0.75 and 0.999999 (Spore et al., 2000). The liquid forms a film on the pipe walls and flows as droplets in the gas core of the pipe. In TRACE the liquid film and droplets are superimposed within a single field. Prior to developing the heat transfer factors for annular-mist flow, the interfacial areas for droplets and the film must be calculated. The calculation of droplet area is based on the correlations for droplet diameter proposed by Kataoka et al., and Kitscha and Kocamustafaogullari (Spore et al, 2000). A detailed description and evaluation of the correlations is given in the TRAC-M Theory Manual by Spore et al. (2000). The liquid film area calculation is derived from purely geometric considerations with acknowledging the effect of surface waves forming on thin films.

The liquid side interfacial heat transfer coefficient for mist flow is calculated using the transient conduction solution in liquid droplets. The solution is approximated as follows:

$$Nu = \frac{\pi}{3} C_C \frac{1+T^*}{T^*} \tag{24}$$

where

$$Nu = \frac{h_{il} D_d}{k_l} \tag{25}$$

and T^* is the dimensionless instantaneous mixing cup temperature given by

$$T^{*} \approx \left[1 - e^{\left(-4\pi^{2} C_{C} \frac{k_{l} t}{\rho_{l} c_{p,l} D_{d}^{2}} \right)} \right]^{1/2} \tag{26}$$

In the code the correction factor C_C is assumed to be zero. To estimate the lifetime of the thermal boundary layer of a droplet a mean free path for the droplet population and the droplet velocity must be estimated. The droplet velocity is

$$V_d = V_g - V_r \tag{27}$$

where the relative velocity V_r is obtained from a force balance between gravity and drag

$$V_r = 2.462 \sqrt{g \frac{\rho_l - \rho_g}{\rho_g} \frac{D_d}{2}} \tag{28}$$

At each cell it is assumed that the average droplet is in the middle of its thermal lifetime t_d. Thus t in Eq. (26) is replaced by $t_d / 2$ where

$$t_d \approx \frac{D_H}{V_r} \tag{29}$$

The vapor side heat transfer coefficient is calculated using the Ryskin correlation.

$$Nu \approx 2 + \sqrt{V_{\max}^{*} Pe} \tag{30}$$

The Nusselt and Peclet numbers are

$$Nu = \frac{h_{ig} D_d}{k_g} \tag{31}$$

and

$$Pe = \frac{\rho_g c_{p,g} D_d V_r}{k_g} \tag{32}$$

The maximum dimensionless circulation velocity at the surface of the drop is

$$V_{\max}^{*} = \frac{1.5}{1 + \dfrac{2.8(1+2\lambda)(2+3\kappa)}{(2+3\lambda)\sqrt{\mathrm{Re}_g}}} \tag{33}$$

Where the Reynolds number is

$$\mathrm{Re}_g = \frac{\rho_g D_d V_r}{\mu_g} \tag{34}$$

and

$$\lambda = \sqrt{\frac{\rho_l \mu_l}{\rho_g \mu_g}} \tag{35}$$

and

$$\kappa = \frac{\mu_l}{\mu_g} \tag{36}$$

Next, the droplet model is combined with the liquid film heat transfer to obtain the heat transfer coefficients for annular-mist flow. Both the liquid and vapor side coefficients are calculated using a Stanton number correlation originally developed by Bankoff (Spore et al, 2000):

$$St = 0.0045\left(\frac{\rho_g V_g \mu_l}{\rho_l V_l \mu_g}\right)^{1/3} \tag{37}$$

In the code the Stanton number is defined as

$$St = \frac{h_{i,l}}{\rho_l c_{p,l} V_l} \tag{38}$$

to calculate the liquid side heat transfer,

$$St = \frac{h_{i,g}}{\rho_g c_{p,g} \left| V_g - V_l \right|} \tag{39}$$

to calculate the heat transfer between vapor and interface, or

$$St = \frac{h_{gl}}{\rho_a c_{p,a} \left| V_g - V_l \right|} \tag{40}$$

to calculate the heat transfer between vapor and liquid. The heat transfer factors are obtained by multiplying each heat transfer coefficient by the interfacial area. Generally, the correlations for a discrete phase, such as drops in annular-mist flows, exhibit a transient heat transfer characteristic with a small time constant. The averaging of the transient behavior is the main problem limiting the accuracy of the correlations for droplet flows.

5.3.2.3 Stratified flow

The weighting factor W_{st} is used to superimpose the stratified flow on the flow regime map given in Section 5.3.1. A weighting factor of unity indicates full stratification, and a weighting factor of zero means that the criteria for stratification are not met. During condensation in the pressurizer and in the accumulator the weighting factor is set to 1 to represent vertically stratified flow. The interfacial area for vertically stratified flow in the pressurizer is equal to the average cross-sectional area of the cell:

$$A_l = \frac{V_{cell}}{L_{cell}} \tag{41}$$

The liquid side heat transfer coefficient is calculated using a constant Stanton number criterion

$$St = \frac{h_{i,l}}{\rho_l c_{p,l} V_l} = 0.0073 \tag{42}$$

The magnitude of the Stanton number is originally suggested by Linehan et al. (1972) who obtained it from experimental data related to steam condensation on sub-cooled water (Spore et al., 2000). They used a horizontal rectangular channel which was 15 cm wide and 1.7 cm high. The steam Reynolds numbers ranged from 14000 to 17500 and the liquid Reynolds number corresponding to injection flow rate was between 250 and 1800. The injected liquid sub-cooling ranged between 7ºC and 80ºC. In the case of pressurizer, no modification is made to the vapor side heat transfer coefficient due to stratification. (Spore et al., 2000)

5.3.3 Evaporation

The film boiling heat transfer regime incorporates several correlations to fully describe film boiling. Film boiling occurs when the wall temperature exceeds the minimum stable film boiling temperature. The heat transfer coefficients for wall-to-liquid and wall-to-vapor are treated separately. Wall-to-liquid heat transfer is the sum of two components: radiation and near-wall liquid effects (Spore et al., 2000).

The liquid heat transfer coefficient is

$$h_{wl} = (h_r + h_{fBB}) \cdot \left[\frac{(T_w - T_{sat})}{(T_w - T_l)} \right] \tag{43}$$

where the radiation component is

$$h_r = \alpha_1 \sigma_r \varepsilon \frac{(T_w^4 - T_{sat}^4)}{(T_w - T_{sat})} \tag{44}$$

In Eq. (44), α_1 = 0.9999 -α, σ_r is the Stefan-Boltzmann constant and ε is the wall emissivity which is assumed to be 1.0. The film boiling component is calculated using the modified Bromley correlation:

$$h_{fBB} = 0.62 \left[\frac{(\sigma_g k_g^3 (\sigma_l - \sigma_g) g h_{\lg}^{'})}{\mu_g (T_w - T_{sat}) \lambda} \right]^{0.25} \tag{45}$$

where λ is the characteristic length given by

$$\lambda = 2\pi \left(\frac{\sigma}{g(\sigma_l - \sigma_g)} \right)^{1/2} \tag{46}$$

and $h_{\lg}^{'}$ is a modified latent heat to account the superheated vapor such that

$$h_{\lg}^{'} = h_{\lg} + 0.5 + c_{pg} (T_g - T_{sat}) \tag{47}$$

The heat transfer coefficient between wall and vapor is calculated using the Dougall-Rohsenow or the turbulent, natural convection correlation, depending on which one gives the greater value. The Dougall-Rohsenow correlation is

$$h_{dr} = 0.023 \mathrm{Re}_{TP}^{0.8} \mathrm{Pr}_g^{0.4} \frac{k_g}{D_H} \tag{48}$$

where

$$\mathrm{Pr}_g = \left(\frac{c_p \mu}{k} \right)_g \tag{49}$$

and

$$\mathrm{Re}_{TP} = \frac{\rho_g \left[\left| V_g \right| \alpha + \left| V_l \right| (1-\alpha) \right] D_H}{\mu_g} \tag{50}$$

The turbulent natural convection correlation is

$$h_{NC} = 0.13 k_g \left(\frac{\rho_g^2 g_c \left| T_w - T_g \right|}{\mu_g^2 T_g} \right)^{0.3333} \mathrm{Pr}_g^{0.3333} \tag{51}$$

The Bromley correlation is a pool-boiling type of a correlation which describes the inverted annular flow film boiling without accounting the effect of mass flow rate on the magnitude of the heat transfer coefficient. The Dougall-Rohsenow correlation was developed assuming that the thermal resistance exists at the liquid-vapor interface and is the result of a laminar zone, a transition zone and a turbulent zone. As the film Reynolds number increased the zones of resistance were gradually removed until none existed in dispersed flow. There are still significant discrepancies between the experimental data and the film boiling correlations in TRACE and also among the different correlations, and further investigations for possible improvements of the model were suggested by Spore et al. (2000).

6 RESULTS AND COMPARISON

6.1 ATWS-10 – ATWS-13

In sections 6.1.1 to 6.1.3 the insurge simulation results of the following modeling cases are analyzed using APROS: the base model using the Shah and the Chen condensation correlations, 3-, 10- and 100-node models using the Shah and Chen condensation correlations and the base model and the 100-node model using first order and second order discretization. In section 6.1.4 the TRACE simulations are included into the analysis and comparisons between simulations by the two codes are made.

6.1.1 Base model

In this section, 30-node pressurizer results are compared to the experimental results of the ATWS insurge followed by outsurge tests. The general parameters such as wall and node temperatures and heat fluxes are observed in detail for the purpose of gaining an in-depth understanding of the phenomena determining the pressure behavior. First, the wall condensation and evaporation which are the dominating heat transfer mechanisms in insurge and outsurge transients were simulated using both correlations available in APROS to test the ability of the code to simulate insurge and outsurge transients where the flow velocities of both the liquid and the steam phase are quite small. The test case was ATWS-10.

6.1.1.1 Shah and Chen correlations

It was observed that calculating the transient using the Shah correlation the pressure reaches approximately 11.3 MPa at 220 s when the measured maximum pressure at the test facility was only 7.8 MPa. As can be seen in Fig. 15, the Chen correlation used in the current APROS release 5.05.06 also predicts the pressure increase to be much more rapid than experimentally shown. Similar results are obtained from simulations of the older MIT insurge tests.

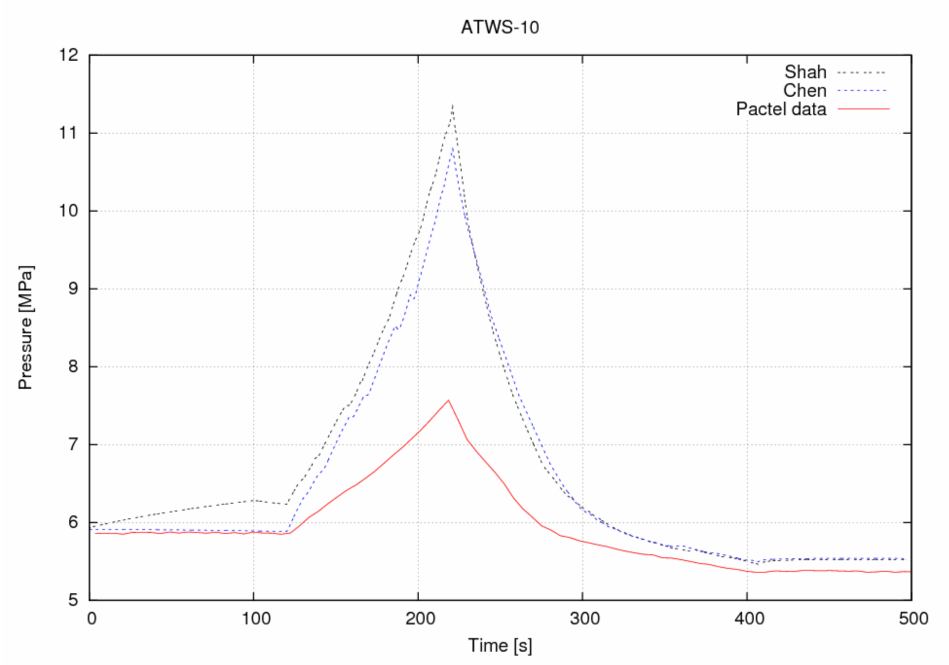

Figure 15. Measured pressure, calculated pressure using the Shah correlation and calculated pressure using the Chen correlation as a function of time (APROS 5.05).

The Shah correlation was developed and assessed for parameter ranges presented in section 4.3.1.1. The correlation has been tested for the turbulent regime for film Reynolds numbers from 100 to 63 000 and it is recommended for Reynolds numbers higher than 350 (Shah, 1979). In the experiments the average liquid Reynolds number, given by Eq. (2), in the steam section is almost all the time during the insurge below 350, except in the steam region just above the water level. The assessment has shown that the Shah correlation is not suitable for predicting the film condensation for clearly laminar flows. Increasing the node number to 100 nodes does not give better results either, as will be shown in section 6.1.2.

The cause for the error in the results obtained by the Chen correlation is more interesting. The original Chen correlation was established to incorporate the effects of interfacial shear, interfacial waviness and turbulent transport, and combine the gravity-dominated and shear-dominated film condensation (Chen et al., 1987). Chen et al. (1987) tested the correlation against experimental data from a wide range of flow regimes and concluded that the correlation is capable of predicting the heat transfer coefficient for most film condensation applications except high vapor flow rates where both interfacial shear and waviness are important. Recalling from Chapter 4, the correlation for co-current annular film condensation inside horizontal tubes which neglects gravitational forces, Equation (8), is used in APROS. In a pressurizer, the liquid and vapor mass flows in the nodes of the steam section are very small and the behavior of the film on the pressurizer wall is definitely dominated by gravitational forces, instead of shear stress. The vapor flows caused by the piston movement of the rising water surface and natural convection are relatively very low. The correlation for high-velocity shear-dominated tube flows is not applicable to vertical laminar flows. The APROS release 5.05.06 is not capable of calculating the film condensation correctly in the insurge transients. After discovering this, a test version of APROS was compiled, in which the full Chen correlation for annular film flow in vertical tubes is used. Otherwise, the APROS test version is identical to the official release. A comparison between the pressure calculation of the two Chen correlations and the PACTEL test results is presented in Fig. 16.

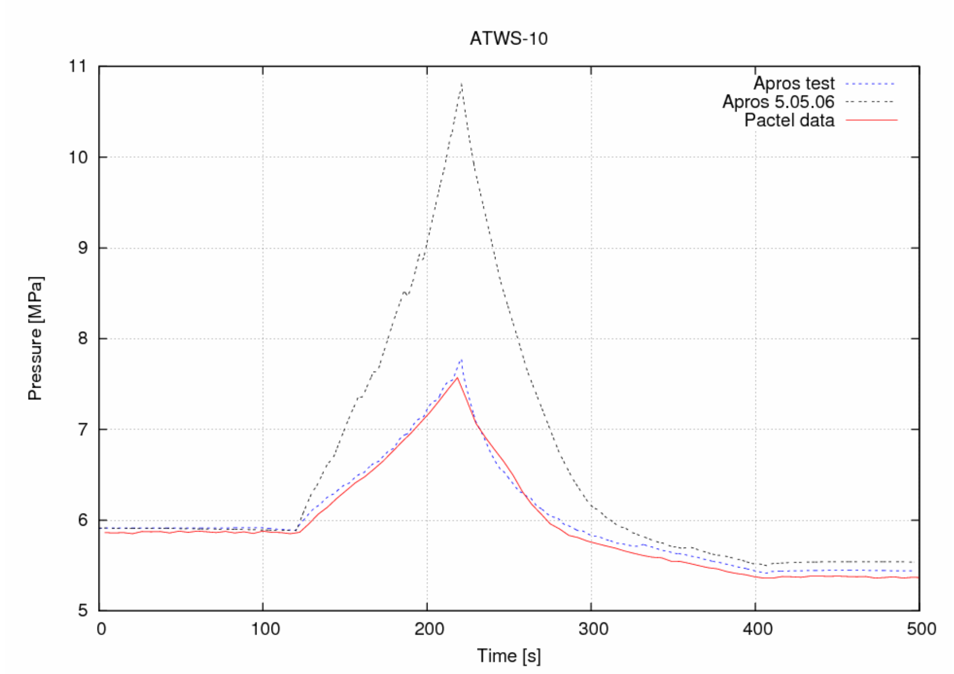

Figure 16. Pressurizer pressure vs. time during ATWS-10 test in the PACTEL test, APROS 5.05.06 and APROS test version (Chen correlation).

In this case, the test version simulation shows a good correlation with the experimental results. The deviation from the test data is approximately 0.2 MPa. The steady-state pressure after the transient is somewhat lower than the initial pressure due to environmental heat losses. The error for the PACTEL pressure measurement for the ATWS-10 test as well as for the other ATWS tests is less than ±0.094 MPa according to the error estimate routines which were run during the tests.

The average heat transfer from wall to thermal hydraulic node in the upper part of the container, between height of 6.5 m and the top, is shown in Fig. 17 for both code versions. This region is above the water level throughout the simulation and the heat transfer consists of condensation at the walls. The heat flow computed by the horizontal Chen correlation amounts to roughly half of the heat transfer by the general correlation. A comparison of cumulated mass transfers between the correlations is demonstrated in Fig. 18, negative value indicates condensation, positive evaporation. As soon as the insurge starts, condensation starts in the steam region. The total amount of steam condensed at the beginning of the draining (t = 220 s) is 1.25 kg which corresponds the value calculated by Riikonen (1998) for ATWS-10 test. Condensation at the phase interface (pool surface) is a small contribution to the total mass transfer in the system but it can be considered negligible. The other experiments in this study, except ATWS-20 and ATWS-21 and some of the cases for nodalization comparison in the next section, were simulated using the test version of APROS, since it is able to calculate the film condensation with fundamentally better accuracy. A comparison of the steam and saturation temperatures (magnitude of steam superheat) during ATWS-10 – 13 tests for both experimental and simulated data obtained using the full Chen correlation is presented in Appendix 1. The test-specific maximum error for the fluid temperature measurements reported for the ATWS-10 – 13 tests is ± 3.8ºC. It is likely that the actual error in the temperatures is smaller than what is reported but this indicates that an inaccuracy of a few centigrade exists also in the measured data.

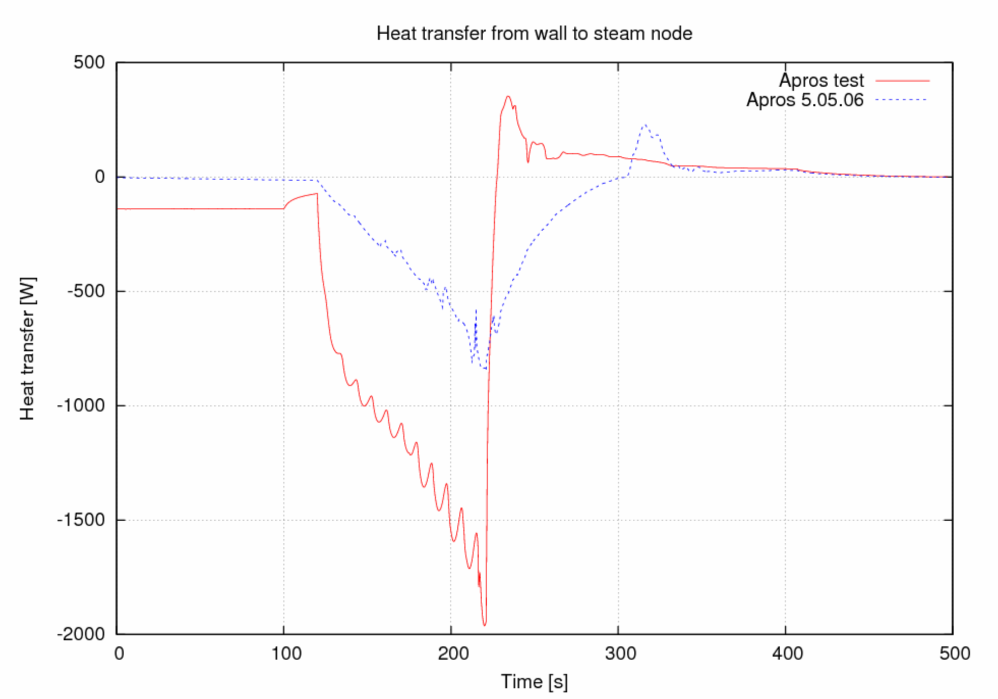

Figure 17. Average heat transfer in nodes 24 to 30 in the ATWS-10 test calculated by APROS 5.05.06 and the test version.

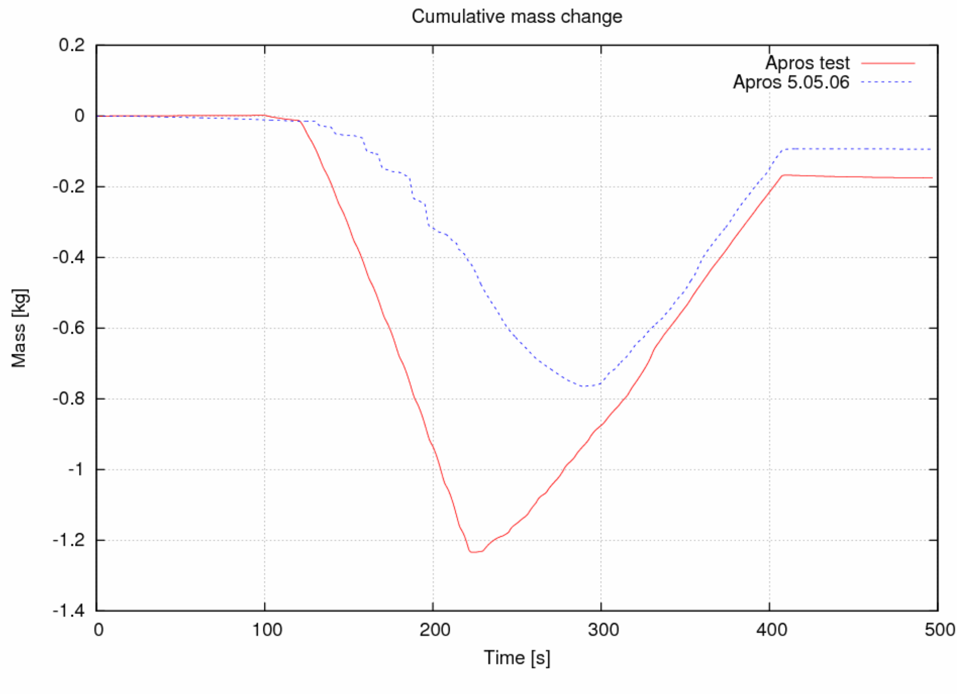

Figure 18. Condensed mass in ATWS-10 test simulated by APROS 5.05.06 and APROS test.

6.1.2 Nodalization

The pressure results for ATWS-10 to ATWS-13 are presented in Fig. 19, 20, 21 and 22 which are obtained using the base model and the 100-node model. Examination of the base model shows that the ATWS-10 and ATWS-11 simulations correspond the experimental results satisfactorily but in the ATWS-12 and ATWS-13 runs, in which the insurge rate is the smallest, a deviation of 0.5 MPa is observed. As the rising water level crosses a node boundary from one node full of water to a node full of steam a “step” is visible in the pressure curve. This indicates that it would be reasonable to improve the accuracy further by using a denser mesh. In the 100-node model the height of a single node is 8.8 cm and the node boundaries are indistinguishable from the figures. The 100-node model predicts that the pressure rises approximately to 8.05 MPa during the ATWS-10 insurge which is 0.35 MPa higher than the base model prediction. The pressure is slightly higher with all four transients.

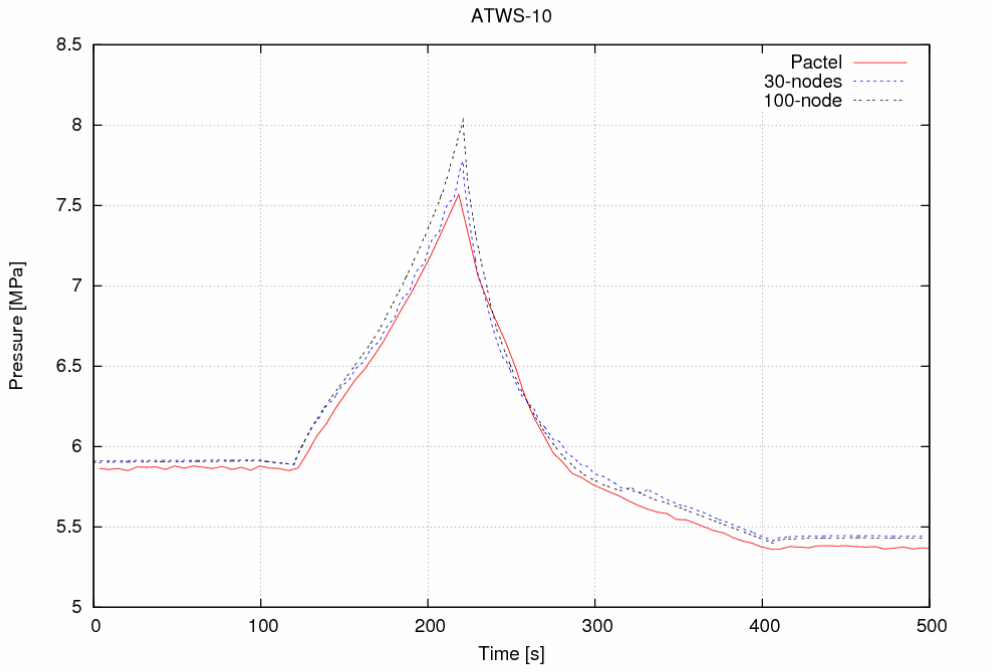

Figure 19. Pressure behavior during ATWS-10 transient.

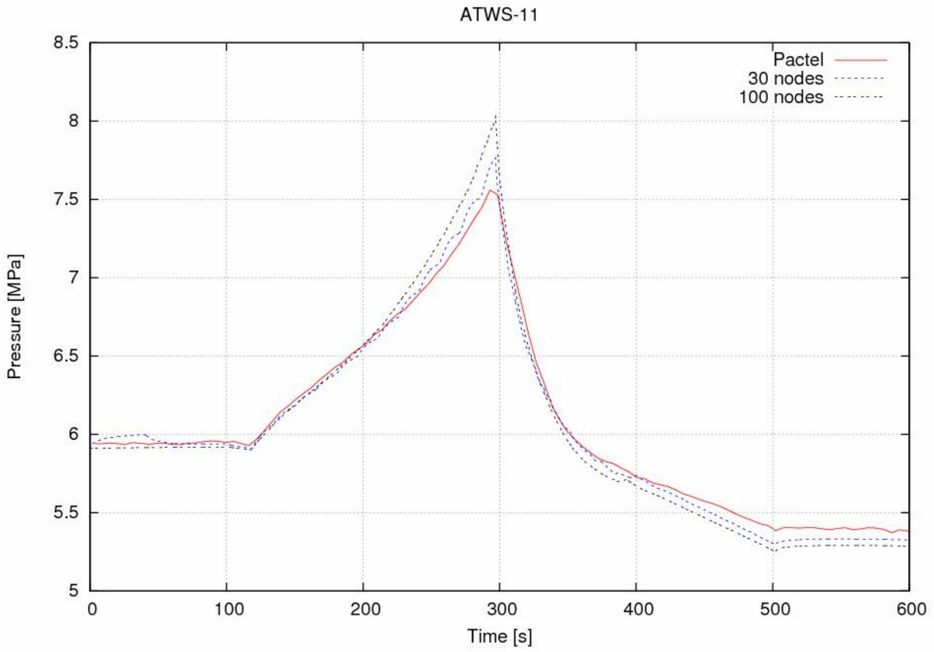

Figure 20. Pressure behavior during ATWS-11 transient.

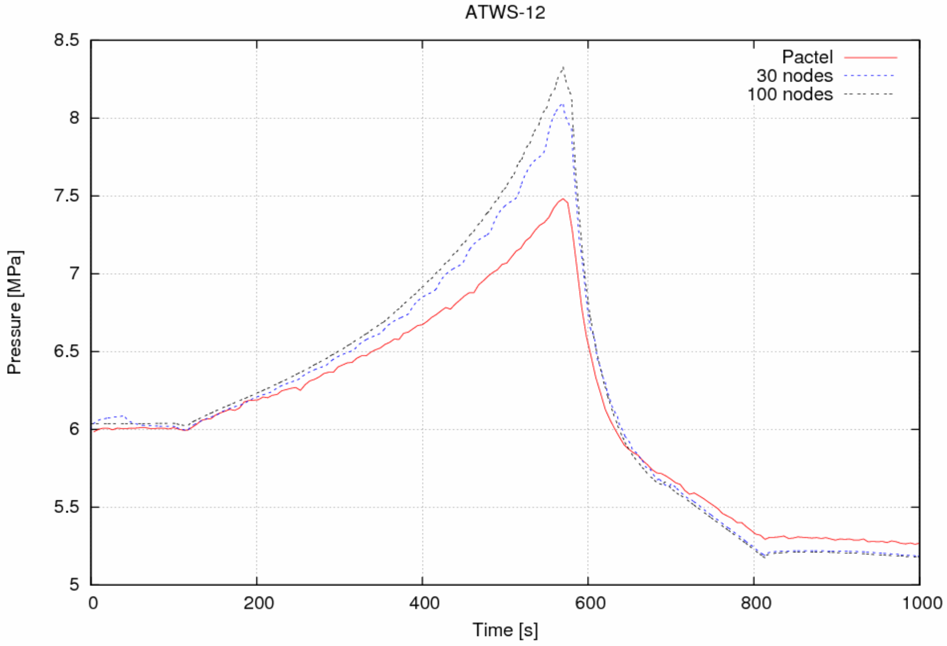

Figure 21. Pressure behavior during ATWS-12 transient.

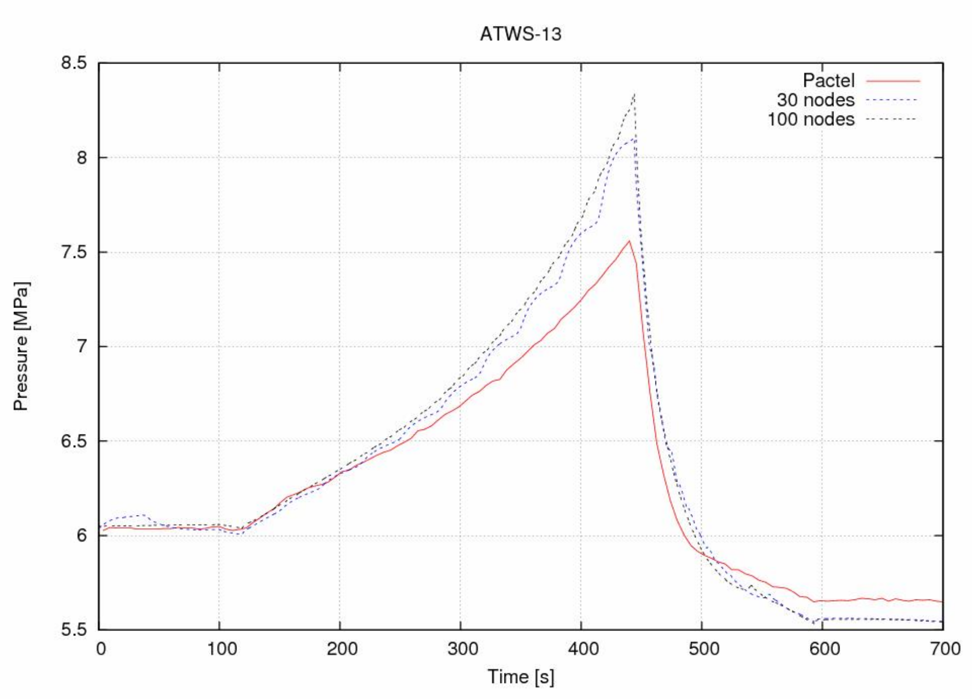

Figure 22. Pressure behavior during ATWS-13 transient.

In order to further investigate which nodalization scheme is optimal for a single channel pressurizer, the ATWS-10 test was simulated using 3-, 10-, 30- and 100-node pressurizer. The comparisons are shown in Figs. 23 and 24. The simulation was performed using both Shah and Chen wall condensation correlations. It appears that the Shah correlation produces the most accurate results for the 3-node pressurizer whereas the 10-node and 30-node cases show a remarkable deviation as expected. In fact, both the condensation correlation and the 3-node coarse mesh configuration are not suitable for the simulation and the relatively good result is merely a coincidence. In the case of three very large nodes, each of the nodes contains water at a certain temperature computed in the middle of the node. Thermal stratification and formation of a layer of saturated water in the upper part of the water volume due to steam condensation is not modeled. The condensation is computed using the average temperature of the large, unrealistically cool node which will result in an exaggerated interfacial condensation rate at the water surface which compensates the error in the wall condensation calculation. The analyst should keep in mind that erroneous simulation configurations may produce seemingly reasonable results, and care should be taken to avoid misinterpretations. Thermal stratification and its effect on the pressure behavior in the water volume are analyzed in detail in the next section.

Using the Chen correlation the 3-node model computes the pressure to be lower than measured pressure, also presumably because of the reduced condensation rate. Using this model, an unphysical drop is observed when the water level crosses the boundary between the second and the third node. The 10-node pressure trend is closer to that of the denser mesh models but the disturbance caused by the relatively large nodes is quite significant. The gradual smoothening of the pressure curve with improved nodalization is clearly visible in Figs. 23 and 24.

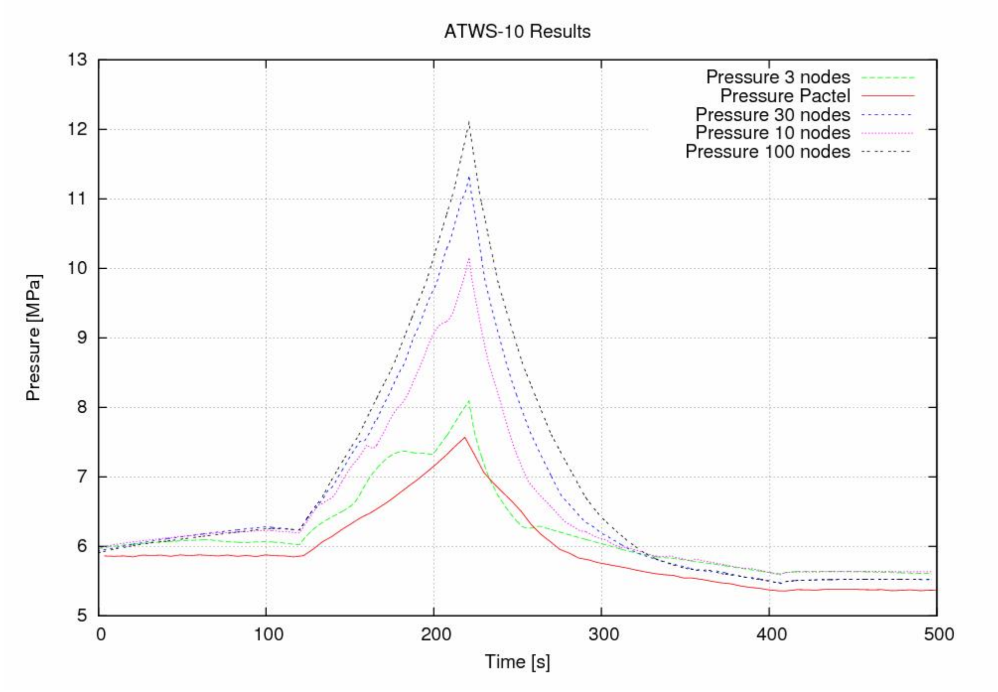

Figure 23. Pressure curve obtained by different nodalization schemes and the Shah condensation correlation.

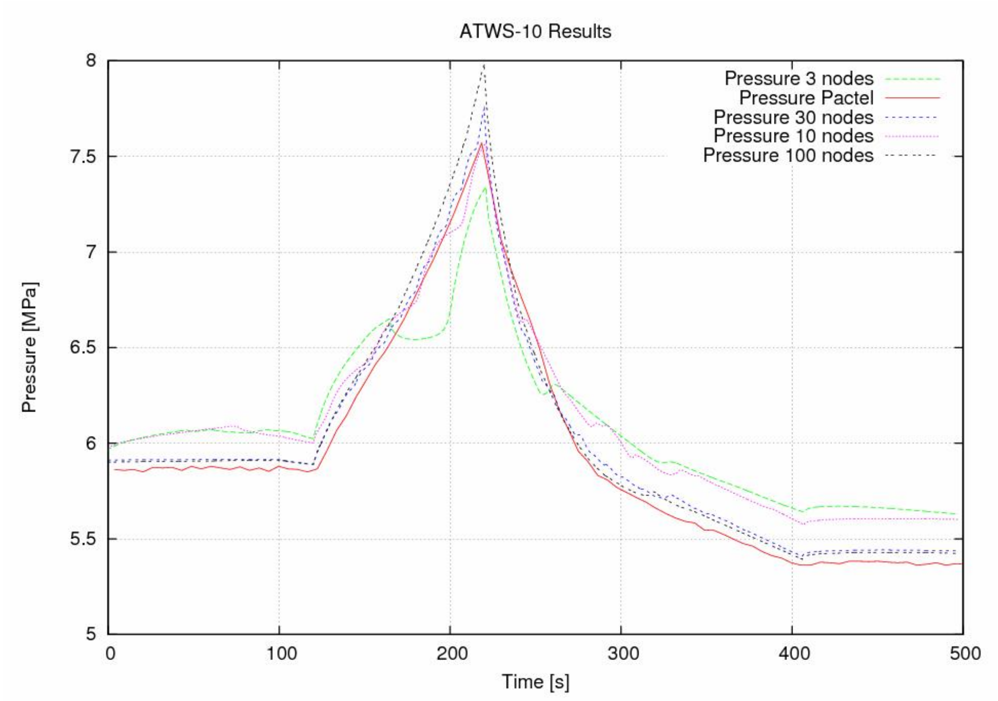

Figure 24. Pressure curve obtained by different nodalization schemes and the Chen condensation correlation.

6.1.3 Thermal stratification

Thermal stratification near the pool surface is investigated using the 100-node “pipe” pressurizer which is expected to produce the most accurate results, which are then compared to the results obtained by the base model. The second order upwind discretization is utilized and a comparison between the temperature predictions of the two discretization schemes is made. The test case used in the thermal stratification study is ATWS-10. The overall effect of the second order discretization method on the pressure calculation of the whole transient is seen in Figs. 25 and 26 where comparisons of the simulations utilizing second order and first order upwind schemes are presented. It was observed that using the second order upwind option maximum pressure at the end of the insurge is roughly 0.2 MPa higher than that of the first order calculation case for both of the nodalizations.

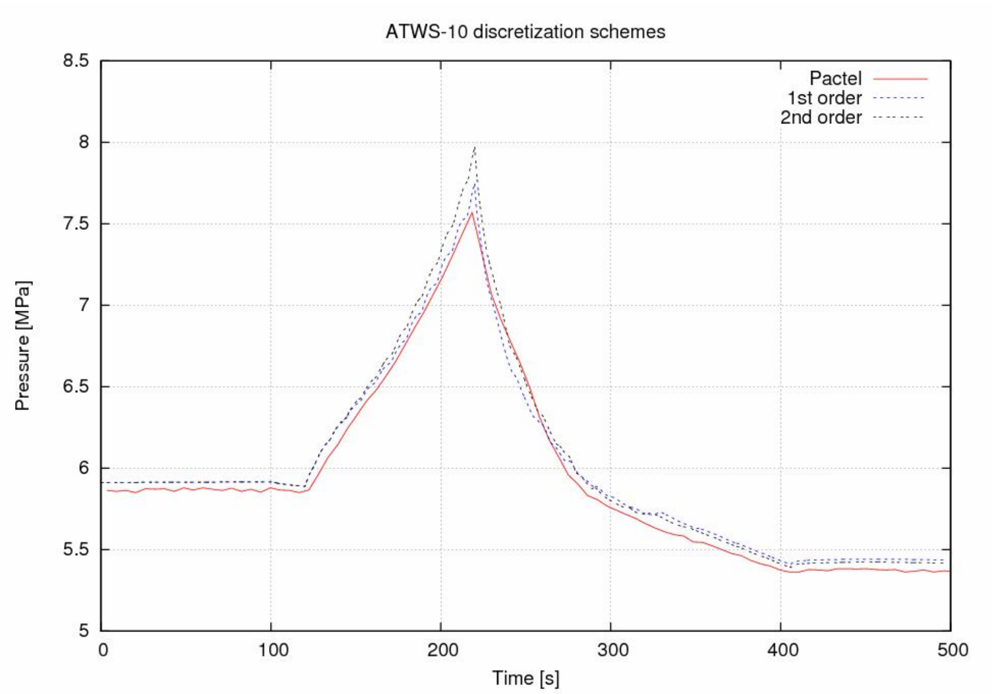

Figure 25. Base model pressure behavior calculated using 1st and 2nd order discretization.

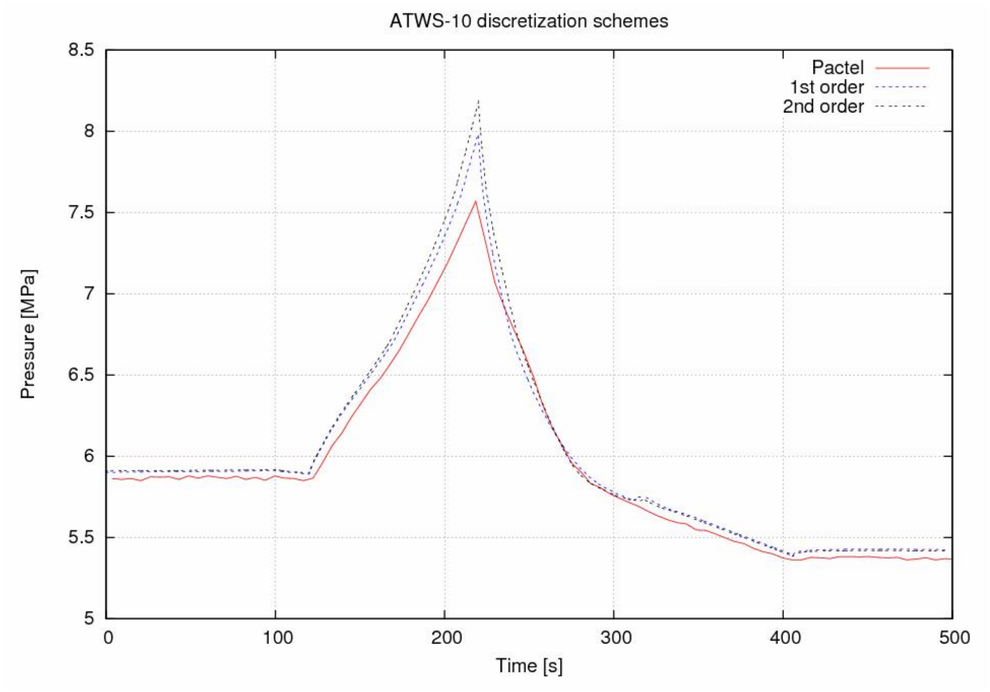

Figure 26. 100-node model pressure behavior calculated using 1st and 2nd order discretization.

Figures 27, 28 and 29 show the axial liquid temperature profile at simulation times *t*=140 s, *t*=180 s and *t*=220 s, during the insurge phase of the ATWS-10 transient. The x-axis value is the node number along the pressurizer height starting from the bottom of the pressurizer. The water level is located in the node immediately on top of the sharp temperature increase which is seen in the figures. In the nodes above the water a liquid film is present at the pressurizer wall and the liquid temperature is defined to be the temperature of the inner wall. If the film is evaporated and the node contains only steam APROS sets the liquid temperature to be same as the node steam temperature. In the figures, the leveling of the temperature curves in the upper nodes indicates that these nodes are filled with steam, or a thin liquid film exists at the wall, and the liquid temperature is the saturation temperature.

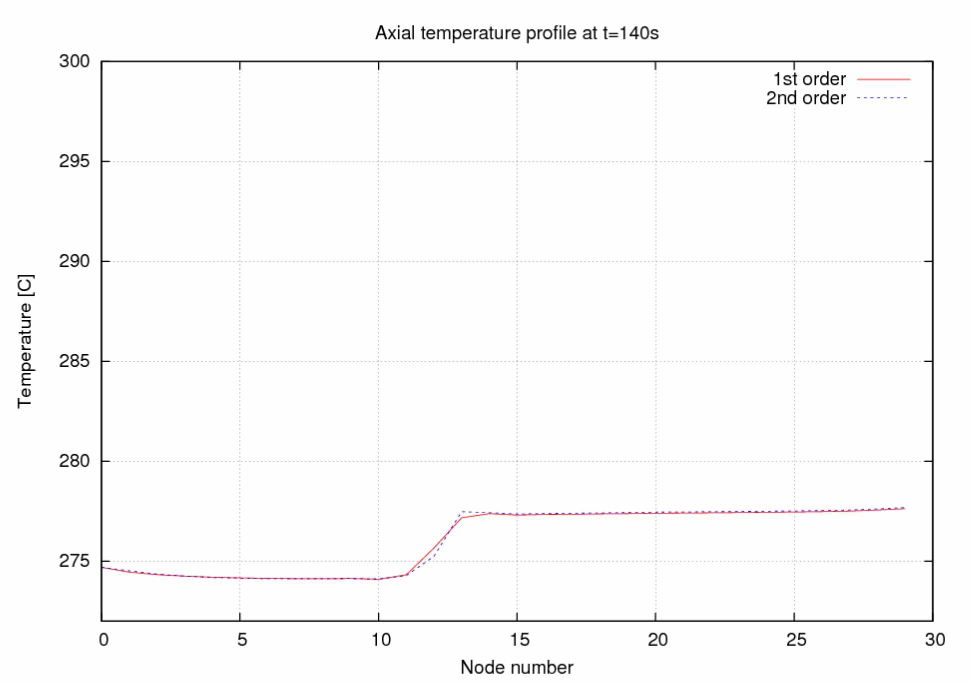

Figure 27. Liquid temperature vs. node number (1 denotes bottom of the tank) at *t*=140s.

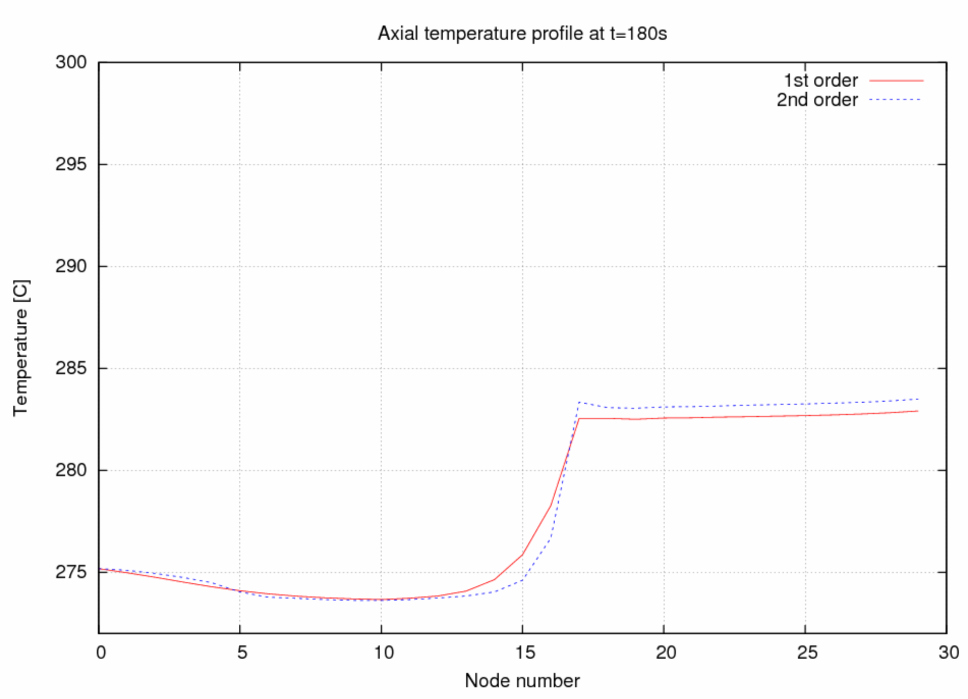

Figure 28. Liquid temperature vs. node number (1 denotes bottom of the tank) at *t*=180s.

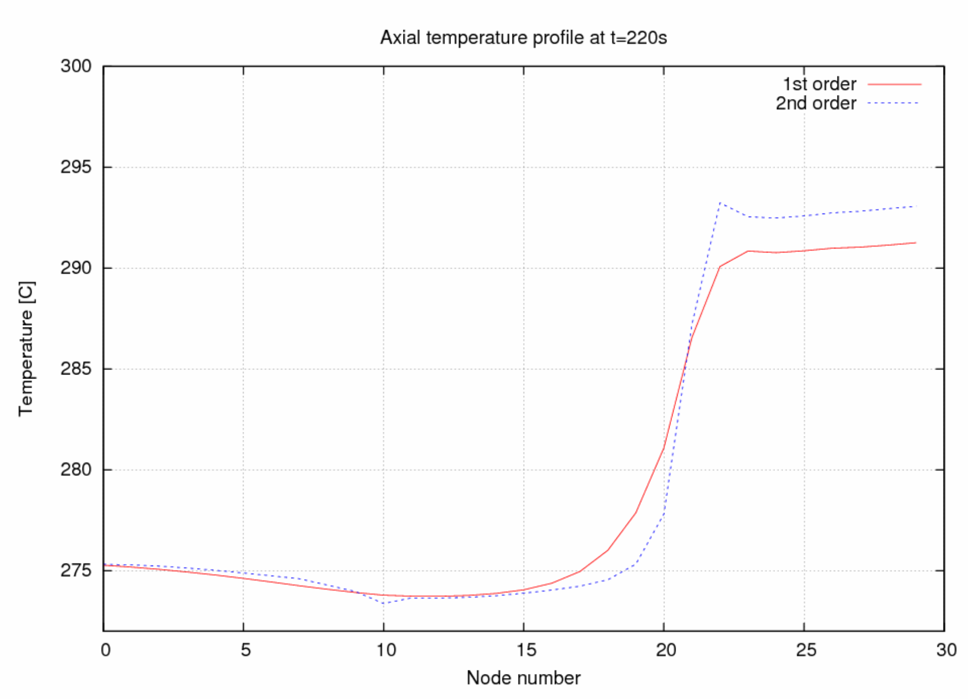

Figure 29. Liquid temperature vs. node number (1 denotes bottom of the tank) at *t*=220s.

The gradual increase of the pressurizer level during the insurge is seen in Figs. 27, 28 and 29 as the temperature jump proceeds from node to node. The temperature increase becomes greater as the insurge proceeds since the steam volume temperature rises corresponding to the pressure increase in the system. The difference between the first and second order upwind scheme calculations becomes more significant as the temperature difference of adjacent nodes increases. A similar behavior is shown in the temperature profiles of the 100-node model which are presented in Figs. 30, 31 and 32.

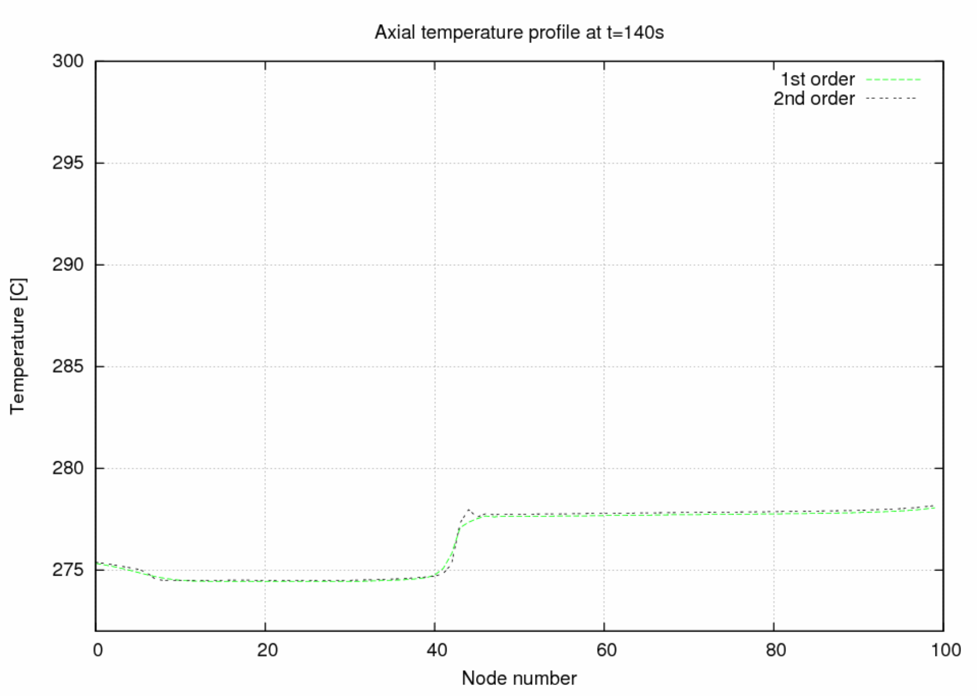

Figure 30. Liquid temperature vs. node number (1 denotes bottom of the tank) at t=140s.

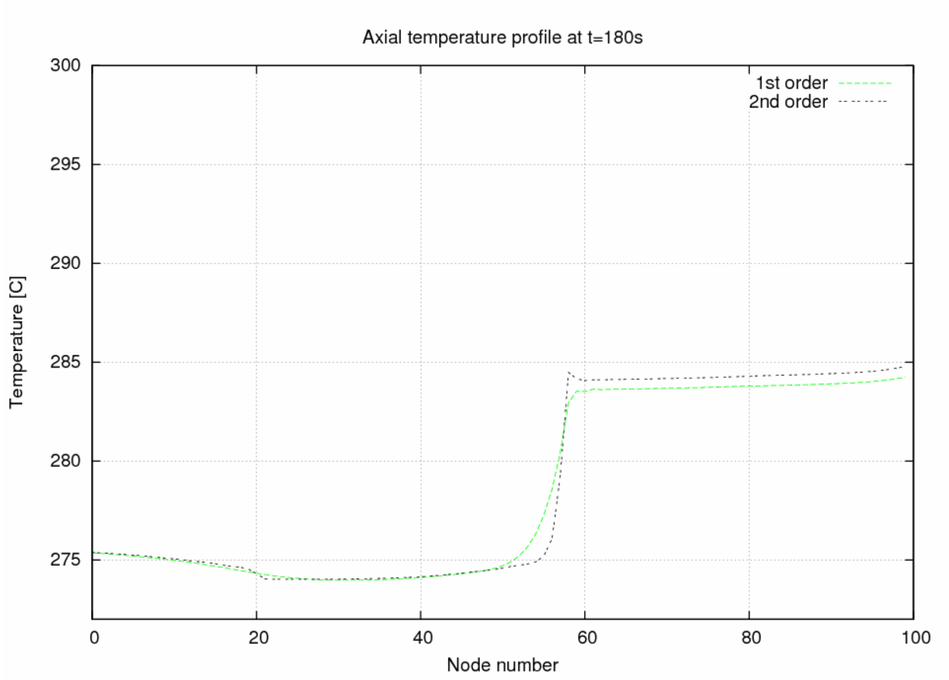

Figure 31. Liquid temperature vs. node number (1 denotes bottom of the tank) at *t*=180s.

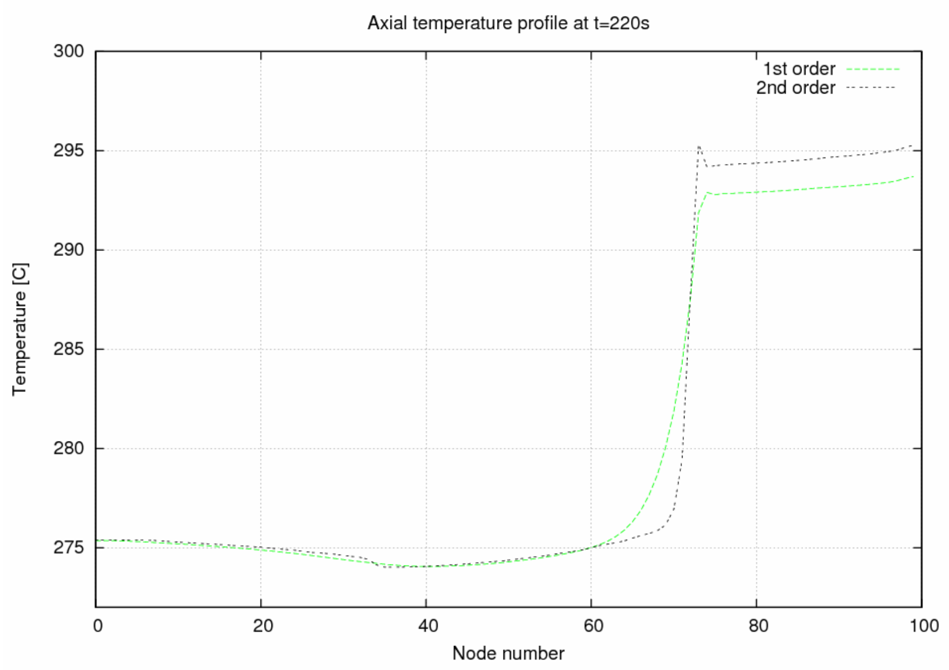

Figure 32. Liquid temperature vs. node number (1 denotes bottom of the tank) at *t*=220s.

Finally, a comparison between the models at the end of the compression phase, presented in Fig. 33, shows that the base model with first order discretization gives the most smoothened temperature profile at the phase interface. The temperature profiles obtained by using the base model with second order discretization enabled and the 100-node model with first order discretization are very similar. Thus, a renodalization to a dense 100-node mesh from the 30-node mesh accounts for a similar improvement to the accuracy of the enthalpy solution as changing the discretization method from first order to second order upwind. The sharpest and most realistic profile is provided by the 100-node mesh using the second order upwind scheme. The results are consistent with the fact that the smoothening of the temperature profiles can be reduced by a denser mesh. A close-up of the profiles of Fig. 33 is shown in Fig. 34. This figure represents the portion of the pressurizer between 5 m and 6.6 m, which is the topmost part of the water volume in the tank. Nodes from number 18 to 23 are located within this range in the base model, and nodes from 57 to 75 in the 100-node model. The temperature distribution of the first order base case shows that the temperature rises across the nodes very evenly. The second order 100-node case is capable of simulating the sharper profile which is formed as the condensing steam forms a layer of warm water on the interface. Below this layer the heat is transferred only by conduction in the water and temperature profile in the water volume nodes below the interface node should remain nearly uniform. The sharp temperature rise is located between nodes 72 and 74.

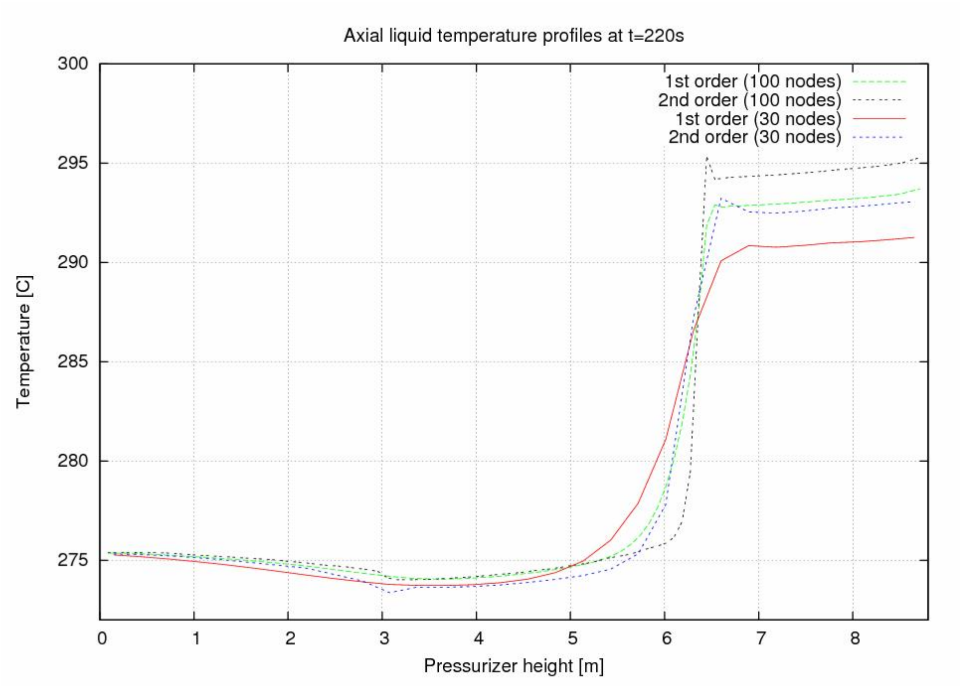

Figure 33. Liquid temperature profiles of 30-node and 100-node models at *t*=220s using both discretization methods. X-axis value is the pressurizer height from the bottom.

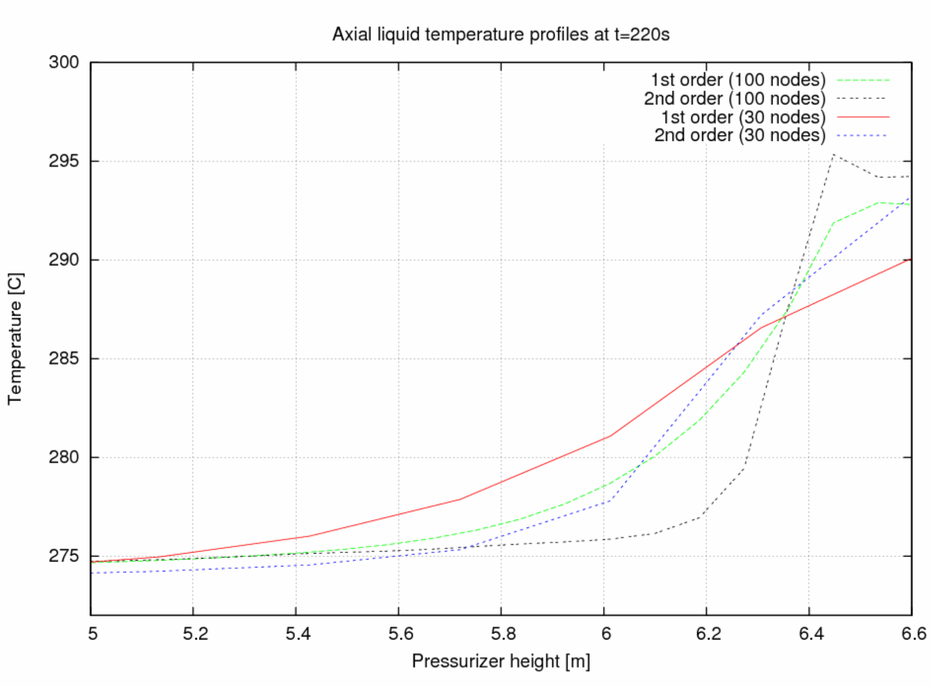

Figure 34. Liquid temperature profiles of 30-node and 100-node models between 5 m and 6.6 m at *t*=220s using both discretization methods.

The effect of the second order upwind option on the pressure behavior of the system was shown in Figs. 25 and 26. Contrary to what was expected, the pressure seems to deviate more from the test results when the improved discretization scheme is enabled. The explanation to this is demonstrated in Fig. 35 which shows the temperature of the node which is at the moment the topmost node containing liquid water with respect to time. Since the node volume in the 100-node model is much smaller than in the 30-node model, the nodes of the 100-node model are warmed up faster than the larger nodes. The temperature difference grows larger towards the end of the insurge, being close to 5ºC at t= 220 s. This has a reducing effect on the heat transfer from steam which becomes greater at the end of the insurge. A warmer node reduces the condensation of steam at the interface, thus contributing to the pressure increase. This observation of increasing error using more accurate model configurations is presumably due to the inaccuracy of the heat transfer correlations used in the code. The condensation calculation may not be as good as the results of Section 6.1.1.1 indicate. One possible cause for the increasing deviation in slower transients is the inaccuracy in the environmental heat loss calculation. If the duration of the transient increases the effect of the heat losses on the system behavior becomes more significant. A too small heat loss would cause a too high pressure rise in the slowest processes. However, this does not seem likely in this case because the final pressure should be higher than the measured final pressure due to a too small total heat loss but as seen in Figs. 21 and 22 the simulated final pressure is slightly lower than the measured pressure.

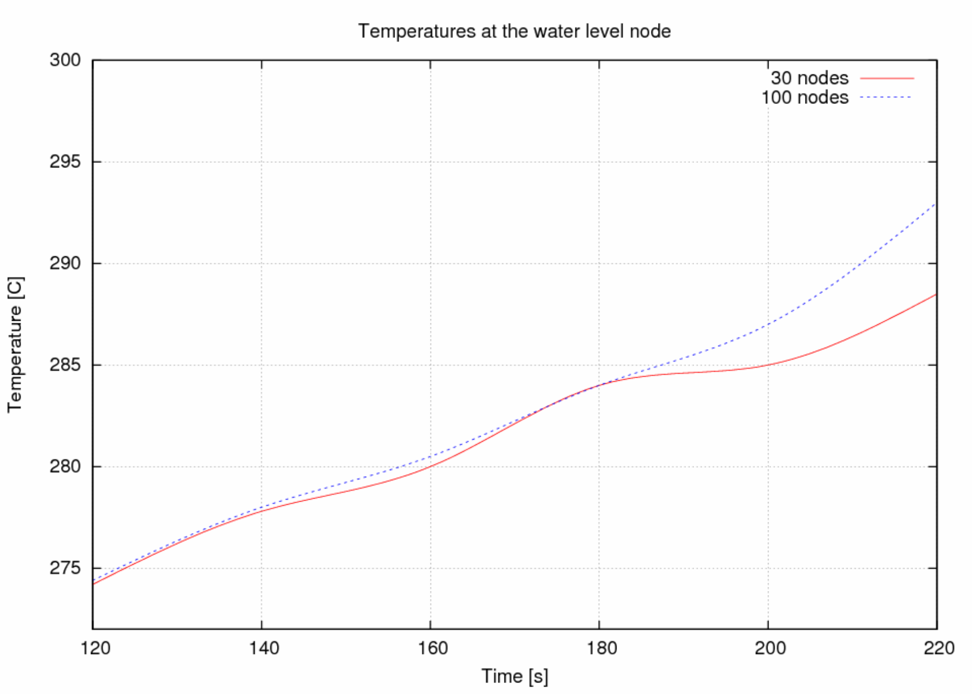

Figure 35. Temperature during insurge in the node at the water level for base model and 100-node model.

6.1.4 TRACE simulations

This section presents comparisons between the TRACE and APROS simulation results and ATWS-10 to ATWS-13 experimental data. In the post-processing of the TRACE simulations the animation model provided by the SNAP package has been utilized. The layout of the SNAP animation model of the pressurizer is shown in Figure 36, 37 and 38. The figures demonstrate the ATWS-10 test at points of time when the insurge is just about to begin, at the end of the insurge when the pressure is at its maximum and at the end of the draining period. The fluid condition range shows how the injected water turns from saturated to sub-cooled as the pressure increases while a layer of warm, saturated water forms on the top of the liquid phase. During the draining period the liquid level decreases near the initial level and steam becoming superheated is seen in the upper part of the tank. The results from ATWS-10 to ATWS-13 simulations using TRACE are shown in Figs. 39-42.

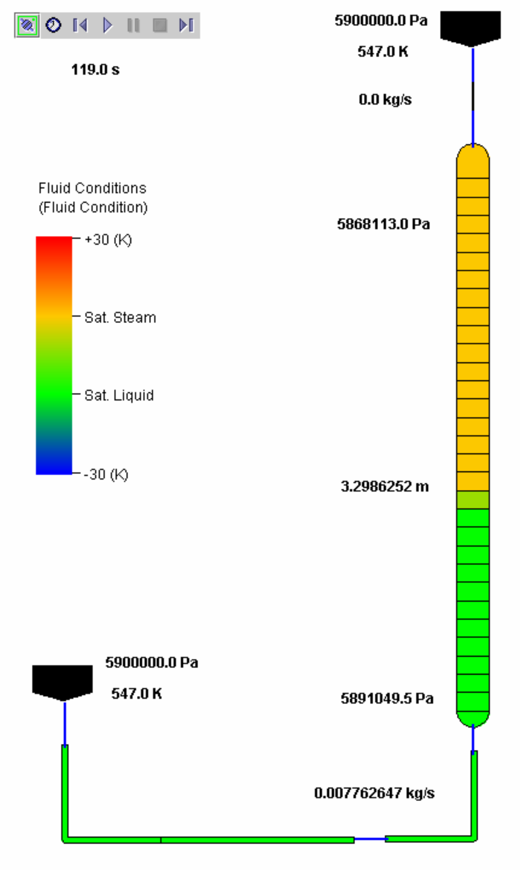

Figure 36. Snapshot of the TRACE calculation animation of ATWS-10 at *t* = 119s.

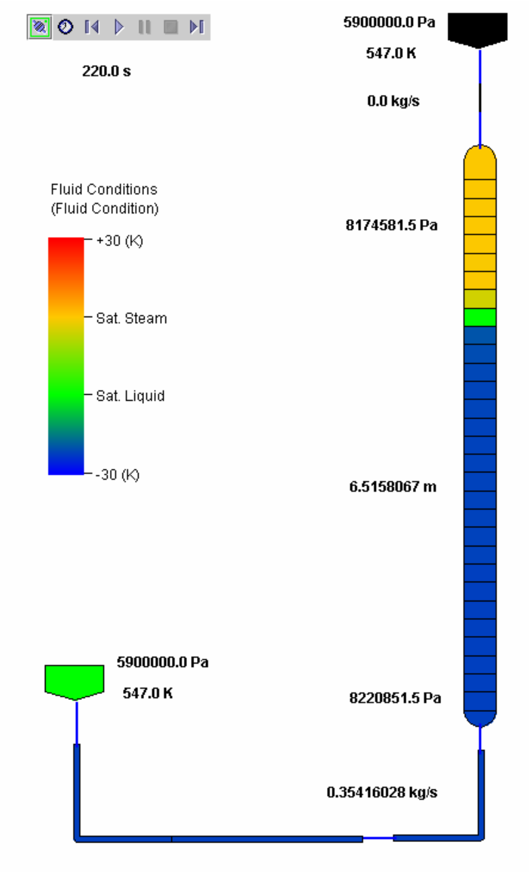

Figure 37. Snapshot of the TRACE calculation animation of ATWS-10 at *t* = 220s.

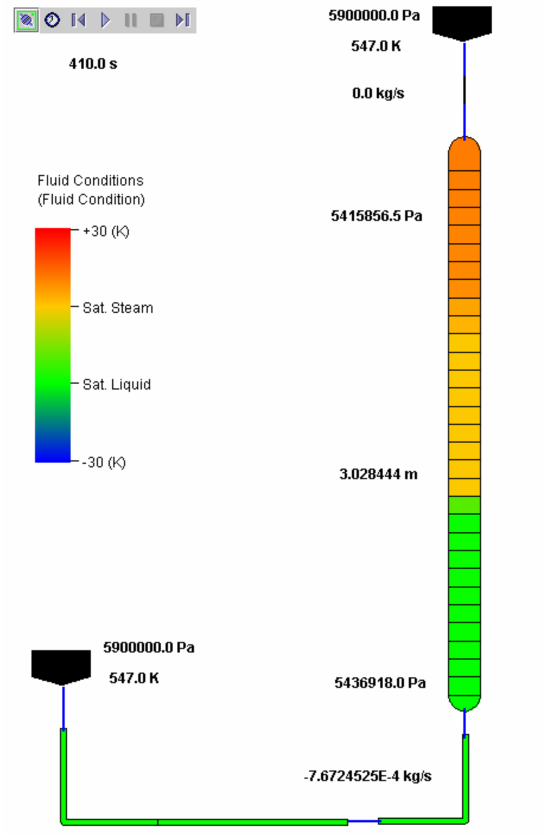

Figure 38. Snapshot of the TRACE calculation animation of ATWS-10 at t = 410s.

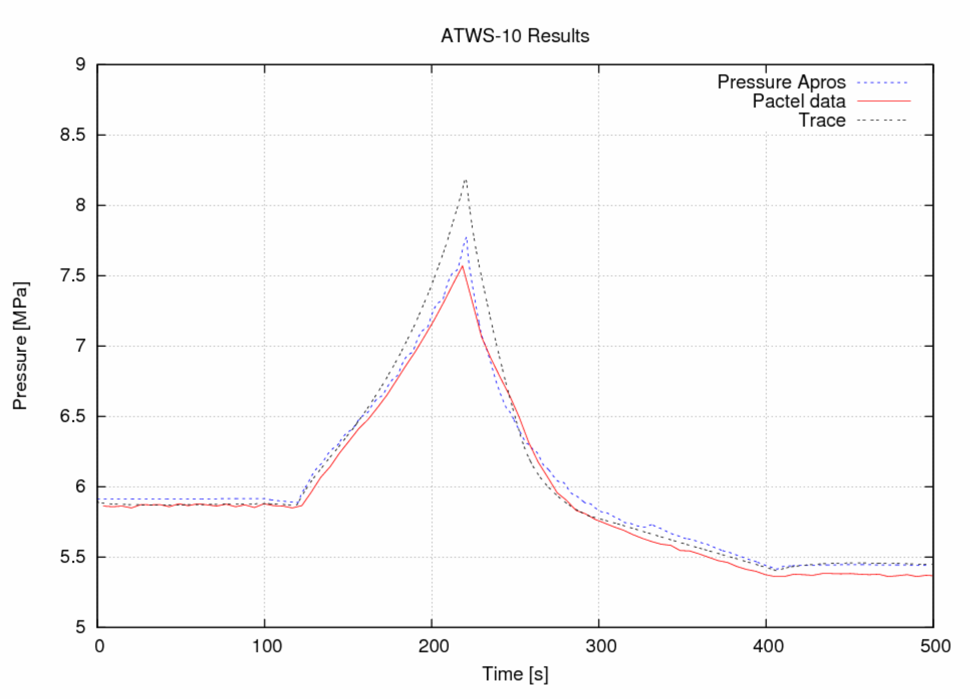

Figure 39. Pressure behavior during ATWS-10 transient.

The maximum pressure computed by TRACE is approximately 8.17 MPa which is 0.37 MPa higher than the pressure obtained using APROS. Possible cause for the higher pressure is that Eq. (16) does not compute the condensation accurately enough but underestimates the film condensation approximately 20% (Spore et al., 2000) which was discussed in Section 5.3.2.1. In case of the slower transients the error becomes greater similarly to what is observed in APROS calculations, as can be seen in the following figures in which the pressures for ATWS -11, -12 and -13 are shown.

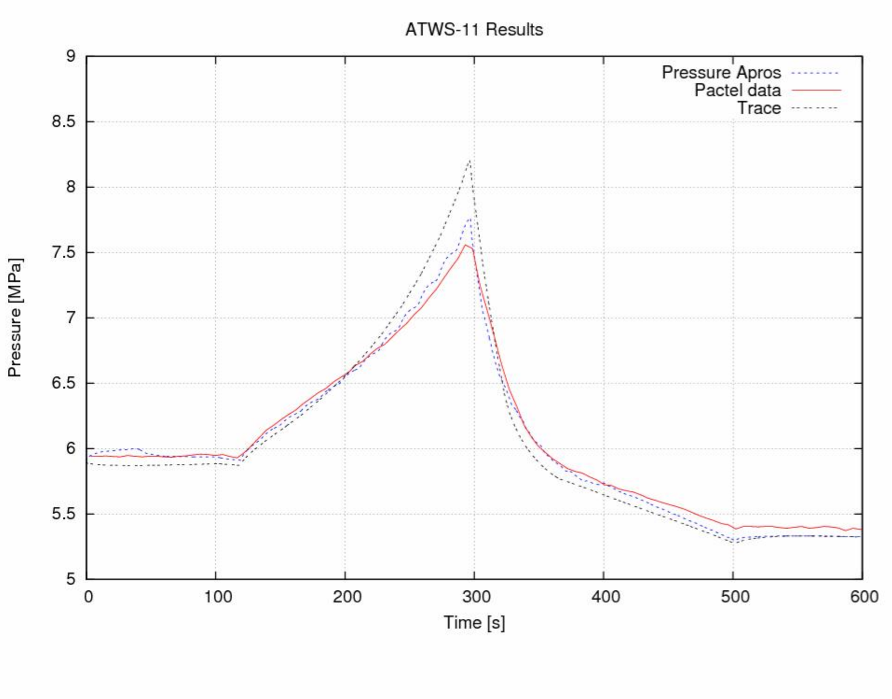

Figure 40. Pressure behavior during ATWS-11 transient.

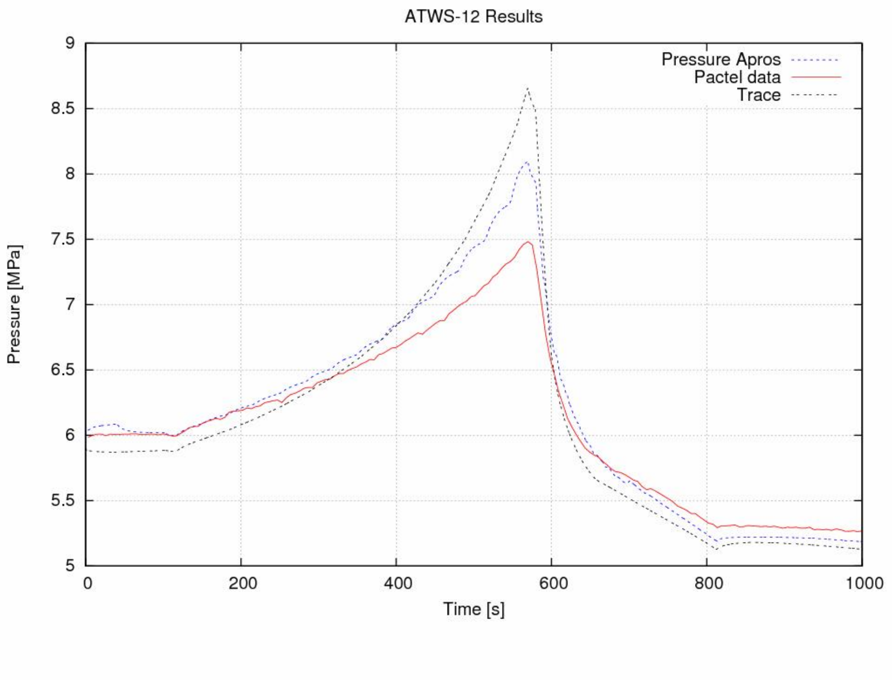

Figure 41. Pressure behavior during ATWS-12 transient.

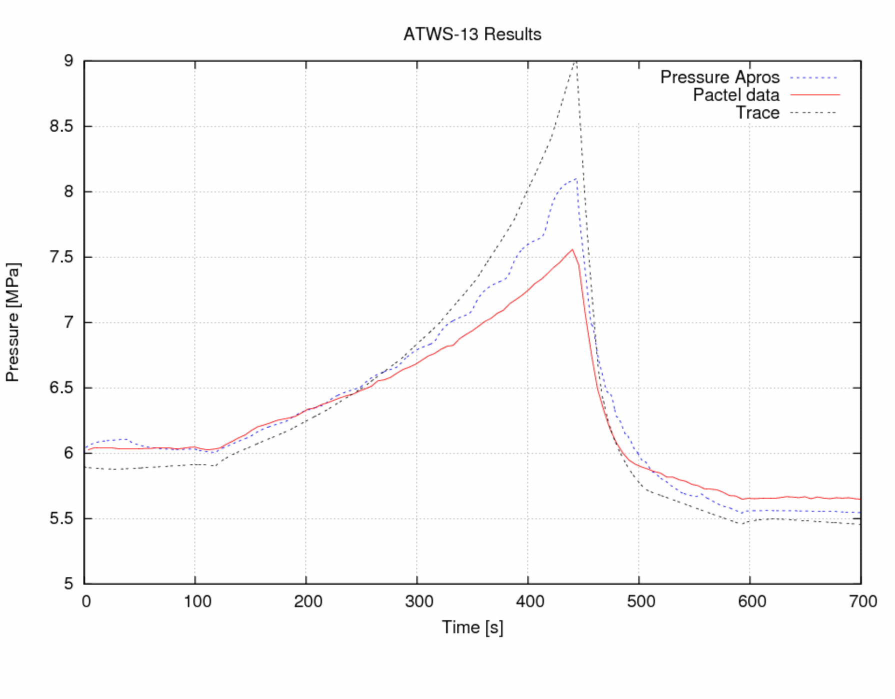

Figure 42. Pressure behavior during ATWS-13 transient.

6.2 ATWS-20 and ATWS-21

The ATWS-20 experiment was simulated with APROS using the Chen correlation which neglects gravity, as well as the full correlation for vertical flows. A comparison of the results is presented in Fig. 43. It was observed that there is a remarkable difference in the pressure behavior during the spray transient calculated using the different correlations. The Chen correlation for horizontal flows predicts that the input of enthalpy by the heaters cancels out the effect of spray cooling when the heater power is 6 kW, and a rapid pressure increase occurs when the full power of 13 kW is used. The reason for this evidently incorrect result is the same as in the insurge and outsurge cases. In addition to the spray cooling, the wall condensation plays an important role in limiting the pressure increase. The pressure increases along the heater-induced temperature rise and the liquid temperature in the steam section nodes becomes higher than the wall surface temperature, which is supposed to result in effective film condensation on the wall. Again, the gravity term is not taken into account and the Nusselt number as well as the heat transfer coefficient is calculated to be unrealistically small. As expected, the simulations showed that the Shah correlation is not capable of predicting the behavior correctly, either. As was the case with the insurge and outsurge transients, the Chen correlation for vertical flows is the correct choice for the spray transients too.

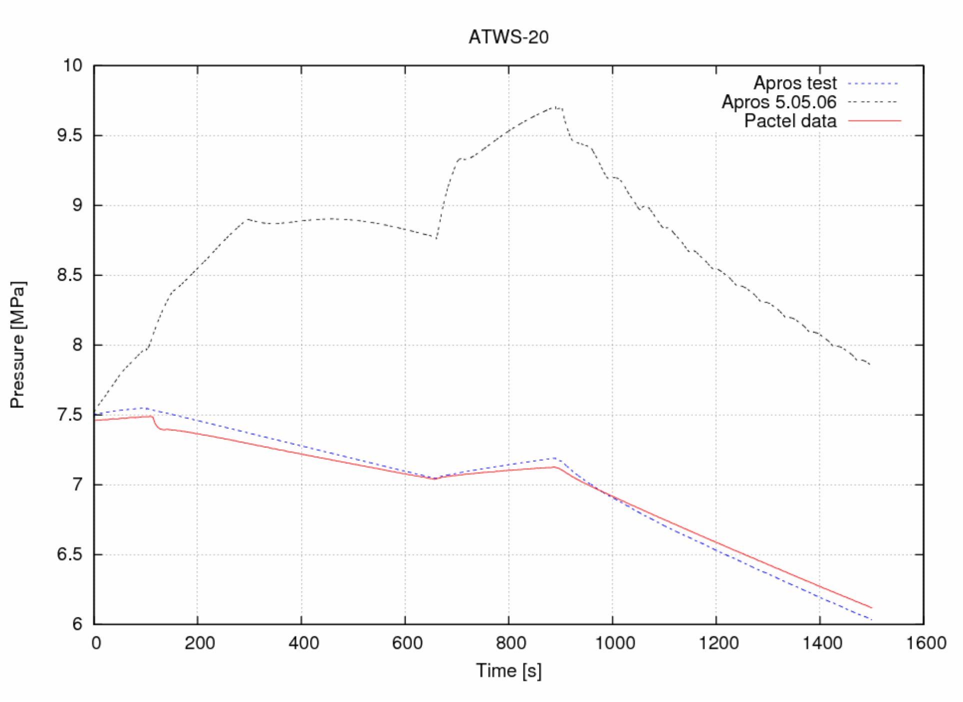

Figure 43. Pressure in ATWS-20 test calculated using APROS 5.05.06 and test versions.

Figure 44 shows the comparison of the APROS test version to the experimental data with a smaller y-range. It is seen that in the simulation after the onset of spray the cooling and the pressure drop is faster, and as the 7 kW heater is turned on the pressure starts to increase more rapidly than the measured pressure. After the heaters are turned off to prevent the pressure increase the pressure drops again fast. However, the difference is only 0.1 MPa at most so the calculation data correspond the test data well, taking into account that the inaccuracy of the pressure measurement could be close to ±0.1 MPa as described in Section 6.1.1.1. The accuracy of the spray flow rate according to the test error estimate is ±0.00079 kg/s.

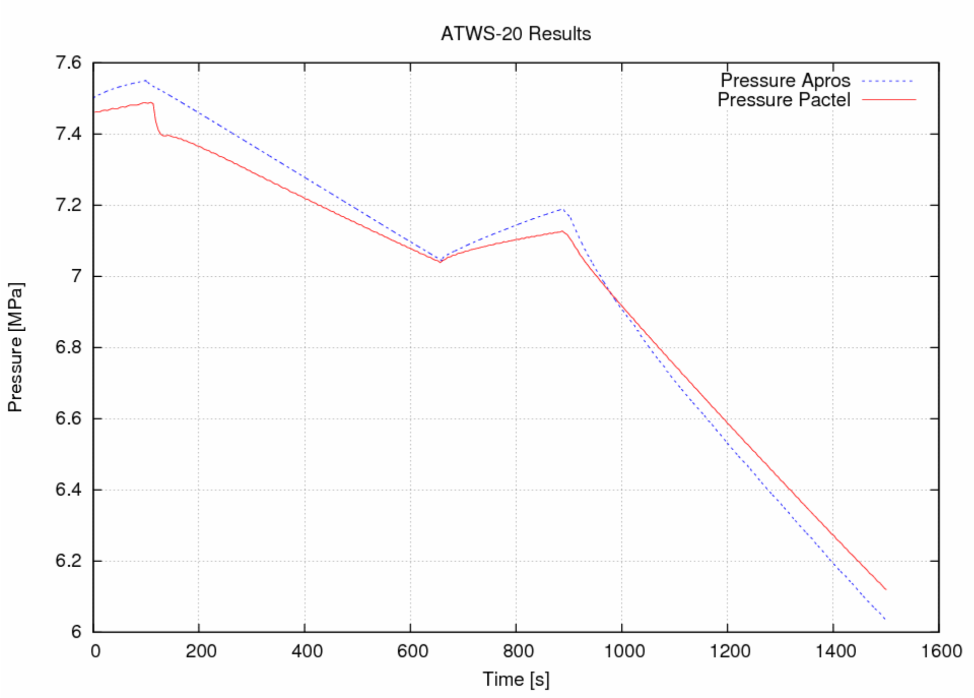

Figure 44. Pressure behavior during the ATWS-20 test.

The ATWS-21 transient in Fig. 45 shows a good correspondence with the test results. After the onset of the spray when the 6 kW power is inserted to the fluid the pressure drops a little faster than expected as was the case in the ATWS-20 test. In this case when the full power of 13 kW is utilized, after around *t*=400 s, the spray injection rate of 1.0 kg/min is high enough to keep the pressure dropping at a rate similar to what was measured. At this time the deviation is 0.1 MPa.

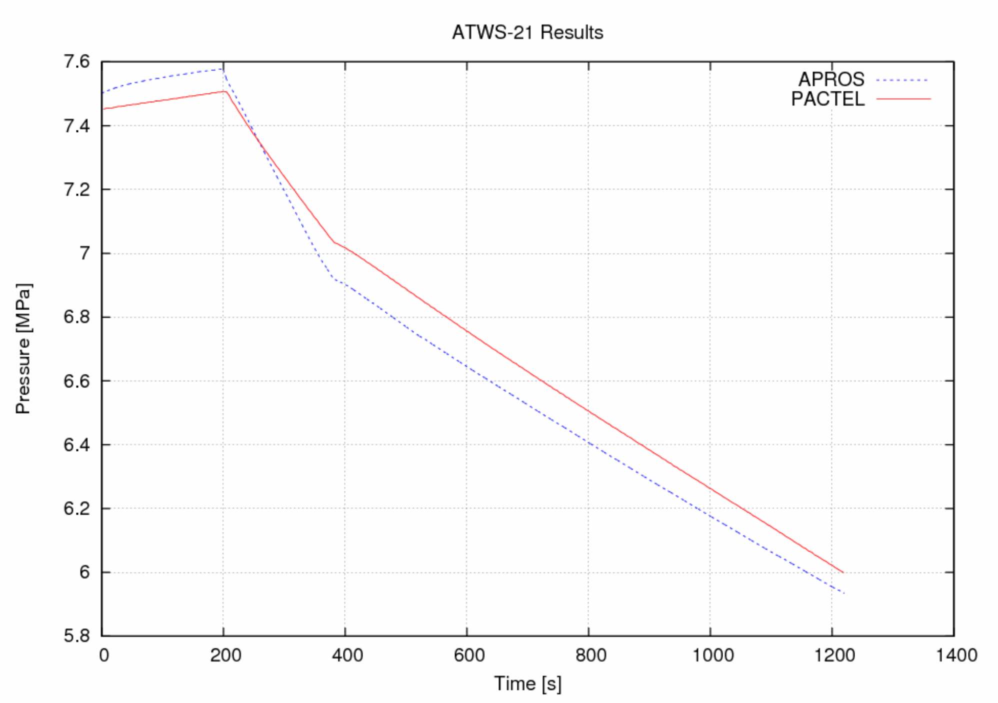

Figure 45. Pressure behavior during the ATWS-21 test.

6.2.1 Spray parameters

The most important spray parameter playing a role in the effectiveness of the spray cooling is the droplet size. The diameter of spray droplets depends on the nozzle geometry. A sensitivity study was performed by using three different values (4 mm, 10 mm and 1.5 mm) for hydraulic diameter for the orifice through which the water is injected into the tank, in addition to the actual diameter (3 mm) of the spray orifices in the PACTEL pressurizer. No significant effect on the pressure curve was observed which is somewhat unexpected. This result may need further investigation.

The injection cooling option, which is related to the branch component, was enabled for the branch included in the pipe component representing the spray line, located between the spray valve and the topmost thermal hydraulic node of the pressurizer. This parameter transmits an additional cooling term to the node next to the outlet of the pipe to account for the locally increased heat transfer caused by the additional turbulence near the liquid jet. A comparison of a spray simulation run in which the injection cooling was disabled to a run where it was enabled showed only a small increase in the internal heat transfer coefficients of APROS if the injection cooling was on. The effect of the cooling on the pressure behavior is practically negligible.

6.2.2 TRACE simulations

The SNAP animation snapshots of the ATWS-20 transient are shown in Fig. 46 (a) and (b). The fluid condition range shows that the water and steam are nearly saturated throughout the transient, only the level increase of approximately 0.66 m is visible in the cell fluid condition indicator. The pressure behavior comparison between results from both codes and test results for ATWS-20 and ATWS-21 are presented in Fig. 47 and Fig. 48. The comparisons of the TRACE and APROS simulations to the experimental data of ATWS-20 shows that the spray is computed by both codes to be slightly more effective than measured at PACTEL at the time range between 100 s and 660 s when the total power distributed by the heaters is 6 kW. The pressure begins to increase at 660s when the 7kW heater is turned on. TRACE exaggerates the pressure rise but the pressure drops quickly when the heaters are turned off at 890-960s. As seen in Fig. 48 the TRACE pressure calculation of the ATWS-21 test is almost identical to the APROS calculation and the codes predict the pressure with good accuracy.

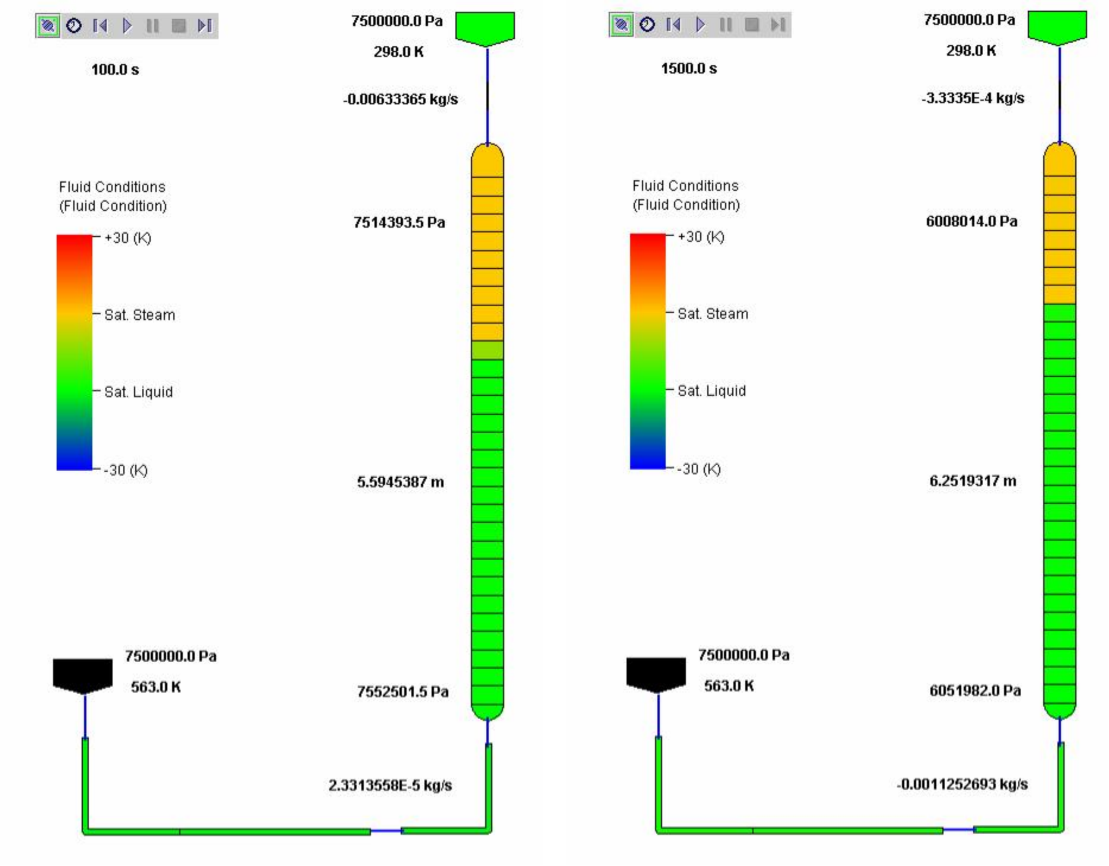

(a) (b)

Figure 46. Snapshots of the ATWS-20 animation at (a) *t* = 100s and (b) *t* = 1500s.

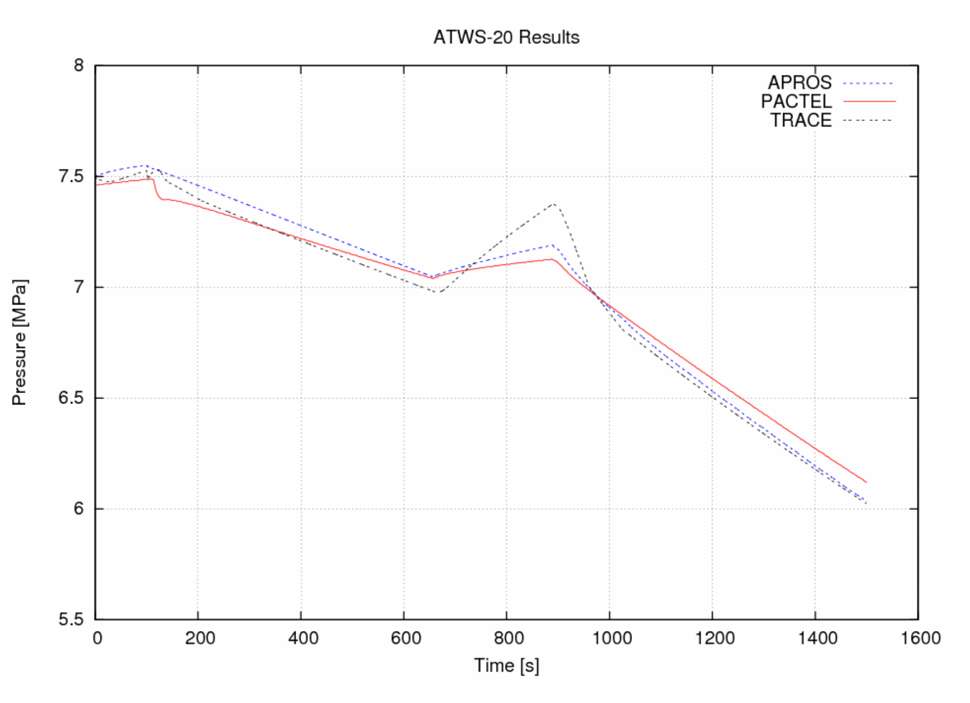

Figure 47. Pressure behavior during the ATWS-20 test.

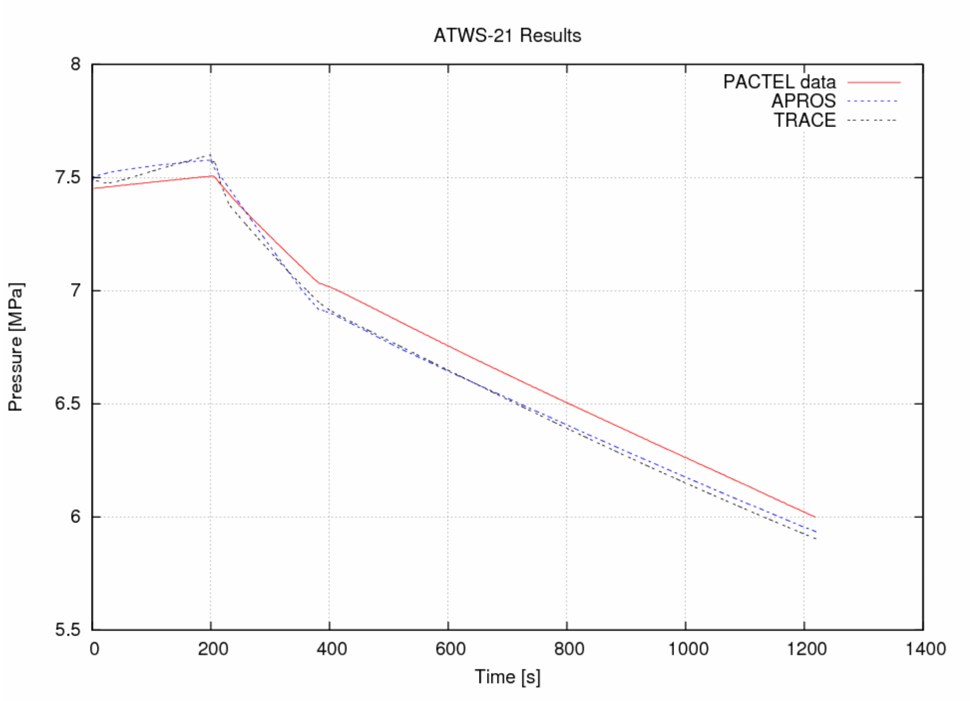

Figure 48. Pressure behavior during the ATWS-21 test.

6.3 MIT Pressurizer

6.3.1 Insurge to a partially full tank

In this experiment cold water of 24ºC was injected into the pressurizer at a rate of approximately 25 kg/s during 63 seconds, starting at *t*=22 s. Initially the system contained saturated liquid and steam at 0.69 MPa. The water level was 0.36 m. The pressure comparison between the measurement, APROS simulation and TRACE simulation is shown in Fig. 49. The accuracy of the measured pressure in Fig. 49 is approximately ±0.002 MPa which is also true for the pressure scale of the four other MIT tests.

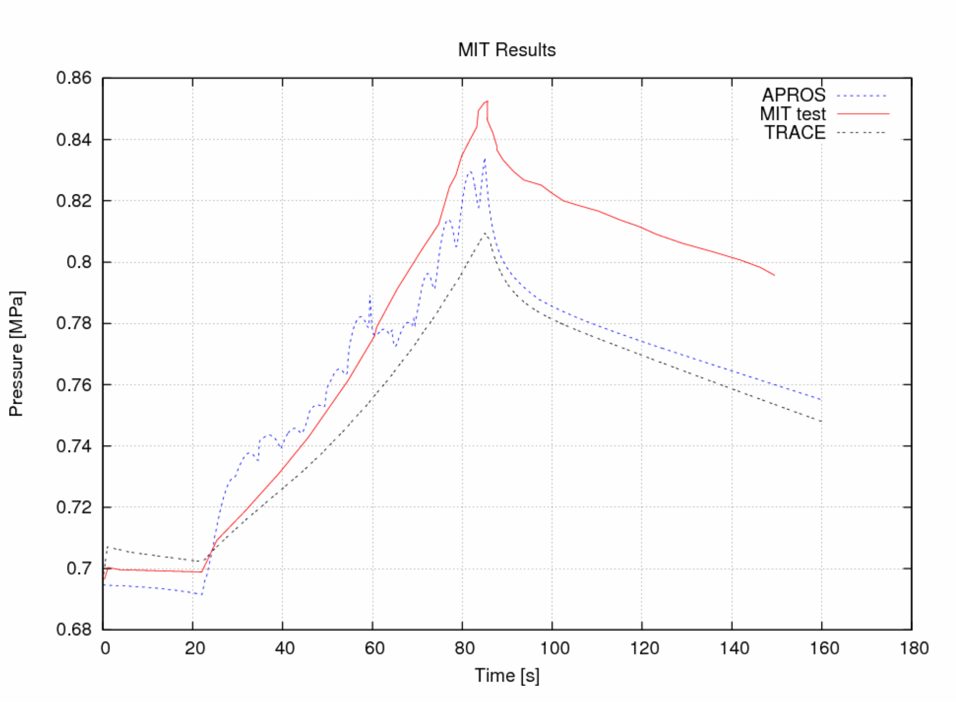

Figure 49. MIT insurge pressure behavior.

Contrary to the results of the previous insurge transients, both the APROS and TRACE simulations predict a lower maximum pressure than the measured pressure. During the insurge there is a noticeable oscillation in the pressure in the APROS calculation. The probable cause for the unsteady behavior is that the inside wall is slightly colder than the liquid temperature of the node in which the water level is located. Hot water entering a node with cooler wall enhances the wall condensation for a short time until the wall is warmed up and the node is submerged. This phenomenon is repeated as the water advances from node to node. Using a denser, two-channel nodalization could help to remove the problem. A possible cause for the oscillation being so remarkable could also be an uncontrolled “sloshing” of water in the tank as a result of the fact that in APROS the pressurizer walls are smooth and the flow in the calculation level branches of the pressurizer component is practically frictionless. In the MIT cases, the pressure is relatively lower than in the other facilities in this study and thus the density of the steam is lower. When the steam has a low density and there is no friction even a little condensation or evaporation can cause rapid changes in the pressure and high-velocity flows near the liquid surface, and liquid level and pressure start to oscillate. Also, the numerical error increases in low-pressure conditions as the difference in the densities of water and steam is significantly greater than in high-pressure systems such as the PACTEL facility. However, though being relatively low, the pressure in the MIT tests is still remarkably higher than the atmospheric pressure and thus should not require any low-pressure calculation options to manage the calculation.

In the previous insurges the injected water was saturated in the beginning of the test but this time the water temperature is much lower than the initial saturation temperature which is 164.5ºC. Thus, there is a remarkable difference between the initial wall temperature and the node average temperature, and the heat transfer by natural convection from the hot wall to the cold liquid plays a role. To examine the mixing of hot and cold water in the water section of the tank let us have a look at the axial temperature distribution at the end of the insurge in Fig. 50. In the bottom of the tank the water is at the injection temperature. In the test data a sharp enthalpy change is located around node 14. The distribution is smoothened by both calculations but at the top of the tank and at the water level (node 22) the temperatures do not differ much. An APROS run using the second order enthalpy discretization showed no remarkable improvement on the pressure behavior.

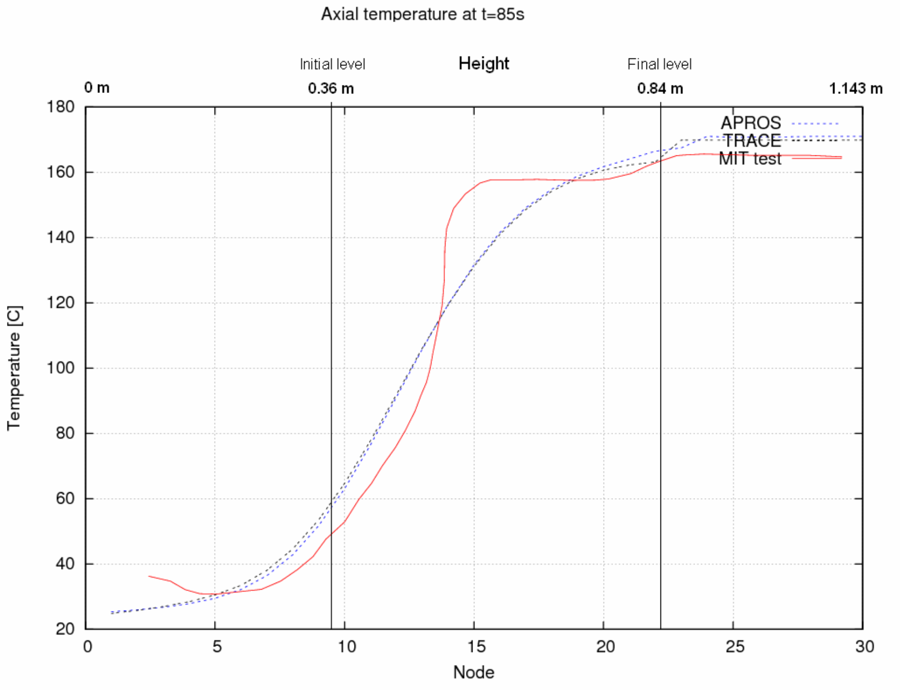

Figure 50. Axial temperature at *t*=85s.

In order to investigate why the pressure is computed to be too low the mass and heat transfer rates at the water level node were also re-examined. A case was run where the injected water was saturated which predicted a higher pressure the same way as was observed in the PACTEL ATWS insurges. As expected based on the small temperature differences there seemed to be no significant discrepancies in the condensation occurring in the vicinity of the phase interface. However, the pressure response is quite sensitive even to small changes in the condensation process. The dependence of the pressure response on the injection water temperature may be explained by the aforementioned sloshing in the tank which could permit some of the cool injection water to rise to the upper part of the water volume and thus have an effect on the condensation.

6.3.2 Outsurge

In this experiment, water was drained from the tank at an average rate of 0.35 kg/s. As seen in Fig. 51 both codes predict a more drastic pressure drop than expected. In the initial state the liquid level is 0.75 m. The level drops to 0.24 m in the end of the outsurge according to the test data but in the simulation the level is drained to 0.09 m until the outsurge stops. This may indicate that the flashing is underestimated. The pressure jump in the beginning of the TRACE simulation could not be explained.

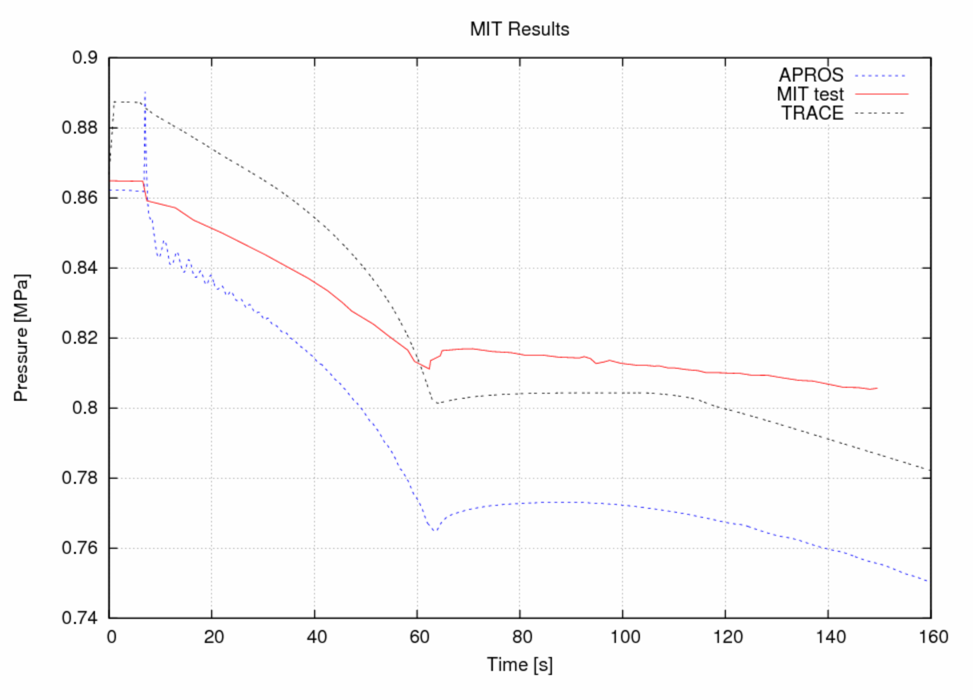

Figure 51. MIT outsurge pressure behavior.

6.3.3 Insurge to a hot tank

In the initial state of this experiment (the state just before insurge) the wall temperature is approximately 5°C higher than the vapor temperature and heat is transferred by natural convection to the vapor. The pressure rise is closer to isentropic than in the simple insurge experiment because practically no heat is lost from the vapor phase. Condensation at the wall starts when the tank pressure reaches the saturation pressure of the initial wall temperature. The vapor superheat is increased linearly until the start of condensation which starts to limit the pressure and temperature increase. The test data curve of Fig. 52 shows that the onset of condensation occurs at *t* = 82s.

TRACE predicts the pressure rise to the saturation pressure corresponding the wall temperature to be more rapid. After the start of condensation the pressure rise is effectively reduced. After the insurge the peak pressure drops again fast. The APROS calculation shows a pressure rise in the beginning of the insurge but around the time the condensation starts the pressure begins to oscillate and the pressure does not increase as supposed. The phenomenon is similar to that observed in the simple insurge transient.

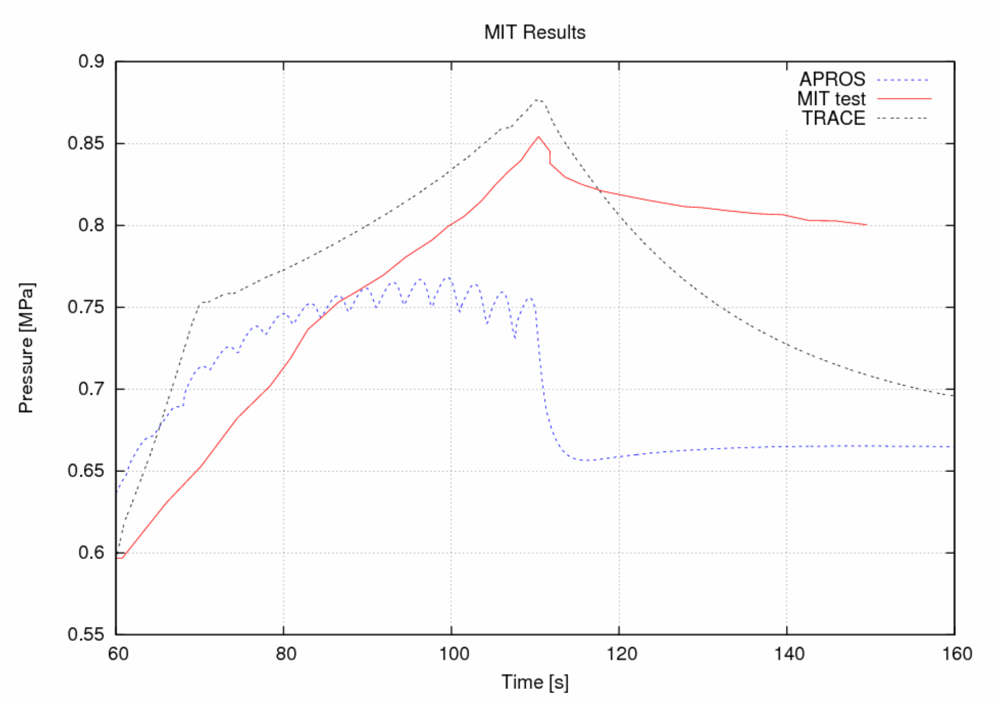

Figure 52. MIT insurge to a hot wall pressure behavior.

6.3.4 Outsurge after insurge

This experiment is similar to the ATWS-10 – 13 experiments. The insurge phase does not differ from the MIT simple insurge phase but during outsurge the pressure must first drop to the initial saturation temperature before evaporation starts to limit the pressure decrease. It was observed that TRACE simulated the pressure behavior very accurately as can be seen in Fig. 53. The peak pressure is slightly below the measured maximum pressure but generally the correlation is good.

Again, the APROS model was not very stable in the simulation and the predicted pressure rise is too low. In the beginning of the insurge an unphysical spike is seen in the pressure curve which may be due to unstable sloshing of water at the pool surface. This unstable behavior can also have an effect on the heat transfer as explained in Section 6.3.1 which could explain why APROS predicts a too low pressure for all the MIT insurge transients, excluding the empty tank insurge in which the whole process is very different from the other three insurge transients. A test case showed that including a form loss in the calculation level branches removed the spike from the curve but generally there was no significant improvement to the pressure calculation. The outsurge phase is calculated accurately by both codes. It was noticed that especially TRACE calculation is very sensitive to the initial wall temperature. Thus, it is important that the wall boundary conditions, or the steady state prior to the experiment, are set correctly.

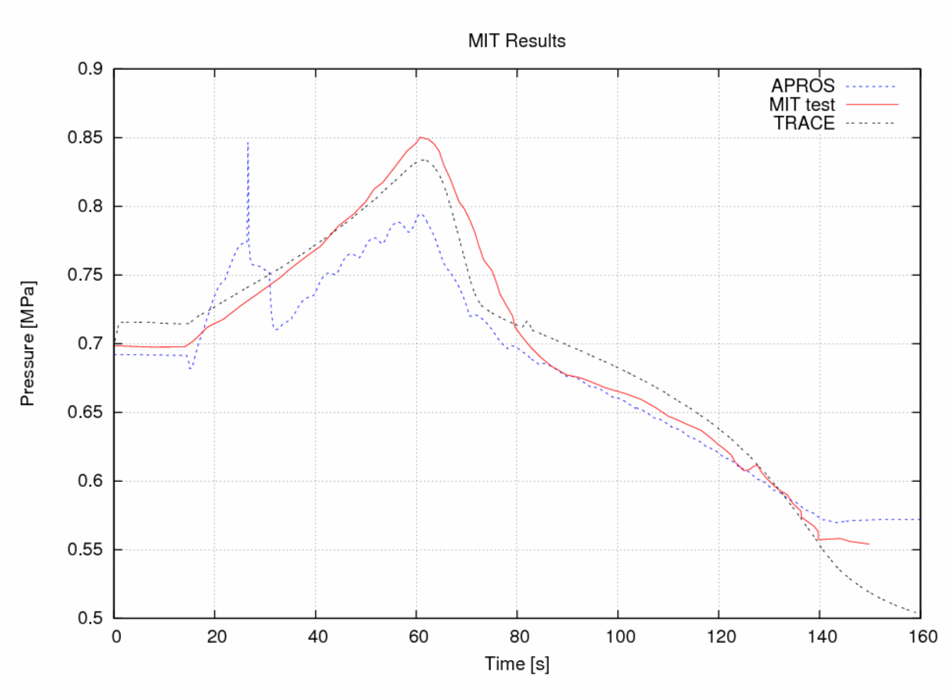

Figure 53. MIT insurge-outsurge pressure behavior.

6.3.5 Empty tank insurge

The heat transfer phenomena occurring in this test are different from the other insurge cases since initially there is no water in the tank which would absorb the momentum of the insurge jet and cause the piston effect, and the water sprays directly into the vapor volume. This results in greatly enhanced interfacial condensation on the injection droplets. First, the interfacial heat transfer causes the pressure to drop sharply. As the water level rises the effect of condensation on liquid spray is reduced, the pressure drop slows down and finally the pressure starts to increase when the steam compression starts to dominate the process. According to Kim (1984) the penetration depth for the sparger used in the test facility is about 0.18 m for a flow rate of 0.45 kg/s.

The initial steam and wall temperature in the tank is 169ºC. The insurge temperature is 23.9ºC and flow rate approximately 0.27 kg/s. The pressure comparison is shown in Fig. 54. APROS calculates the pressure drop accurately but fails to simulate the pressure increase correctly as was the case with the previous MIT insurges. The TRACE simulation of the transient was not successful. The pressure even stays constant in the beginning, then drops very slowly throughout the insurge until drops to a stationary state after the insurge.

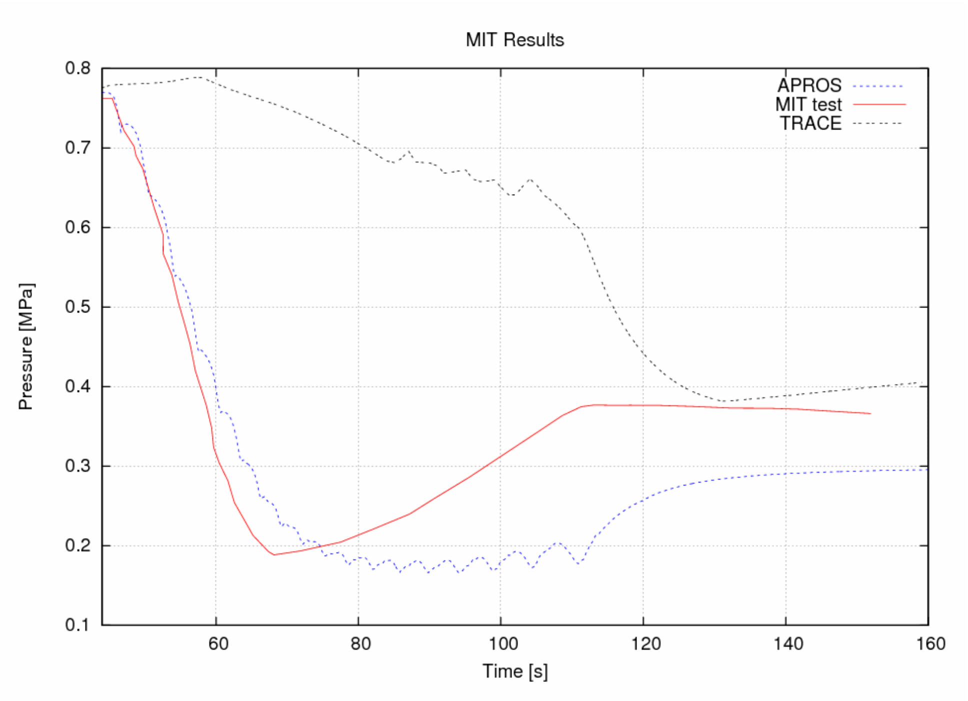

Figure 54. MIT insurge to an empty tank pressure behavior.

The thermal hydraulic codes can not simulate the high velocity insurge jet which is distributed into the vapor mechanistically. The rapid pressure drop observed in APROS is due to increase in the interfacial condensation on the surface node which results from the small amount of saturated water in the bottom getting mixed to the cold insurge water. The cold water is in contact with the hot vapor until the water is deep enough for a layer of saturated water to form on the pool surface without being disturbed by the insurge water.

The TRACE and APROS models were also tested using several initial water levels. In the cases presented in Fig. 54 there was a very small amount of saturated water (2-3 cm) in the bottom of the tank. If the initial water level was raised the pressure decrease became slower because the mixing is not as effective and the saturated layer is formed sooner. In reality the pressure drop stops because water reduces the momentum of the insurge jet and causes the insurge water to get warmer prior to entering the steam volume (Kim, 1984). Kim (1984) also reported that the pressure response is very sensitive to the initial water depth. Performing calculations with different initial levels did not significantly improve the performance of TRACE.

In TRACE the churn (transition) flow regime is selected by the code, for which the interfacial heat transfer is solved by using an interpolation of the bubbly slug and annular-mist regimes. The weighting factor for averaging the parameters for the regimes is based upon void fractions. No separate effect assessment for this flow regime has been performed since there are no heat transfer models developed specially for churn flow (Spore et al., 2000). One possible reason for the TRACE results is that the heat transfer correlations are not suitable for this type of case. In APROS the stratified or droplet flow regimes are selected rather than bubbly slug or annular regimes. Thus, the two codes may have a very different approach to the same transient. Also, the very high initial temperature difference between the injected water and the wall may cause problems in the calculation process.

6.4 Neptunus Y05

The Neptunus Y05 experiment consisted of four successive insurge and outsurge transients in which the spray was in use simultaneously with the insurge phases. The mass flow rates of insurge and spray of the experiment are presented in Fig. 55.

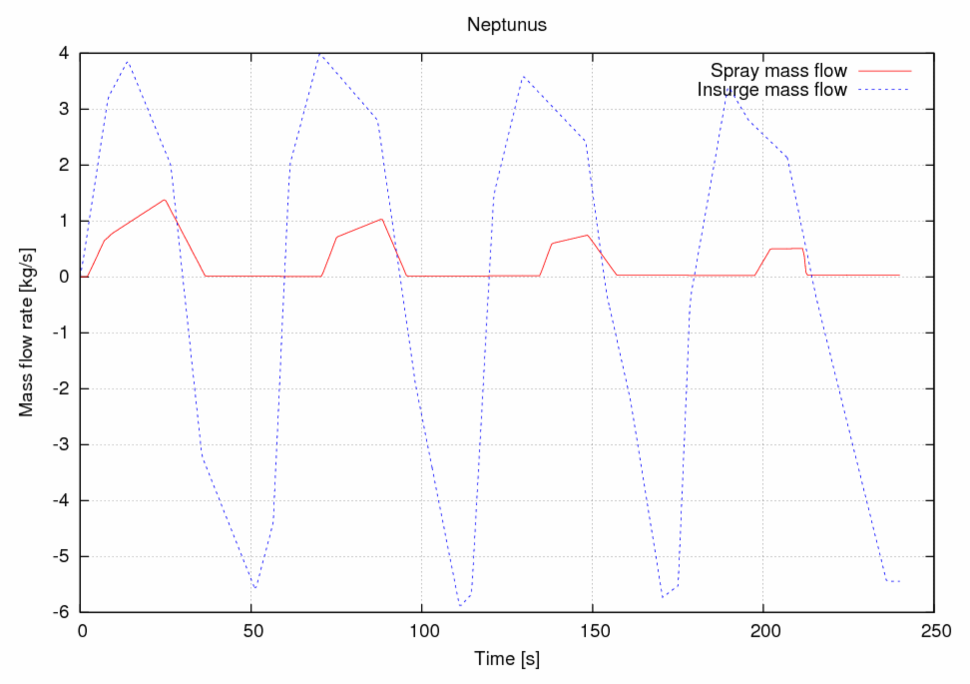

Figure 55. Insurge and spray mass flow rates of Neptunus Y05 test according to Peterson (1984).

6.4.1 APROS simulation

The pressure comparison of the APROS results and the measured data, which is given in Fig. 56, shows that the largest deviation of the calculated pressure from the measured pressure occurs during the first two insurges in which the calculated peak pressure is approximately 0.5 MPa too high. Correspondingly, the minimum pressure is computed to be too high for each outsurge. In the last two insurges the relative pressure rise is small and the peak pressures appear to correspond the measured pressures whereas the minimum pressures are too high. It is observed that the pressure does not start to drop until there is a significant decrease in the surge flow. The measured data show that the initiation of spray flattens the pressure rise quickly. The underestimated effectiveness of spray is also seen in the last insurges where the peak pressures are lowest even though the flow rate and duration of the spray is at its minimum. The PACTEL ATWS runs showed that APROS tends to slightly exaggerate both spray cooling and insurge pressure rise making it difficult to discern the contribution of spray and insurge in this type of experiment. A phenomenon adding to the complexity of the case is that in a simultaneous spray and insurge the spray drops which hit the pool surface disturb the saturated layer on the surface and the cool water below is exposed to the vapor which increases interfacial condensation. This is not taken into account in the APROS models.

Generally, the correlation between the simulation and the measured data is good. In this pressure scale the system is quite sensitive to changes especially in the insurge flow rates. The digitization of the measured data from the report of Peterson (1984) and the interpolation of the data to the form in which it is used in APROS causes small errors to the boundary condition mass flows. Naturally, the accuracy of the original data depends on the measurement system of the test facility which is described by Peterson (1984) to have been very limited. The report also states that the spray water temperature varied between 227ºC and 318ºC but no information about the nature of the variation was given. The average temperature was used in the simulations. In reality, temperature differences of this magnitude may result in remarkable differences in the results.

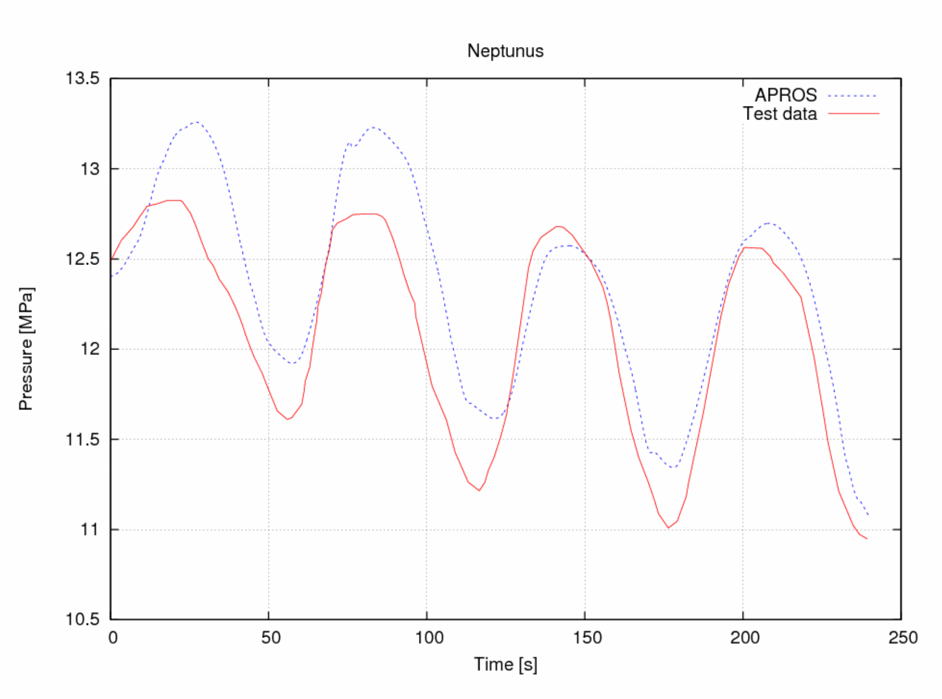

Figure 56. Pressure behavior of Neptunus Y05 experiment.

6.4.2 TRACE simulation

TRACE exaggerates the pressure rise more than APROS as is seen in Fig. 57 where the calculated pressure is compared to the measured value. The maximum pressure is as much as 1 MPa too high. A better prediction for the minimum pressures is obtained.

Other analysts have also obtained similar results of the Neptunus Y05 test in which the peak pressures are too high such as Peterson (1984) who used the test to assess the TRAC-PF1/MOD 3 code which is one of the predecessors of TRACE. The RELAP-3D, which is an outgrowth of the one-dimensional RELAP5/MOD3 code developed at the Idaho National Engineering & Environmental Laboratory (INEEL) for the NRC, also showed poor comparison with the data for pressurizer calculations before an improved pressurizer condensation model was introduced (Weaver, 2004). Several modifications were added to the interfacial condensation model of which the most important was a model which calculated the enhanced condensation by spray droplets disrupting the saturated water layer. The enhanced mass transfer rate is a product of spray impingement rate, ratio of pool sub-cooling and heat of vaporization and a user input constant (Weaver, 2004). This type of model could provide an improvement also to the TRACE calculation.

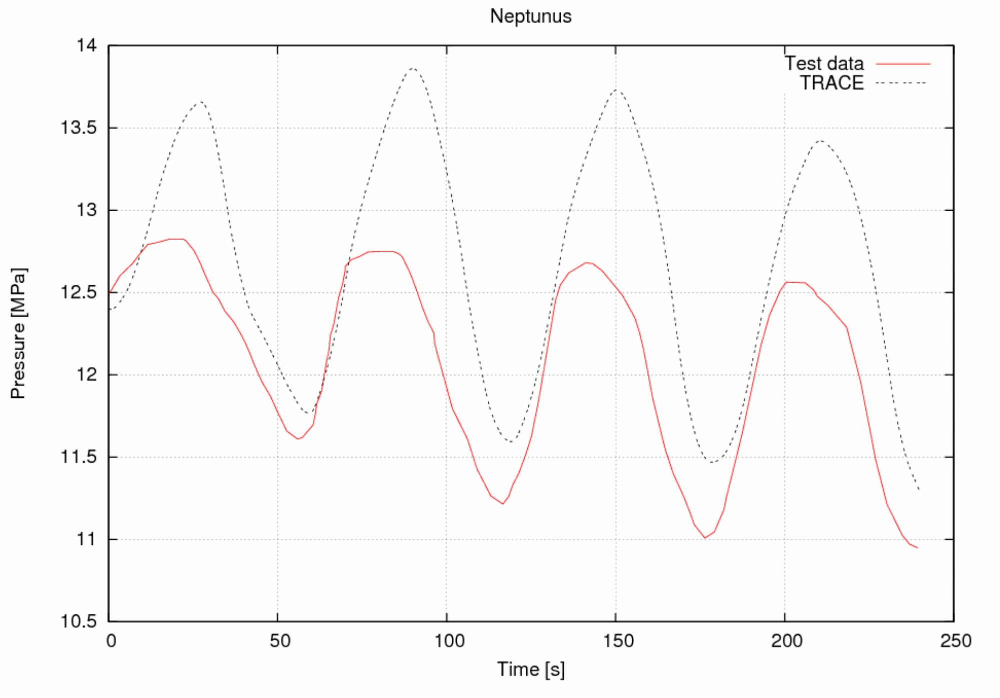

Figure 57. Pressure behavior of the Neptunus Y05 experiment

6.5 Loviisa turbine trip transient

The measured pressurizer level and the level approximation used in APROS during the transient are shown in Fig. 58. The APROS mass flow rates are computed from the pressurizer level measurement and the mass flows in and out of the pressurizer are thus integrated into the one mass flow boundary condition which is the surge line branch. The condensation and evaporation mass transfers can be considered to be too small to have a significant effect on the pressurizer level. Also the heat loss to the environment is not taken into account since in the power plant scale the heat losses are relatively very small compared to the heat losses in the volume scaled test facilities.

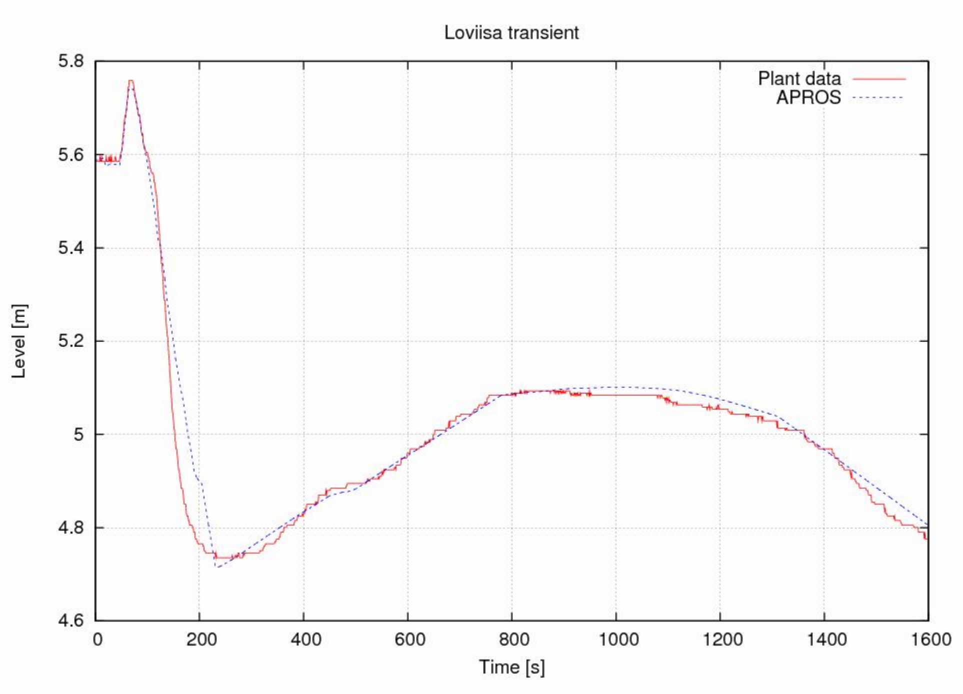

Figure 58. Pressurizer level.

The pressure during the transient using the Shah correlation and the Chen correlation for vertical pipes is shown in Fig. 59. The higher pressure predicted by the Shah correlation can be seen in the pressure peak at the initiation of the transient when the by-pass valves are opened and more clearly when the level and the pressure increase between t = 230 s and t = 800 s. As expected, the cooling period pressure drop is calculated similarly by both correlations. A spray flow of 0.1 kg/s is injected into the pressurizer throughout the transient to simulate the continuous spray during normal operation. Also two spray valves are open between t = 15 s and t = 20 s which provide a spray rate of 7.6 kg/s. The spray line is connected to a cold leg downstream of the main circulation pump and the average cold leg temperature of the transient was used in the calculation. It is seen in Fig. 59 that in the simulation the short spray injection is not able to cut the pressure increase in the beginning of the transient but the predicted peak pressure is too high also in the case in which the Chen correlation is utilized. Initially, it was assumed that two heater groups, which are almost all the time on during normal operation, and two heater groups, which are on from time to time to compensate the environmental heat losses and the continuous spray, were on providing 360 kW heating power to the water. The 180 kW heater group was switched on at t = 37 s, the 360 kW group at t = 69 s and the 720 kW group at t = 77 s and all the heaters were on for the rest of the transient. The exact operation of the heaters during the transient, or in the initial steady-state, is not known, nor attempted to simulate in detail in this case. Also the heat losses to the environment were neglected, thus the present model is not an exact model of the Loviisa NPP pressurizer but contains some inaccuracies in the boundary conditions which may also cause discrepancy in the results. For investigating the scaling effect on the performance of the two heat transfer correlations, however, the model is satisfactory.

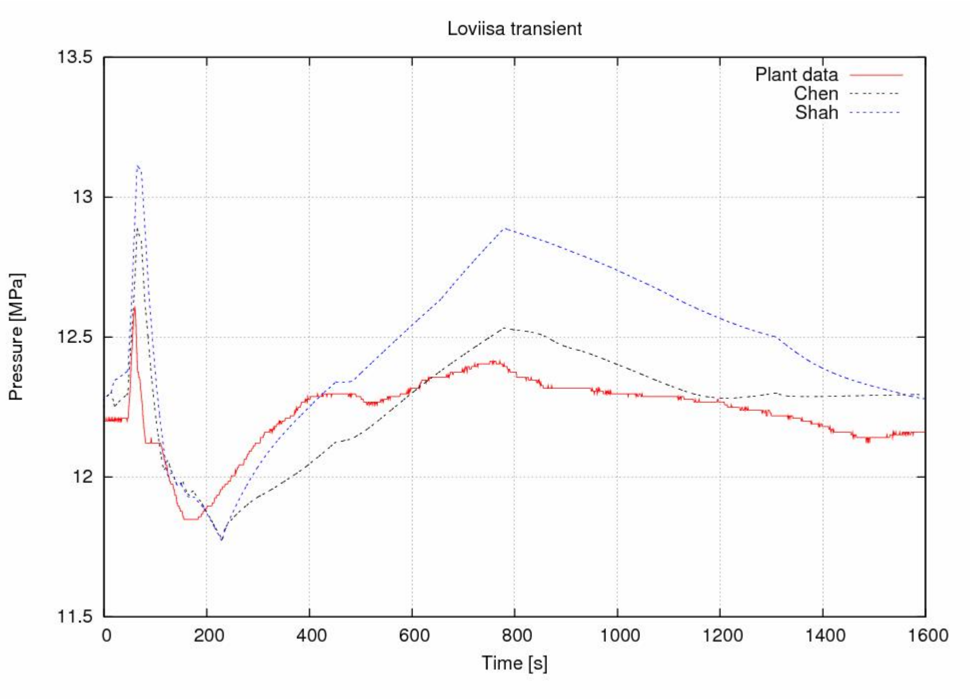

Figure 59. Pressure using the Shah and Chen (APROS test) condensation correlations.

The deviation in the two different calculations is nearly 0.4 MPa at most. Relatively it is not as high as in the smaller test facilities but clearly noticeable. In a realistic power plant scale the contribution of the interfacial condensation to the total condensation is larger since the pool surface area is very large compared to the wall area and the interfacial condensation reduces the pressure rise. For example, the pressurizer of the PACTEL test facility is as high as the pressurizer of the Loviisa NPP but very narrow since the volume scale is 1:305. However, it is clear that selecting the appropriate wall condensation correlation has a remarkable effect on the system behavior also in large-scale power plant simulations. A slight improvement to the performance of the Shah correlation simulation was observed if the injection cooling option was enabled for the spray line branch while the injection cooling had no noticeable effect in the case of Chen correlation, as was noted in Section 6.2.1, but this has no significance since the Shah correlation is not suitable for the case. The Chen correlation for horizontal flows in which the gravity term is neglected gives similar results than the Shah correlation.

6.6 Remarks and suggestions for code improvement

The results of all the insurge transients examined in this work showed clearly that the two heat transfer models for film condensation which were available in APROS were not suitable for calculating pressurizer transients, or consequently any phenomena in which laminar, vertical flow and heat transfer are present. APROS was updated to include the Chen correlation for both gravity-dominated and shear-dominated flows, Eq. (4) in Section 4.3.1.2, as soon as it became clear that there had been no appropriate correlation for a pressurizer insurge transient. For the future APROS releases further assessment of the correlations by separate effect test cases is suggested to investigate whether the two correlations are capable of satisfactorily covering different thermal-hydraulic phenomena where wall condensation is important.

Another problematic feature of APROS encountered during the simulations is that the pressurizer component limits the node number to 30. The 30-row table is a limitation in heat transfer modules too as was seen in Section 4.2 where the 100-node pressurizer was built using the “Pipe with Heat Structure” component. The pipe wall representation which consisted of 5 radial and 102 axial heat nodes allowed only 30 of the 102 heat nodes to be connected to the heat transfer module without special operations at the calculation level, even though the pipe component itself can be composed of an arbitrary number of nodes. The original idea when the components were developed has apparently been that no more than 30 nodes should be required for any component model. However, modern computers can handle large simulation models in reasonable calculation times. Especially when modeling separate effect tests in which the main focus is on a specific phenomenon which is investigated in detail dense nodalizations are necessary. In addition, encountering this kind of limitations in the code can be very confusing to an analyst who is not thoroughly familiar with the basic calculation level of APROS, especially when they are not properly documented in the APROS manuals.

From the user’s point of view there are several differences between using APROS and TRACE. The SNAP interface for TRACE is quite clear and comfortable to work with in comparison to GRADES. For example, for a heat structure component the values for initial node temperatures are clearly accessible in the property window of the component and the input decks of the components are easily viewed in SNAP. In GRADES the information accessed via the component property window has a lot of variation depending on the component and sometimes the necessary input to make the model function as supposed must be inserted directly into the calculation level parameter. An advantage of SNAP is that it includes the possibility to generate animation models of which examples were seen in Sections 6.1 and 6.2. The animation model reads the graphics output file which was created during calculation. At the moment in APROS there is no such postprocessing tool. On the other hand, using GRADES the simulation parameters can be monitored and trend curves drawn in real time during the simulation, and it is easy to notice if something goes wrong in the calculation. Further development of the APROS user interface and post-processing and visualization tools could help in gaining international recognition for the code.

7 CONCLUSIONS

A significant improvement to the APROS pressurizer component was achieved by discovering the inapplicability of the wall condensation correlations for laminar vertical flows, and modifying the condensation model. After the modification relatively good simulation results were obtained for the PACTEL insurge-outsurge and spray tests. Also the Loviisa turbine transient indicated that it is essential to use the appropriate wall condensation correlation even though the significance of the interfacial condensation is emphasized in a realistic-scale system.

The deviation in the results of the PACTEL ATWS simulation runs compared to test data and other problems encountered during the calculations could be mostly explained by examination of the APROS code itself and the test documentation. Generally, the results of the MIT tests obtained by both codes do not correspond the measured data as well as the PACTEL results, especially the performance of APROS is not as good as in the PACTEL transients. In the MIT insurge transients APROS pressure calculation starts to oscillate as a result of the suddenly enhanced condensation when water level increases across a node boundary. This effect is not as drastic in the PACTEL cases where the system pressure is remarkably higher and the temperature differences between saturated state and injected water radically smaller. The poor APROS results might be explained by an increasing numerical error which is caused by the relatively low pressure conditions in the system and the uncontrolled sloshing of water due to the absence of flow resistance in the calculation level branches of the pressurizer component. A further investigation, i.e. studying the connection of the frictionless branches in the pressurizer component to the unstable calculation, in order to find out and remove the cause for these APROS results would be necessary.

The phenomena occurring in the MIT calculations are not as reliably explained as the PACTEL test behavior since a better documentation of the PACTEL experiments is provided. This is also true for the Neptunus case. Especially in the Neptunus test the information available on the instrumentation of the test facility was very limited, whereas the measurement system of the PACTEL and MIT pressurizer were described in detail. Also, the MIT pressurizer with its extensive thermocouple installations and the PACTEL pressurizer contained a better temperature measurement system than the oldest Neptunus facility. A comprehensive documentation helps to define the simulation boundary and initial conditions accurately. In this study, the best results were obtained for the test case of which most information was available. This highlights the importance of experimental research and comprehensive documentation of the tests to be able to make more reliable analysis of the results.

In most cases TRACE simulations showed similar behavior as the APROS simulations but during insurge transients and piston effect TRACE appears to exaggerate the pressure increase. In particular the Neptunus simulation peak pressures were relatively very high. This may be caused by an ineffective spray cooling or an inaccurate heat transfer correlation for wall condensation. It must be kept in mind that the experimental heat transfer correlations always have some error margin and they are assessed for a certain parameter range. In case of spray injection, as well as numerous other separate effect phenomena, the thermal hydraulic codes developed for large systems are not capable of modeling the phenomenon mechanistically. The heat and mass transfer between spray droplets, steam and pool surface are computed from the overall energy balance. Incorporating detailed models for different aspects of the phenomenon could greatly improve the modeling capabilities.

The testing of different nodalization schemes using APROS showed that the 30-node pressurizer gives reasonably accurate results and only a slight improvement can be obtained by a 100-node model considering that the calculation of a 100-node model requires much more computational effort than a 30-node model. The 10-node model and 3-node model results were not good and especially the use of only three nodes is not recommended, also as a part of larger system models. The nodalization scheme study shows that modeling errors due to inaccurate nodalization and use of inappropriate heat transfer models can cancel each other out and apparently good results may actually be unphysical. Thus, care is needed to identify this kind of problem situations and their source. Investigation of the improved thermal stratification model of APROS revealed an improved axial temperature distribution on the topmost part of the liquid but practically there was no significant effect on the pressure response in the simulated cases. In all the cases a single channel nodalization was used. A drawback of this type of a model is that it is not capable of simulating the convection in the water volume and mixing of hot and cool water. Especially in case of slow transients and large systems with multiple heater groups in which the heaters play a significant role in the overall heat transfer processes, such as the Loviisa pressurizer, a two-channel model could provide a more realistic simulation.

REFERENCES

Aksan, N., D’Auria, F., Glaeser, H., Pochard, R., Richards, C., Sjoberg, A. 1993. OECD/NEA-CSNI Separate Effects Test Matrix for Thermal-hydraulic Code Validation. Volume 1. Phenomena Characterisation and Selection of Facilities and Tests. Organisation for Economic Co-operation and Development. OCDE/GD (94)/82. Paris. 678 p.

APROS Nuclear with Containment Model Documentation. Distributed with APROS 5.05 installation.

Bestion, D. 1990. The physical closure laws in the CATHARE code. Nuclear Engineering and Design. Vol. 124. pp. 229-245.

Chen, S.L., Gerner, F.M., Tien, C.L. 1987. General Film Condensation Correlations. Experimental Heat Transfer. Vol. 1, pp. 93-107.

Hänninen, M., Ylijoki, J. 2004. The Constitutive Equations of the APROS Six-equation Model. Espoo, VTT.

Kim, S. 1984. An Experimental and Analytical Model of a PWR Pressurizer During Transients. Doctor of Philosophy Thesis. Massachusetts Institute of Technology. Department of Nuclear Engineering. 226 p.

Kim, S., Griffith, P. 1987. PWR Pressurizer Modeling. Nuclear Engineering and Design. Vol. 102, No 2, pp. 199-209.

Lamarsh, J.R., Baratta, A.J. 2001. Introduction to Nuclear Engineering. Third Edition. Upper Saddle River, New Jersey, USA, Prentice Hall. 783 p. ISBN 0-201-82498-1.

Lazor, M.D. 2004. Evaluation of Assessment Techniques for Verification and Validation of the TRACE Nuclear System Code. Master of Science Thesis. The Pennsylvania State University, The Graduate School, College of Engineering. 136 p.

Peterson, A.C. 1984. TRAC-PF1/MOD1 Independent Assessment: NEPTUNUS Pressurizer Test Y05. Albuquerque, New Mexico, USA, Sandia National Laboratories, NUREG/CR–3919. 49 p.

Prelewicz, D., Mortensen, G.A., Barber, D., Bolander, M., Fletcher, D., Caraher, D., Wang, W. 2005. RELAP5 Status Report. Spring 2005 CAMP Meeting. Dubrovnik, Croatia, May 2-4, 2005.

Riikonen, V. 1998. ATWS Experiments with PACTEL: Pressurizer Experiments. Espoo, VTT Energy, TEKOJA 1/98. 11 p.

Shah, M.M., 1979. A General Correlation for Heat Transfer During Film Condensation inside Pipes. Int. J. Heat and Mass Transfer. Vol. 22, pp. 547-556.

Spore, J.W., Elson, J.S., Jolly-Woodruff, S.J., Knight T.D., Lin, J.-C., Nelson, R.A., Pasamehmetoglu, K.O., Steinke, R.G., Unal, C., Mahaffy, J.H., Murray, C. 2000. TRAC-M/FORTRAN 90 (Version 3.0) Theory Manual. Los Alamos National Laboratory, Los Alamos. LA-UR-00-910. 923 p.

Tuunanen, J., Kouhia, J., Purhonen, H., Riikonen, V., Puustinen, M., Semken, R.S., Partanen, H., Saure, I., Pylkkö, H. 1998. General description of the PACTEL test facility. Espoo, VTT, VTT-Tiedotteita – Research Notes 1929. 35 p.

USNRC. NRC Reactor Safety Code User Information Exchange. Referred October 7, 2005. < http://www.nrccodes.com/ >

Validyne Engineering. DP15 Pressure Measurement System. Referred November 14, 2005. <http://www.validyne.com/data_pdf/dp15.pdf>

Vihavainen, J., Hänninen, M., Tuunanen, J. 1999. Improved Thermal Stratification Modeling in the Apros Code Simulations of Passive Safety Injection Experiments. Ninth International Topical Meeting in Nuclear Reactor Thermal Hydraulics (NURETH-9). San Francisco, California, USA, October 3-8, 1999.

Weaver, W. 2004. Improvements to the Pressurizer Component. 2004 International Relap Users Group Meeting. Sun Valley, Idaho, USA, August 25-27, 2004.

Yrjölä, V. Assessment of RELAP5/MOD2 Cycle 36.04, Against the Loviisa-2 Stuck-Open Turbine By-Pass Valve Transient on September 1, 1981. 1992. Washington, D.C., USA, Office of Nuclear Regulatory Research, USNRC, NUREG/IA-0047. 81 p.

APPENDIX 1. PACTEL ATWS -10 – 13 STEAM SUPERHEAT

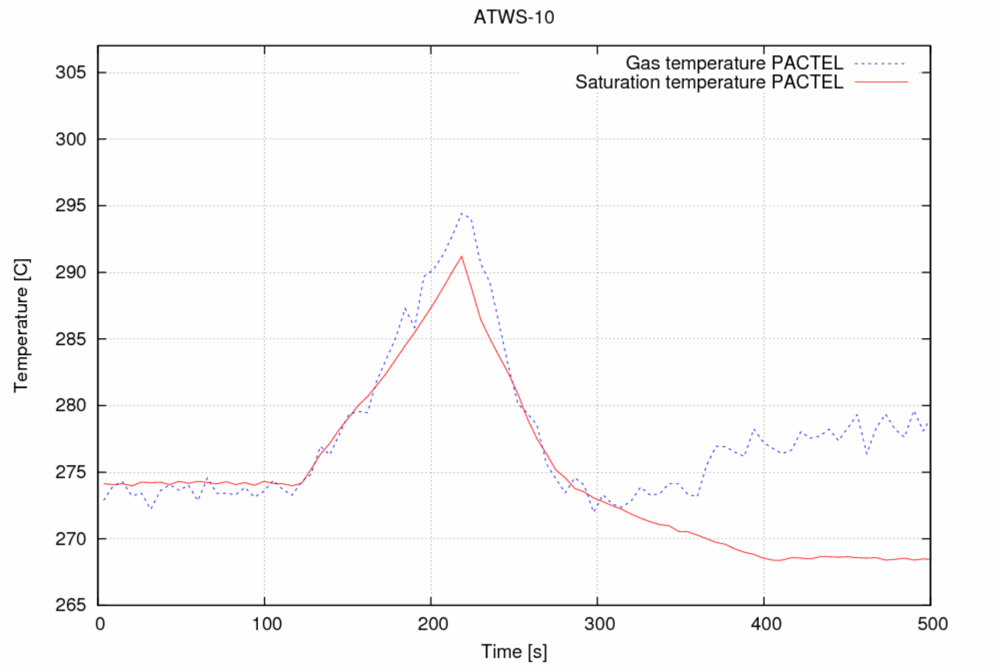

Figure A1. Measured steam and saturation temperatures during ATWS-10 transient.

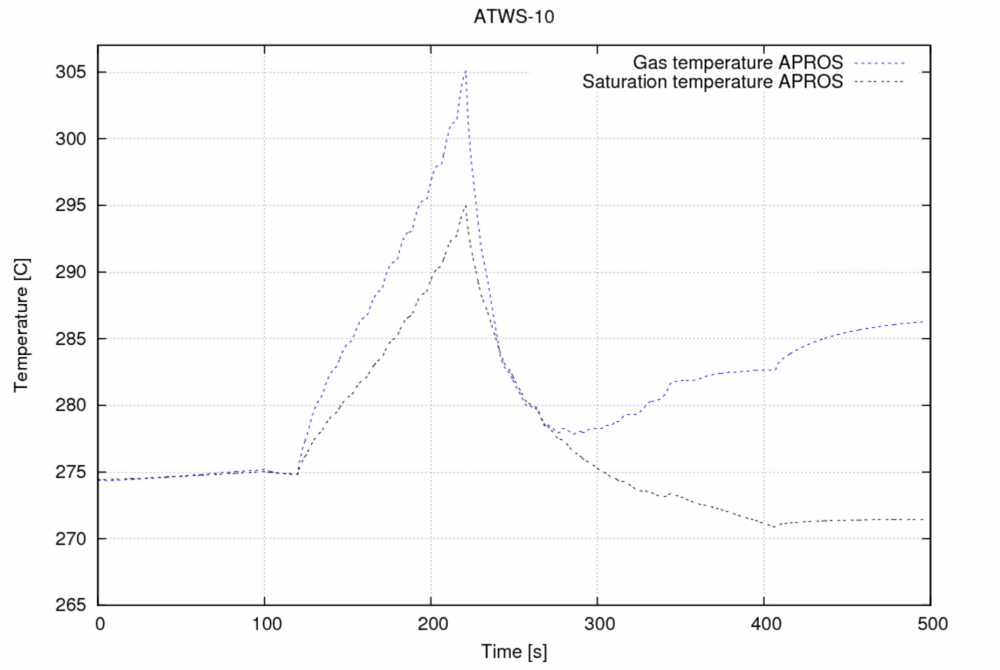

Figure A2. Calculated steam and saturation temperatures during ATWS-10 transient.

APPENDIX 1 CONTINUED

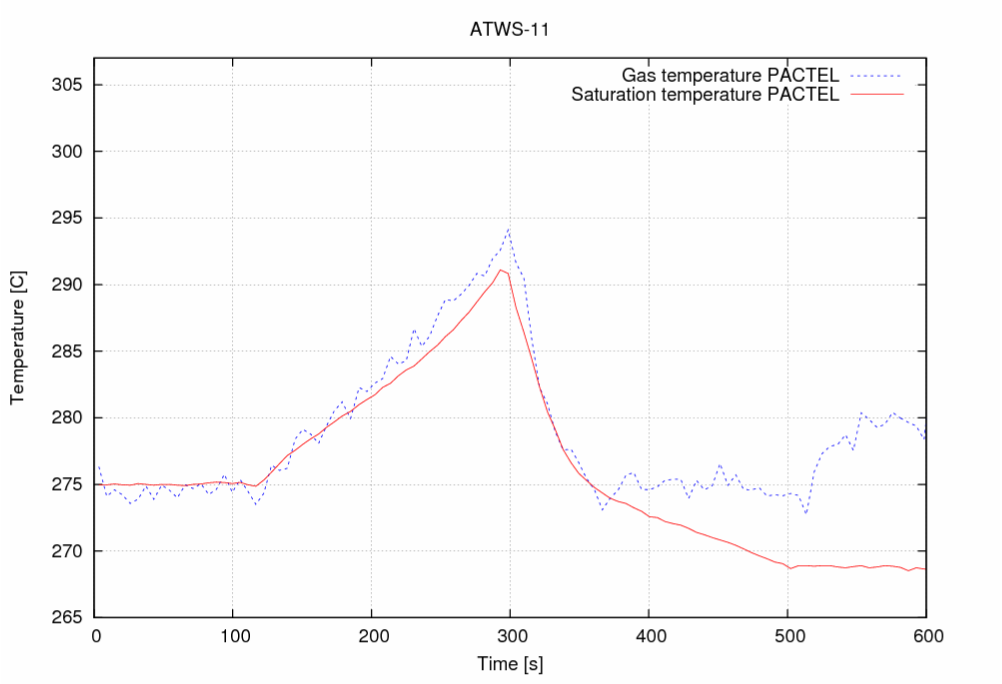

Figure A3. Measured steam and saturation temperatures during ATWS-11 transient.

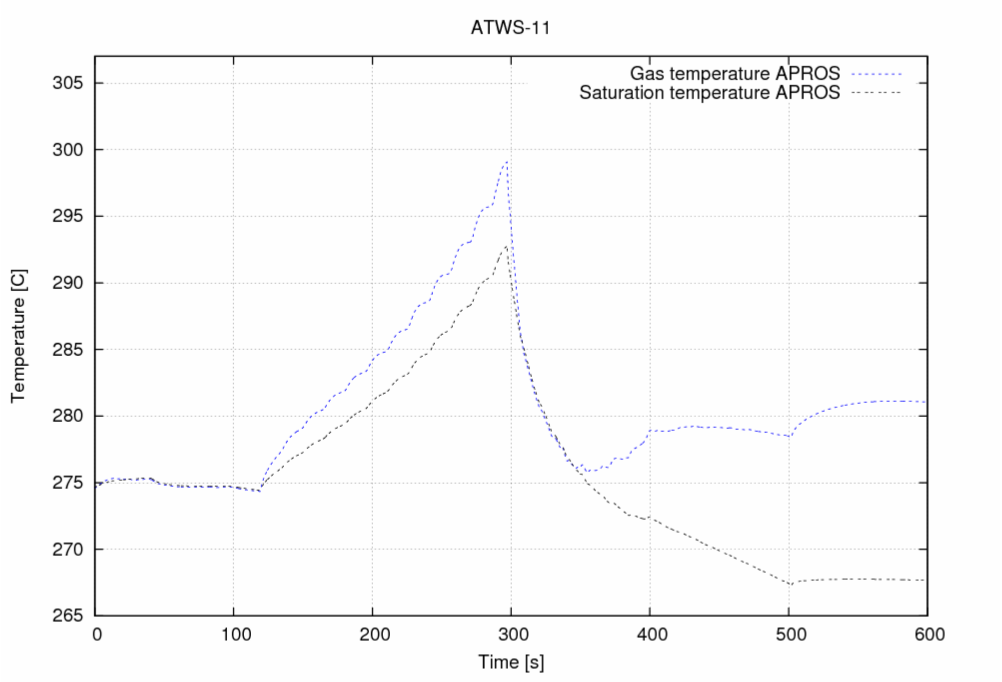

Figure A4. Calculated steam and saturation temperatures during ATWS-11 transient.

APPENDIX 1 CONTINUED

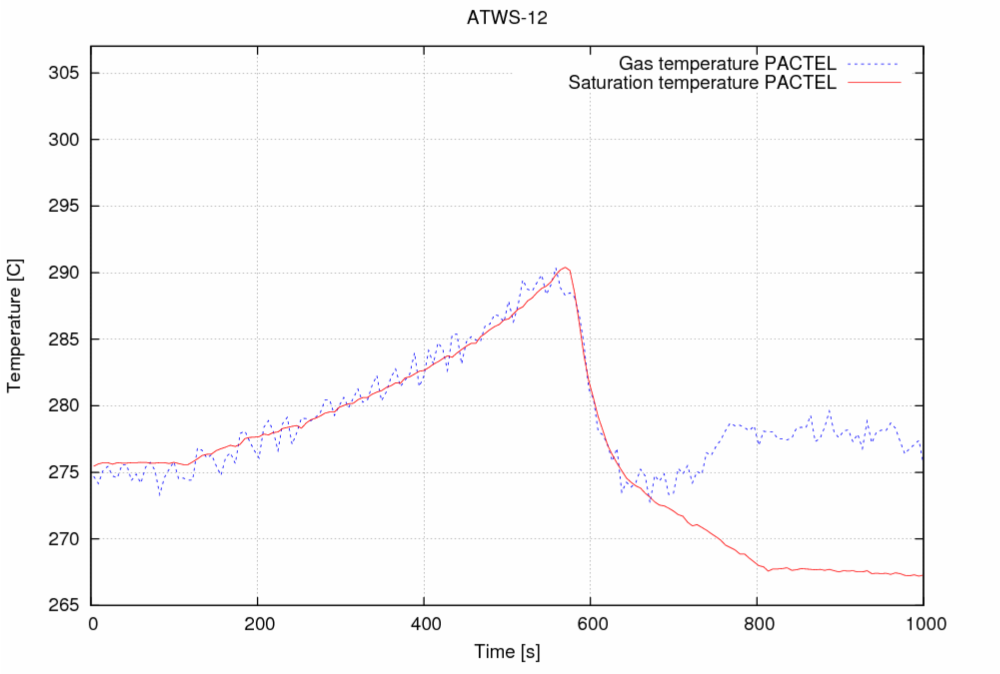

Figure A5. Measured steam and saturation temperatures during ATWS-12 transient.

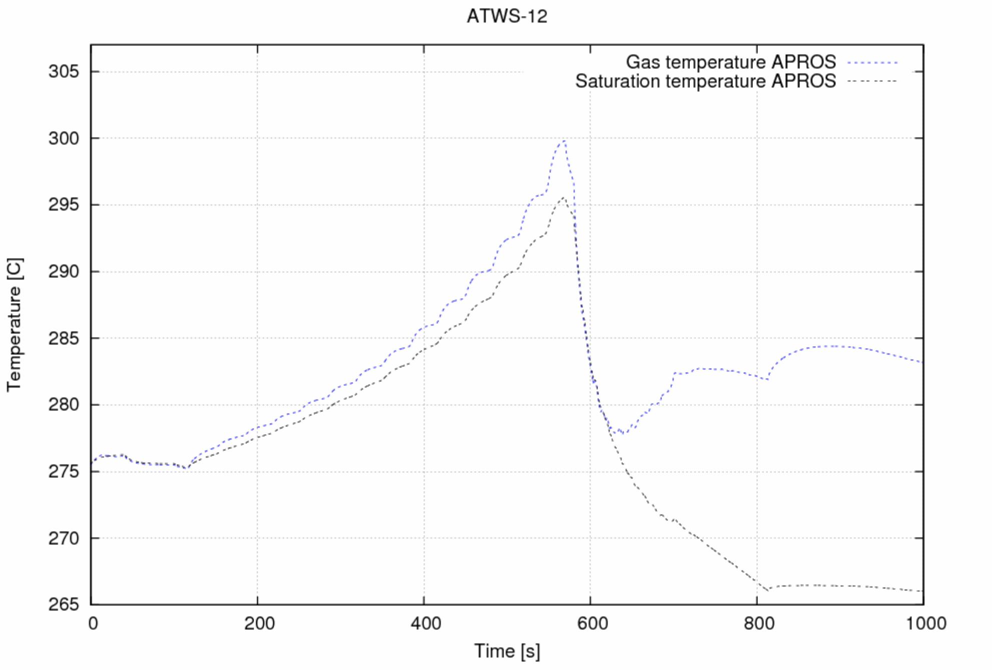

Figure A6. Calculated steam and saturation temperatures during ATWS-12 transient.

APPENDIX 1 CONTINUED

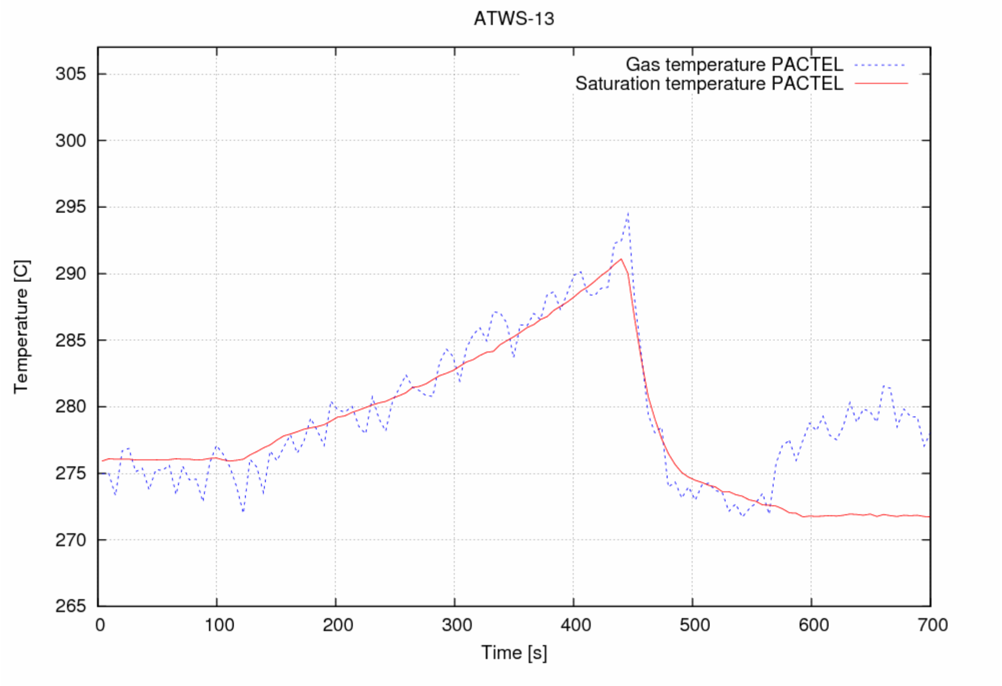

Figure A7. Measured steam and saturation temperatures during ATWS-13 transient.

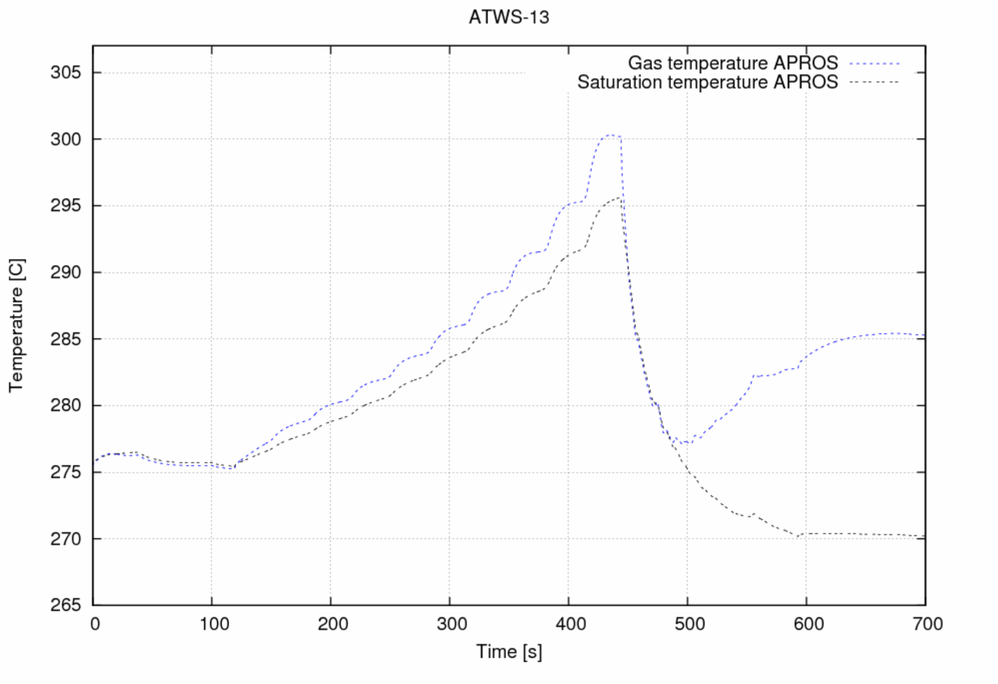

Figure A8. Calculated steam and saturation temperatures during ATWS-13 transient.